WARSAW UNIVERSITY

OF TECHNOLOGY

Faculty of Mechatronics

Ph.D. THESIS

Dariusz Jarząbek, M.Sc. Eng.

A method for investigation of fracture on the nanometer scale by use of SFM and its applications

Supervisors

Professor Zygmunt Rymuza, Ph.D., D.Sc.
Warsaw University of Technology

Professor Thomas Jung, Ph.D., D.Sc.
University of Basel

Warsaw 2013

Abstract

The knowledge of materials properties and materials behavior is essential for the design of machines and any type of device. Consequently, numerous measurement methods assessing different properties have been established. Much research in recent years has focused on materials studied on the nanometer scale due to the fact that different behavior arises depending on the scale. This phenomenon occurs on one hand, because the probability to encounter defects in smaller objects gradually decreases as a consequence of defect density, on the other hand surface and interface energies influence the mechanical properties with decreasing external dimensions. This provides the motivation to perform mechanical experiments on objects as small as possible. In addition, the design of micro and nanodevices (MEMS, NEMS) and the development of novel technologies (e.g. with the use of silicon-on-insulator (SOI) wafers, nanoimprint lithography), require exact knowledge on how material behaves on the nanometer scale. Most importantly the maximal stresses and strains before failure need to be known for every material in any application.

This thesis first reviews the capability of Scanning Force Microscopy (SFM) to perform experiments with forces in a wide range, from low non-contact forces to high contact forces inducing mechanical deformations in the substrate. In analogy to fracture mechanics, as established in materials science, SFM is used to exert forces to pillars with nanometer dimensions while the cantilever deformations are monitored quantitatively. Using this novel approach, in combination with a number of different ways to produce nanopillar samples, a large number of experiments can be performed and shall be presented, as they derive from different experimental modes including also lateral (friction) force mode of operation of a Scanning Force Microscope.

Furthermore quantitative measurements of the fracture strength or flexural strength of different materials, and materials interfaces in different environments (atmosphere, water, various solutions) is presented. To analyze the various data obtained, Finite Element Method (FEM) calculations were used. The simulation allows to predict the threshold stresses and strains of nanopillars in comparison. To assess failure in dependence of slow degradation processes induced by exposure to different fluids measurements are repeated in a suitable sequence. The above described method provides a unique platform for addressing a wide range of scientific problems and applications of the results.

Streszczenie

Wiedza na temat własności materiałów oraz ich zachowania w różnych warunkach jest niezbędna przy projektowaniu wszelkiego rodzaju urządzeń. W związku z tym, opracowano wiele metod pomiarowych dla rożnych typów materiałów i różnych warunków ich pracy. W ostatnich latach duże znaczenie odgrywają metody pomiarowe w skali nanometrowej. Jest to spowodowane występowaniem tzw. efektu skali – zmiany własności materiałów (np. twardości) wraz ze zmniejszaniem się wymiarów próbki.

Praca ta wpisuje się w nurt badań związanych z nanotechnologią, a zwłaszcza z nanometrologią. Opisano tu metodę pomiaru naprężeń krytycznych oraz modułu Younga w strukturach o wymiarach wyrażonych w nanometrach przy pomocy mikroskopu sił atomowych (AFM, SFM). Urządzenie to jest w stanie wywierać siły w szerokim zakresie – standardowo od pojedynczych nanoniutonów do kilkudziesięciu mikroniutonów – na wykonane przy pomocy litografii elektronowej (oraz innych technologii wytwarzania w skali nano) tzw. nanowieże (pionowe walce o stosunku średnicy do wysokości równym od 1 do 4). Struktury te są gięte oraz skręcane, a wreszcie łamane, przy czym mierzona jest jednocześnie siła powodująca te deformacje. Następnie przy pomocy podejścia analitycznego oraz numerycznego metodą elementów skończonych (MES) wyznaczane są naprężenia krytyczne w badanych strukturach oraz moduły Younga materiałów, z których struktury zostały wykonane..

Opracowana w tej pracy metoda została następnie wykorzystana do pomiaru materiału kruchego – krzem, materiału lepkosprężystego – PMMA w funkcji temperatury, oraz interfejsu pomiędzy dwoma różnymi materiałami – interfejs krzemu i tlenku krzemu – w różnych środowiskach – powietrzu, wodzie, roztworach. Głównym celem tych eksperymentów było ukazanie wszechstronności opracowanej metody. Niemniej jednak badania dostarczyły interesujących informacji na temat mechanicznych własności materiałów w skali nanometrowej. Wyniki tych pomiarów również zostały w tej pracy szeroko przedyskutowane.

CONTENTS

1.   Introduction

1.1.   Nanotechnology

According to the National Nanotechnology Initiative (a Unites States federal nanoscale science, engineering, and technology research and development program) nanotechnology is the manipulation of matter with at least one dimension sized from 1 to 100 nanometers (1 nm = 10^{-9}m). Therefore it is very broad, including fields of science as diverse as surface science, organic chemistry, microfabrication, molecular biology etc. Nanotechnology may be able to create many new materials and devices with a vast range of applications, such as in medicine, biomaterials, energy production or electronics. Hence, in recent years it has become one of the most dynamic developing field of science and engineering.

The concepts that seeded nanotechnology were first discussed in 1959 by one of the greatest physicist of the twentieth century – Richard Feynman, in his talk 'There's Plenty of Room at the Bottom', in which he described the possibility of synthesis of structures via direct manipulation of atoms and molecules. Scientists and engineers, inspired by Feynman's concepts, started developing the methods of visualisation and manipulation of matter in nanoscale. The invention of the scanning tunnelling microscope in 1981 provided unprecedented visualization of individual atoms and bonds, and was successfully used to manipulate individual atoms in 1989. In 1986 the atomic force microscope, which is the main tool used in this thesis, was invented.
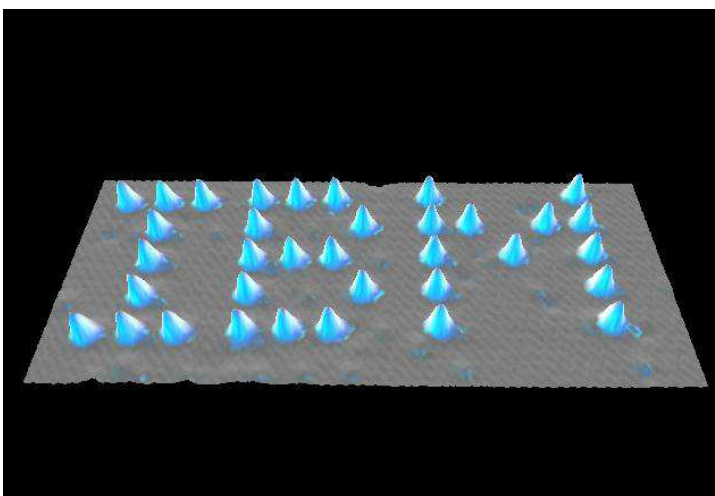
Figure 1.1 *Researchers at the IBM Almaden Research Center were able to write the name of their company by manipulating single atoms with the scanning tunneling microscope. (source:[1])*

Nowadays, it is difficult to imagine a world without nanotechnology. Modern electronic devices are widely spread all over the world. Smartphones and fast computers among other digital electronic devices allow for an unprecedented level of communication and data exchange. This has changed many aspects of business and social life on the planet and lead to the so called 'global village'.

This thesis presents a small step forward towards the further miniaturization of devices by developing the abilities of Scanning Force Microscopy to manipulate extremely small, nanometer-size objects and to investigate the mechanical properties of nanostructures. Thereby, it contributes to the ongoing progress of nanotechnology.

1.2.   Size effect and measurements on the nanoscale

The knowledge of material behavior and its properties is essential in machine design and numerous methods exist for assessing materials properties on the macroscale [2-6]. On the nanoscale, however, interesting phenomena occur, which are often referred to as size effects. Size effects relate to the scaling problem, which are central to every physical theory and which depends on the property of concern. The size effect in solid mechanics is understood as the effect of the characteristic structures size on the nominal strength of structure when geometrically similar structures are compared [7]. One of the most popular examples for the mechanical size effect is the increase of surface hardness, with decreasing indentation depth [8] (**Fig.1.2**).
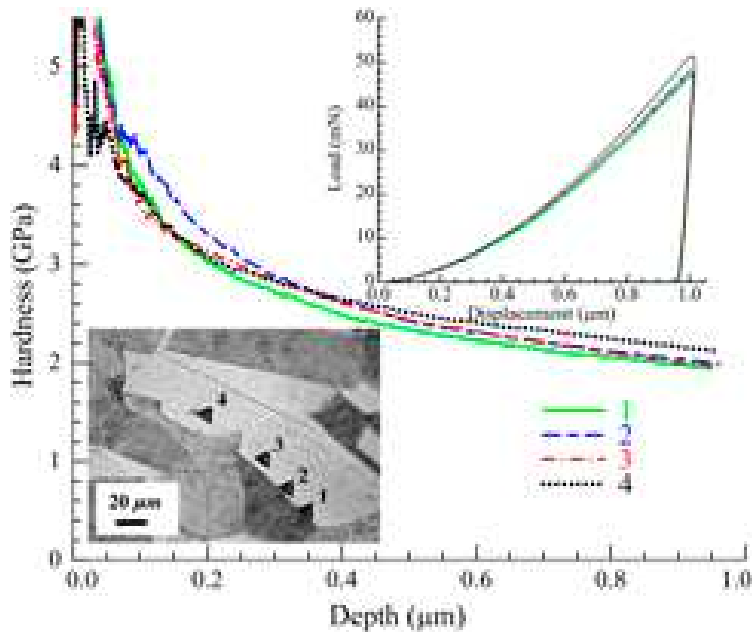
Figure 1.2 *An example for the size effect. The surface hardness increases while the indentation depth is reduced. (image source: [7])*

Size effects modify properties on smaller scales and therefore affect the engineering of smaller devices. Therefore there is a need for measurements of mechanical properties on the nanoscale contributing to their deeper understanding. In many cases, it was observed that mechanical properties on the nanoscale significantly deviate from bulk values. This may e.g. occur from the finite defect densities in the material which will affect small structures depending on their discrete number and their position within the geometry, far away from the homogenously distributed case. This provides a strong motivation to perform mechanical experiments on objects with external dimensions down into the nanometer range. In past years several techniques for the measurement of properties of thin layers and nanostructures have been developed [9-11] but usually only the most basic mechanical properties (Young modulus, hardness) have been measured.

For designing nanomachines as well as current day electronic and electromechanic devices, which already include nanostructures, it is important to know exactly how material behaves on the nanoscale, what are the highest stresses and strains which can be sustained before fracture. Moreover, modern technological processes, such as polymer injection molding and nanoimprint lithography, require well-established knowledge about the used materials, especially about the fracture strength (e.g. of molds and molded parts) or yield strength of the used polymers. Hence, this provides the main reason why this thesis takes focuses on the investigation of fracture strength and the mechanisms of material failure on the nanoscale.

1.3. Synopsis

After this short introduction to the world of nanoscience, nanometrology and nanotechnology, Chapter 2 will present a short overview of the current state of fracture mechanics. This starts from the basic atomic model of fracture and material failure, then discusses the classical fracture and failure hypotheses, and finally describes more modern theories of fracture and adhesion with a focus on those which are needed to discuss the experimental results presented in this thesis. At the end of Chapter 2 there is also a critical review of currently available methods of fracture and adhesion measurement techniques, on the macroscale and on the nanoscale.

Chapter 3 shortly summarizes the goals and objects of this thesis, whereas Chapter 4 describes in detail the measurement technique, which has been developed in this thesis. At the beginning of Chapter 4 there is a general description of scanning force microscopy and of the force calibration methods which are important for quantitative measurements. Subsequently, the sample preparation is described. The technique of bending and fracturing nanopillars made of brittle materials with the SFM is introduced in the third paragraph of the Chapter 4 and ductile materials are taken into consideration in paragraph 4.4. At the end of Chapter 4, imperfections and limitations of the developed methods are discussed and suggestions are made towards methodological improvements.

Chapter 5 provides a set of applications for the investigation of fracture strength and failure investigation, i.e. for nano-fracture mechanics with the SFM. In particular investigations of different materials (brittle or ductile) and in different environments are demonstrated. Firstly, the fracture strength of the silicon/silicon dioxide interface is measured. This particular interface is often used in modern electronics and micro-electro-mechanical systems (MEMS) technology, hence the detailed knowledge of its properties is of high importance. Subsequently, the influence of different chemical environments (air, water, salt solutions) on this interface is studied. Finally, the mechanical properties of PMMA nanopillars is investigated which provides an important basis towards improvements of the nanoimprint lithography process.

The findings of this thesis are summarized in Chapter 6 and conclusions are presented together with an outlook and suggestions for further research are made.

2. Fracture mechanics – an overview

2.1. The atomic bonding model for estimation of theoretical mechanical properties

Material scientists and engineers have long sought for methods to determine the mechanical properties of materials from the knowledge of the bonding properties of individual atoms. The observation of mechanical elasticity suggests the existence of both attractive and repulsive forces between atoms. These attractive and repulsive forces vary depending upon the interatomic or intermolecular separation. Attractive forces are mainly electrostatic in nature while repulsive forces are much more complicated to understand, as they are caused by the interactions between the electron shells of the atoms and are difficult to estimate directly. The variation of attractive and repulsive forces and of the binding energies in dependence of the separation distance are shown in **Fig.2.1**, where r_0 is the equilibrium spacing. The forms of the equations agree well with physical observations but the values of the constants α, β, m and n vary for different materials and atoms. Obviously, crystal defects, such as dislocations, vacancies etc. complicate the picture in metals, and the long chains, entanglements and other defects complicate the picture in polymers while ionic compounds can often be treated in an electrostatic model. Note however, that the polycrystalline grain structure of materials often can also introduce a strong modification of this picture derived for the homogenous material.
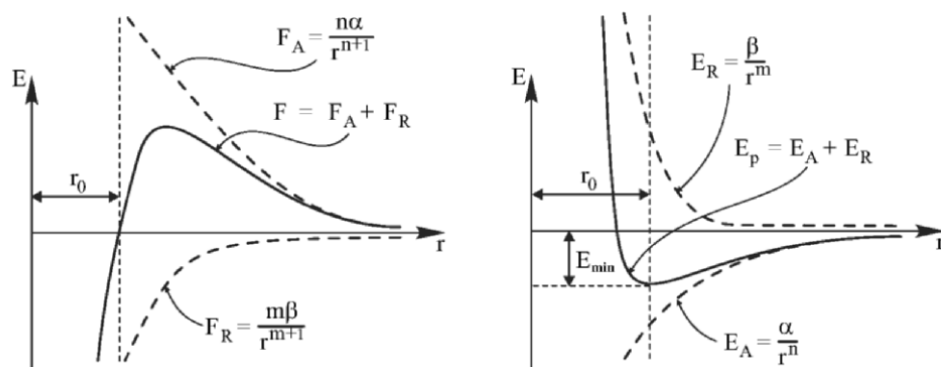
Figure 2.1 The variation of attractive and repulsive forces and energies with separation distance. (Image source: [12]) E stands for energy and r for distance. r_0 is the equilibrium spacing, F_A and F_R are attractive and repulsive forces, respectively, and their sum F is the resultant force. α, β, m and n are constants, which vary for different materials and atoms. E_A, E_R and E_p stand for attractive, repulsive and overall potential energy, respectively.

If the tensile forces are large enough, the distance between atoms can be so large that the attractive forces will tend to zero and the bond will be broken. On the other hand, the application of compressive forces cannot force neighbouring atoms to merge due to the Pauli exclusion principle and therefore the material will fracture from the inhomogeneous distribution of stresses and strains. On the grounds of the atomic structure of a material it should however be possible to determine the theoretical strength of the material. Unfortunately, the complicated equations of quantum mechanics and the great number of atoms, which must be taken into consideration in the simulation, make render precise calculations difficult and close to impossible for large slabs of materials with a realistic distribution of defects and grains / grain boundaries. Therefore to date, the empirical determination remains a more versatile evaluation of the mechanical properties of materials, while important insight and input can be derived from ab-inito calculations of model systems.

2.2. Classical fracture and failure hypotheses

The word *classical* in the heading of this paragraph means that the so-called *strength hypotheses* are already quite old. Partially they were established at the end of the 19th or the beginning of the 20th century. They have been pushed into the background as far as research is regarded. However, because of their simplicity and versatile application they are still extremely important, especially in machine design.

2.2.1. Basic concepts

There are two different fracture mechanisms: ductile fracture and brittle fracture (**Fig. 2.2**). Ductile behaviour is characterized through plastic deformations which occur when the stress exceeds the yield strength σ_Y. In this case, the ultimate stress at fracture will be attained only after sufficiently large inelastic deformations. This is the behaviour for most metals and polymers. On the other hand, brittle material behaviour is characterized by the fact that no significant inelastic deformations occur before fracture. This type of fracture is common for glass, ceramics, stones, concrete, ice etc. but is occasionally also found in alloys and metals (especially at low temperatures).
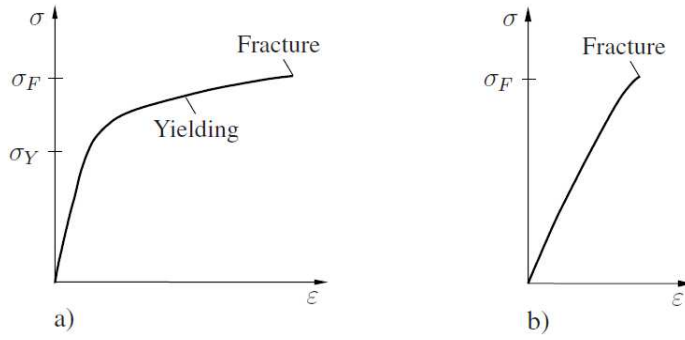
Figure 2.2 Two different types of behaviour of materials: ductile (a) and brittle (b). σ_F denotes a fracture strength of the material while σ_Y is a yield strength of ductile material.

σ stands for stress and ε for strain.

The strength of the material is often characterized by either the yield stress or by the ultimate stress at the fracture threshold. The associated material parameters are the yield strength and the fracture strength. However, it should be emphasized that both ductile and brittle behaviour are not pure material properties. The stress state plays also an essential role during fracture process. Therefore, it could be assumed that for any complex loading of a material, its failure limit can be characterized by the current stress or strain state. Hence, the failure condition can be expressed as:

$$F(\sigma_{ij}) = 0 \quad \text{or} \quad G(\varepsilon_{ij}) = 0 \tag{Eq. 2.1}$$

where σ_{ij} is the stress tensor and ε_{ij} is the strain tensor.

A failure condition of the type (**Eq. 2.1**) implies that the material state at failure does not depend on the deformation history. This can be applied with sufficient accuracy mainly to brittle materials or to plastic yielding in ductile materials. Moreover, such a failure condition requires the material to be considered as a continuum without any macroscopic defects or grain / domain structure.

2.2.2. Cracks

From a macroscopic, continuum mechanics point of view, a crack is considered as a cut in a body. Its opposite boundaries are called crack surfaces. The crack ends at the crack tip. Concerning the formation of the crack, there are three different crack opening modes (**Fig. 2.3**). Mode I denotes a symmetric crack opening with respect to the xz-plane. Mode II is characterized by an antisymmetric separation of the crack surfaces due to the relative displacement in x-direction (normal to the crack front). Mode III described the separation caused by relative displacements in z-direction

15

(tangential to the crack front). The symmetries associated with the different types of crack opening are only locally defined but in special cases they may hold for the entire body.
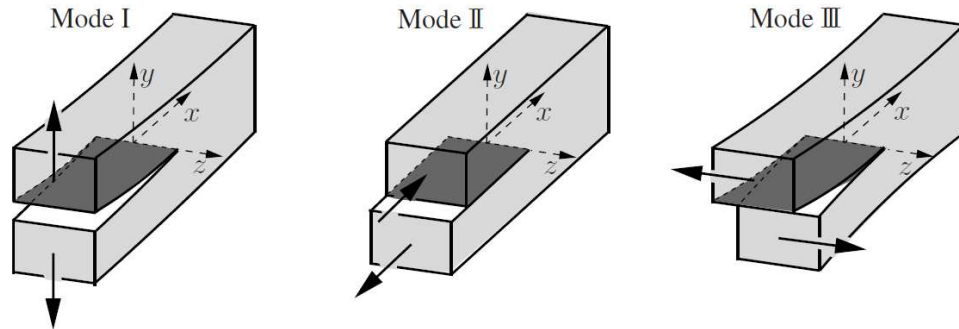
Figure 2.3 *Crack opening modes. (Image source: [13])*

2.2.3. Failure hypotheses and deformation behaviour during fracture

In literature there are many failure hypotheses of the type described by **Eq. 2.1** and it is possible to establish many more. Some of them may be found in [13]. In what follows, some common hypotheses are presented, particularly those, which are important for the analysis and discussions of results presented in this thesis.

Principal stress hypothesis

This hypothesis was established by W.J.M. Rankie (1820-1872), G. Lamé (1795-1870), and C.L. Navier (1785-1836). According to this hypothesis, failure is expected to take place when the maximum principal stress reaches σ_t or when the minimum principal stress reaches $-\sigma_p$. The principal stress hypothesis may be applied to brittle fracture of materials. It neglects the influence of the two other principal stresses onto failure; therefore, its applicability is limited to brittle materials.

'Von Misses stress' hypothesis

According to the 'von Misses stress' hypothesis, the fracture occurs when a reference stress σ_{vm} is higher than an ultimate stress at fracture measured for uniaxial tension. In case of spatial stress state, the reference stress σ_{vm} is obtained from expression:

16

$$\sigma_{vm} = \sqrt{\sigma_1^2 + \sigma_2^2 + \sigma_3^2 - \sigma_1\sigma_2 - \sigma_2\sigma_3 - \sigma_3\sigma_1 + 3\left(\tau_{12}^2 + \tau_{23}^2 + \tau_{31}^2\right)}$$ **(Eq. 2.2)**

where $\sigma_{1,2,3}$ and $\tau_{12,23,31}$ are compounds of a stress tensor.

This failure criterion is applicable to the case of ductile materials.

Strain energy hypothesis

This hypothesis was proposed by E. Beltrami (1835-1900). It is here assumed that failure occurs when the strain energy density U reaches material-specific critical value U_c. Usually this assumption implies that the material behaves linearly elastic until failure occurs. It has been shown that this hypothesis is described by means of the principal stresses by the following equation:

$$3\sigma_c^2 = (1+\nu)\left[(\sigma_1 - \sigma_2)^2 + (\sigma_2 - \sigma_3)^2 + (\sigma_3 - \sigma_1)^2\right] + (1 + -2\nu)(\sigma_1 + \sigma_2 + \sigma_3)^2$$ **(Eq.2.3)**

where ν stands for Poisson's ratio.

No direct conclusion can be drawn for the deformation behaviour or the kinematics during fracture on the basis of the failure criterion alone. Respective statements are only possible when specific and physically meaningful assumptions are introduced.

At the incident of fracture new surfaces, - so called fracture surfaces – are created. The associated kinematics is complex and cannot be discussed in simple terms. Only for the case of sufficiently high stress conclusions can be drawn which are guided by the experimental results. Two basic patterns for the formation of fracture surfaces can be distinguished (**Fig.2.4**). For a normal stress dominated fracture, the fracture plane coincides with the cross section normal to the maximum principal stress (necessary tension). Shear dominated stress takes place when the fracture surface is formed by the cross section in which a certain shear stress reaches a critical value. Both types occur also in mixed forms.
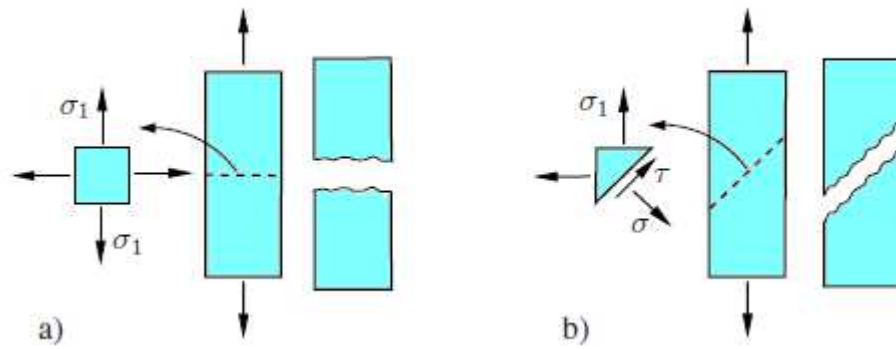
Figure 2.4 *Two basic patterns for the formation of fracture surfaces. In picture a) there is shown a normal stress dominated fracture, while in picture b) share dominated fracture is illustrated.(Image source: [13])*

2.2.4. Energy balance approach

The first analytical model for the mechanics of brittle fracture was developed in 1920 by Alan Arnold Griffith [14]. Rather than focusing on the crack-tip stresses directly, Griffith employed an energy-balance approach that has become the most useful development in materials science.

From continuum mechanics it is known that the strain energy U^* per unit volume V of stressed material is

$$U^* = \frac{1}{V}\int f dx = \int \frac{f}{A}\frac{dx}{L} = \int \sigma d\varepsilon \qquad \text{(Eq.2.4)}$$

where A is the surface of the formed crack, L stands for its length and f is a force.

For linear materials ($\sigma = E\varepsilon$):

$$U^* = \frac{E\varepsilon^2}{2} = \frac{\sigma^2}{2E} \qquad \text{(Eq.2.5)}$$

When the crack has grown into a solid to the depth a, a region of material adjacent to the free surfaces is unloaded, and its strain energy released. Griffith computed this energy, which for plain stress loading is:

18

$$U = -\frac{\sigma^2}{2E} \cdot \pi a^2$$

Here the dimension normal to the x-y plane is taken to be unity, so U is the strain energy released per unit thickness of specimen. Crack growth liberates this strain energy During the crack formation, bonds are broken, and the bond energy is then absorbed by the material. The surface energy S associated with a crack of length a (and unit depth) is:

$$S = 2\gamma a$$

(Eq. 2.7)

where γ is the surface energy and the factor 2 is needed because two free surfaces have been formed. As shown in **Fig. 2.5**, the total energy associated with the crack is then the sum of the (positive) energy absorbed to create the new surfaces, plus the (negative) strain energy liberated by allowing the regions near the crack flanks to become unloaded.
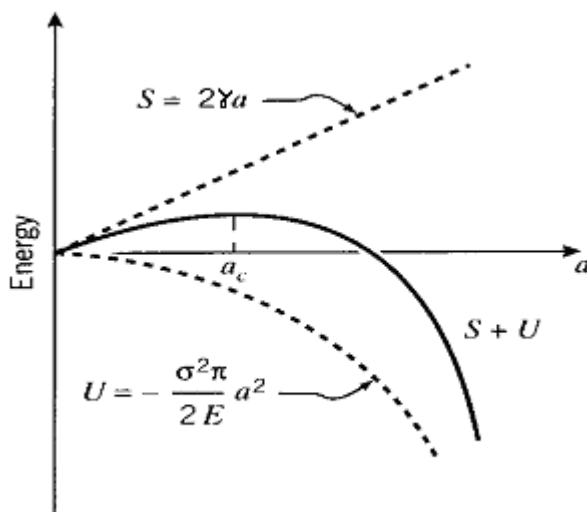
Figure 2.5 The total energy associated with the crack is the sum of the positive energy S absorbed to create the new surface plus the negative strain energy U liberated by allowing the regions near the crack surfaces to become unloaded. (Image source: [15])

As the crack grows longer, the quadratic dependence of strain energy on a eventually dominates the surface energy, and beyond a critical crack length a_c the system can lower its energy by letting the crack grow still longer. Up to the point where $a = a_c$, the crack will grow only if the stress increased. Beyond that point, crack growth is spontaneous and catastrophic.

The value of the critical crack length can be found by setting the derivative of the total energy $S+U$ to zero:

$$\frac{\partial(S+U)}{\partial a} = 2\gamma - \frac{\sigma_f^2}{E}\pi a = 0 \qquad \text{(Eq. 2.8)}$$

Because fast fracture is imminent when this condition is satisfied, we write the stress as σ_f. Finally, it can be calculated from:

$$\sigma_f = \sqrt{\frac{2E\gamma}{\pi a}} \qquad \text{(Eq. 2.9)}$$

Griffith's original work dealt with very brittle materials, specifically glass rods. Unfortunately, for ductile materials consideration of the surface energy alone fails to provide an accurate model for fracture. This problem was solved, at least in part, independently, by Irwin [16] and Orowan [17]. They suggested that in a ductile material the vast majority of the released strain energy was absorbed not by creating new surfaces, but by energy dissipation due to the plastic flow in the material near the crack tip. They proposed that the catastrophic fracture occurs when the strain energy is released at a rate sufficient to satisfy the needs of all these energy "sinks", and denoted this critical strain energy release rate by the parameter G_c; the Griffith equation can then be rewritten in the form:

$$\sigma_f = \sqrt{\frac{EG_c}{\pi a}} \qquad \text{(Eq. 2.10)}$$

This relation describes in very succinct way, the interrelation between three important aspects of the fracture process: the material, as evidenced in the critical strain energy release rate G_c; the stress level σ_f; and the size a, of the flaw.

2.2.5. Theory of acid-base interactions in adhesion

Fracture along materials interfaces is much more complicated process than fracture of solid bodies. There are many theories about fracture strength of different interfaces. Particularly interesting for this thesis is the acid-base theory of adhesion. In the absence of chemisorption and interdiffusion, the work of adhesion is the sum of the various intermolecular forces involved and can be related to the surface free energies (Dupré's equation):

20

$$W = \gamma_1 + \gamma_2 - \gamma_{12} \qquad \textbf{(Eq. 2.11)}$$

where γ_1 and γ_2 are the surface energies of components 1 and 2 and γ_{12} is the interfacial free energy. For two materials interacting via London dispersive forces only across their interface, Fowkes [18] suggested that W can be described by

$$W^d = 2(\gamma_1^d \gamma_2^d)^{\frac{1}{2}} \qquad \textbf{(Eq. 2.12)}$$

where W^d is the dispersive contribution to the work of adhesion and γ_i^d is the dispersive contribution to the surface energy γ_i of surfaces 1 and 2, respectively. The nondispersive contribution to the work of adhesion is more difficult to establish. Fowkes et al [19] attributed the nondispersive contribution of the work of adhesion W^p with Lewis acid-base interactions, which correspond to the acid-base contribution of the work of adhesion W^{AB} :

$$W^p = W^{AB} = W - W^d = W - 2(\gamma_1^d \gamma_2^d)^{\frac{1}{2}} \qquad \textbf{(Eq. 2.13)}$$

Two methods were developed to determine W^{AB}. The first was suggested by Fowkes [19]. This method makes use of the heat of acid-base adduct formation ΔH^{AB}:

$$W^{AB} = -f n_{AB} \Delta H^{AB} \qquad \textbf{(Eq. 2.14)}$$

where f is a free energy to enthalpy conversion factor and n_{AB} the number of acid-base adducts per unit area.

The second approach was introduced by van Oss and co-workers [20]. They introduced the notion of acidic and basic components to the surface energy (γ^+ and γ^-, respectively) to characterize the acid-base properties of materials and evaluate W^{AB}:

$$W^{AB} = 2(\gamma_1^+ \gamma_2^-)^{\frac{1}{2}} + 2(\gamma_1^- \gamma_2^+)^{\frac{1}{2}} \qquad \textbf{(Eq. 2.15)}$$

γ^+ and γ^- for solid can be determined by contact angle measurements using three reference liquids of known γ^d_L, γ^+_L, γ^-_L.

2.3. Fracture experiments on the macroscale

2.3.1. Tensile test

The uniaxial tensile test [21] is the most important test for measuring the plastic properties of materials for materials specification and for analytical purposes. It provides well-defined measures of yielding, ultimate tensile strength, work hardening and ductility. It can be also used to measure the temperature dependence and strain rate sensitivity of these quantities. The results from the test are commonly used to select the material for a specific application, for performing a quality control, and to predict how a material will deform under other types of applied forces.

The test process involves placing the test specimen in the testing machine and applying tension to it until fracture occurs. During the application of tension, the elongation of the gauge section is recorded against the applied force. The data is renormalized such that it does not depend on the geometry of the test sample. The elongation measurement is used to calculate the strain ε from the following equation:

$$\varepsilon = \frac{\Delta L}{L_0} = \frac{L - L_0}{L_0}$$

(Eq. 2.16)

where ΔL is the change in gauge length, L_0 is the initial gauge length, and L is the final length. The force measurement is used to calculate the stress σ using the following equation:

$$\sigma = \frac{F_n}{A}$$

(Eq. 2.17)

where F is the force and A is the cross-section of the gauge section. From these data the stress-strain curve (**Fig. 2.2**) can be plotted.

A tensile specimen (**Fig. 2.6**) is a standardized sample cross-section. It has two shoulders and a gauge (section) in between. The shoulders are large so they can be readily gripped, whereas the gauge section has a smaller cross-section so that the deformation and failure can occur in this area.
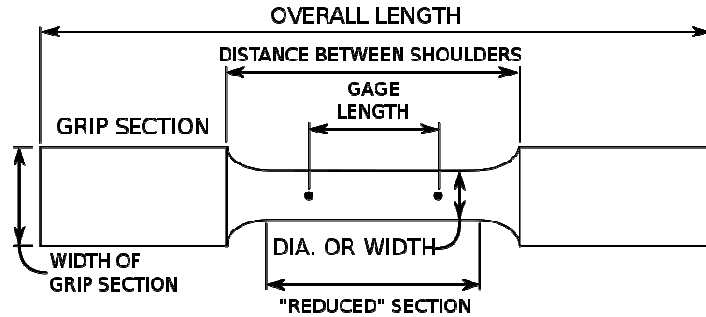
Figure 2.6 *A standardized tensile specimen cross-section. (Image source: [22])*

Figure 2.7 *An example of a machine used in tensile tests.*

2.3.2. Charpy impact test

The Charpy impact test, also known as the Charpy V-notch test, is a standardized high strain-rate test which determines the amount of energy absorbed by a material during fracture. The absorbed energy is a measure of a given material's notch toughness. The test is widely applied in industry because it is easy to prepare and conduct, so the results can be obtained quickly and cheaply.

The device (**Fig. 2.8**), which is used to conduct the experiment, consists of a pendulum of known mass and length which is dropped from the known height to impact the notched specimen of material. The energy which is transferred to the material can be

inferred by comparing the difference in the height of the hammer before and after the fracture (energy absorbed by the fracture event).

The notch in the sample must be of regular dimensions and geometry due to the fact that it affects strongly the results of the impact tests. The size of the sample can also affect results, since the dimensions determine if or not the material is in plane strain. This difference can greatly affect the conclusions made. The quantitative results of the measurement of the energy needed to fracture a material can be used to elaborate the toughness of the material and the yield strength.

The "Standard methods for Notched Bar Impact Testing of Metallic Materials" can be found in ASTM E23 [24] ISO 148-1[25] or EN 10045-1[26] where all the aspects of the test and equipment used are described in detail.
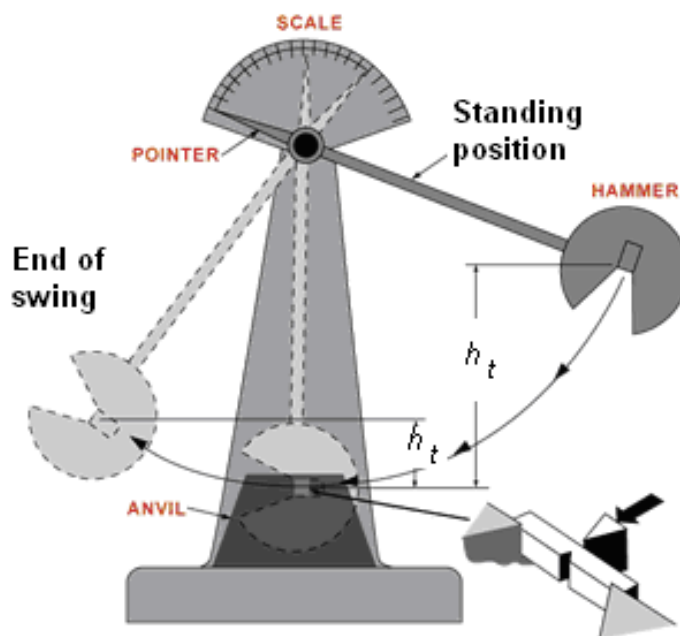
Figure 2.8 Charpy impact test device. h_t stands for the height of the hammer. (Image source: [23])

2.4. Fracture experiments on nanoscale

2.4.1. Nanoindentation fracture strength measurements for brittle materials

Nanoindentation is normally used for measuring thin film mechanical properties such as the elastic modulus and hardness [27]. The fracture toughness of brittle materials, as an important measure of the resistance of the materials to crack

propagation and fracture, can be also evaluated through the instrumented indentation. When a small indenter plastically penetrates a brittle solid, a pattern of cracks often forms around the impression, as the indenter is removed.

Generally, there are three types of cracks as they are illustrated in **Fig. 2.9**.
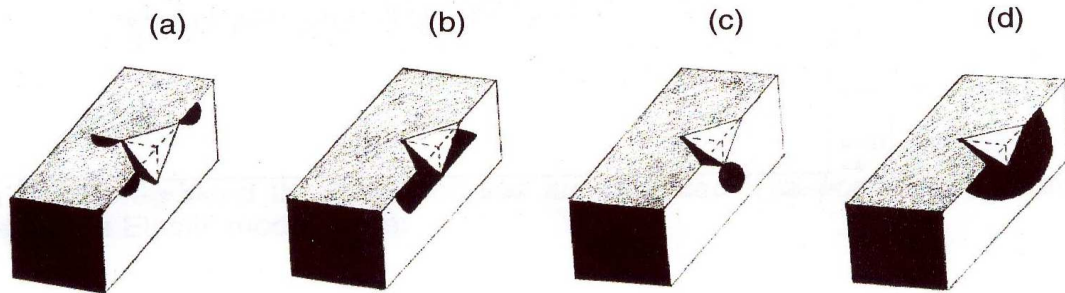
Figure 2.9 Cracks systems of Vickers indenter (the crack region is marked black) (a) radial cracks, (b) lateral cracks, (c) median cracks, (d) half-penny cracks.

The radial cracks are of particular importance, since their proximity to the surface has influence on the fracture strength of the specimen. To measure fracture toughness, these radials cracks are generated by making an indentation mark with a cube-corner indenter. The fracture toughness K_c can be calculated using the following equation:

$$K_c = a \left(\frac{E}{H} \right)^{1/2} \left(\frac{F}{c^{3/2}} \right)$$

(Eq. 2.18)

where E and H are the instrumented elastic modulus and hardness respectively, F is the applied load, c is the length of the radial cracks since the centre of the indent, and a is dimensionless empirical constant for the geometry of the tip used in the indentation experiment. For a cube corner tip the value is 0.032.

Figure 2.10 *SFM image of an indent on glass showing radial cracks.*

Despite its simplicity the nanoindentation test has several disadvantages. Firstly, the investigated material must be brittle, otherwise, there will not be a visible crack formation and the evalu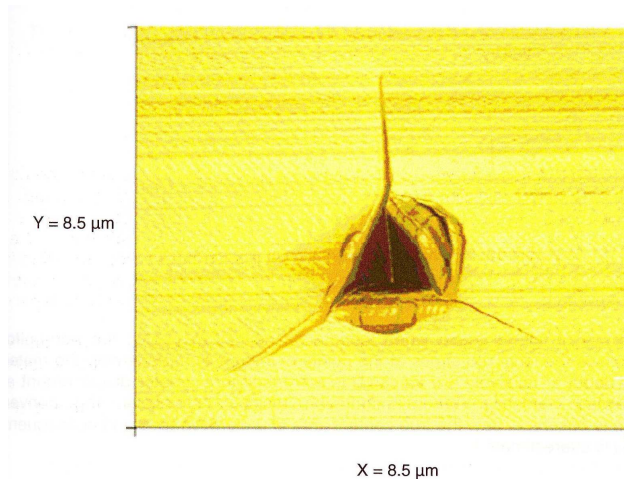ation of K_c will not be possible. Secondly, the differences between the measured values for the same material are usually quite significant. They depend on many different parameters (indenter size and type, indentation speed etc.). Finally, even well-described in literature Young modulus evaluation from nanoindentation data does not include the influence of an anisotropy. There are also problems with investigation of thin layers of soft materials (i.e. polymers).

2.4.2. Interface fracture strength measurements for thin films on substrates

Adhesion is a very important property of components not only in composite technology but also for microelectronics and emerging technologies such as microelectromechanical systems (MEMS). Therefore, there are more than one hundred different methods for measuring adhesion (especially in thin films) that employ different sample geometries. Some tests use continuous films, some require patterning, but all tests use some driving force or stored energy to achieve thin film delamination. The energy may come from the external mechanical force imposed on the measured sample, or it can be stored in the sample itself (e.g. through the film internal stress). These tests generally measure critical values of applied stress intensity or strain energy release rate. The most popular ones are:

Superlayer test

A test based upon internally developed stresses first proposed by Bagchi and co-workers [28]. Here, residual tensile stresses in a thin film line drive its delamination from a thick substrate. One of the way of achieving it is by increasing resulting film thickness by putting a thick overlayer (superlayer) on top of the tested structure. The superlayer increases the film total thickness and elevates the total residual stress without changing the tested interface. It is deposited at ambient temperatures (i.e. electron beam evaporation) and should not react with the tested film. **Fig.2.11** illustrates the test of adhesion force between a copper deposited on a substrate. In this case chromium was found to be the optimum superlayer. Firstly, a thin carbon release layer is thermally evaporated to act as a precrack. To avoid the edge effects on the energy release rate it is two times thicker than the Cu film. Furthermore, the Cu and the Cr superlayer are deposited and patterned to form strips perpendicular to the carbon lines. The debond energy is determined by the critical superlayer thickness.
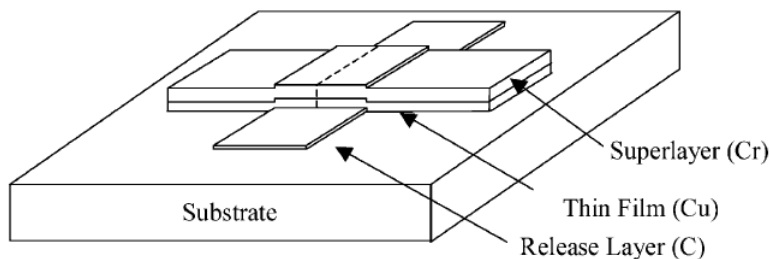
Figure 2.11 Superlayer test schematic. Residual tensile stresses in a thin film line drive its delamination from a thick substrate (Image source: [29])

Although, the superlayer test gives accurate adhesion energy values, the testing technique is rather tiresome and time-consuming. Several superlayer thicknesses have to be deposited before the lower and upper bounds of adhesion could be extracted.

Indentation tests

In the case of a brittle, weakly bonded film, indentation can be used to delaminate the film from the substrate, thus measuring the thin film interfacial strength [30-34]. Usually, the cone (plane stress) and the wedge (plane strain) are used for measuring brittle fracture of thin films adhesion by indentation. There are several models to investigate the indentation results and to evaluate the fracture strength of the interface or the strain energy release. For instance, Rosenfeld et al. [32] proposed following equation to calculate the strain energy release:

(Eq. 2.19)

$$G = \frac{0.627 H^2 h (1-v_f^2)}{E_f} \left(\frac{1}{1+v_f + 2(1-v_f)\frac{Ha^2}{P}} \right)^2$$

where E_f, v_f, and H are a Young modulus, Poisson's ratio and hardness of the tested film, respectively, a is the crack radius, h is the film thickness and P is the load.
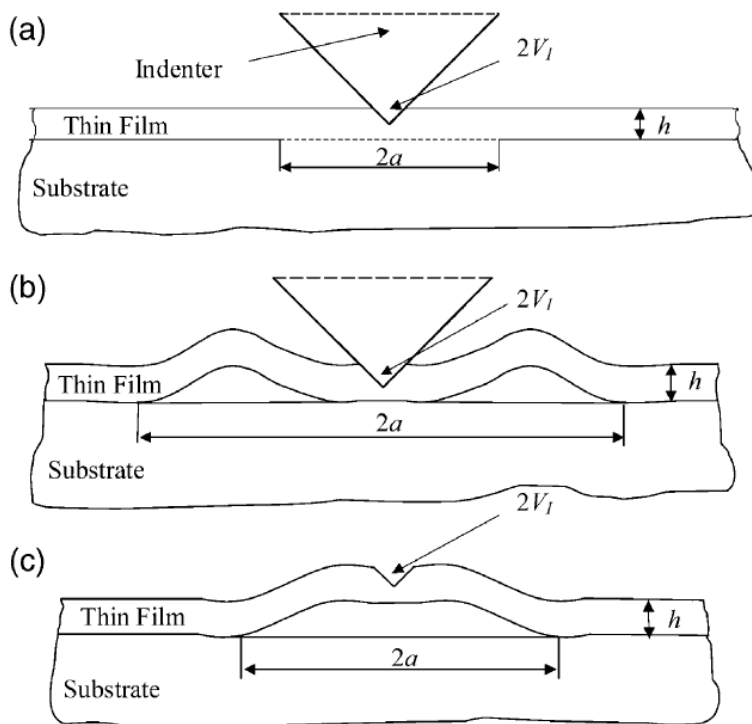
Figure 2.12 Different behavior of thin film during indentation tests. (a) no buckling during indentation; (b) double-buckling; (c) single-buckling after the indenter tip removal (Image source: [2.9])

Unfortunately, indentation tests cannot often be used to test adhesion of ductile films on brittle substrates. A ductile strongly adhered film often deforms before delamination from the substrate. Even if the film debonds from the substrate, delaminations are not reproducible. Moreover, the models used to estimate the strain energy release strongly influence the final results.

Scratch tests

In a typical scratch test a stylus or a diamond tip is drawn across the film surface. The test could be treated as a combination of two operations: normal indentation process and horizontal tip motion. A vertical increasing load is applied to the tip during scratching until the coating detaches from the substrate. The minimum

critical load P_c at which delamination occurs is used as a measure of the practical work of adhesion [35,36] :

$$P_c = \frac{\pi r^2}{2} \left(\frac{2EW}{h} \right)^{1/2}$$

where r is the contact radius, h is the film thickness, E is the Young modulus and W is the work of adhesion. This analysis can be applied only when the tensile stress normal to the film surface drives delamination.
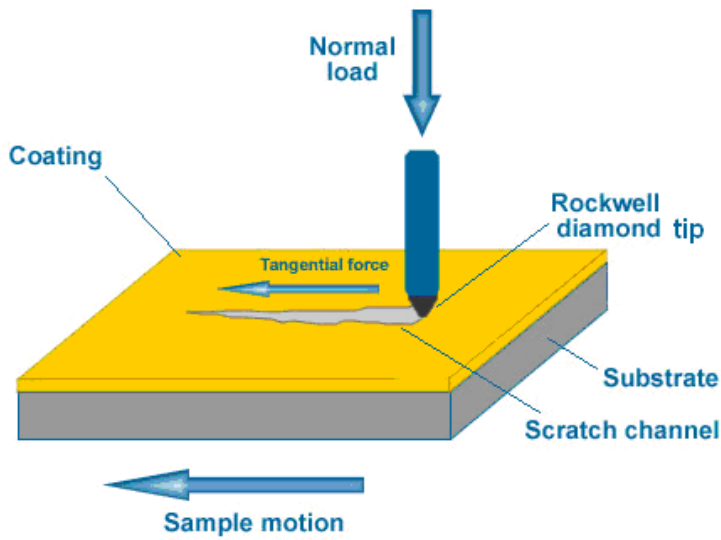
Figure 2.13 Schematic of the scratch test with Rockwell diamond tip. A stylus or a diamond tip is drawn across the film surface.

The main disadvantages of the scratch test are the necessity of special equipment, which is not as popular as i.e. nanoindenters or scanning force microscopes, and difficulties arise with studies of very thin films and soft materials.

2.4.3. Contact angle measurements

According to the acid-base theory of adhesion described in §2.1.4 it is possible to determine the work of adhesion between to different surfaces from the measurement of a contact angle.

The wetting of a solid surface by a liquid drop is expressed by Young's equation:

$$\gamma_S - \gamma_{SL} = \gamma_L \cos\theta_C$$

(Eq. 2.21)

where γ_S is the surface energy of the solid, γ_L is the liquid surface tension, γ_{SL} is solid-liquid interfacial tension and θ_C is the equilibrium contact angle (**Fig. 2.14**). Combining the **Eq.2.11** one obtains the Young-Dupré equation for the work of adhesion:

$$W_a = \gamma_L (1 + \cos \theta) \qquad \text{(Eq. 2.22)}$$

Further, from (2.22), (2.15) and (2.12):

$$\gamma_L(1+\cos\theta_C) = 2(\gamma_S^d \gamma_L^d)^{\frac{1}{2}} + 2(\gamma_S^+ \gamma_L^-)^{\frac{1}{2}} + 2(\gamma_S^- \gamma_L^+)^{\frac{1}{2}} \qquad \text{(Eq. 2.23)}$$

Hence, using three different test liquids it is possible to determine the surface tension components for the surface under test and therefore the total surface free energy.

$$\gamma_S = \gamma_S^d + 2(\gamma_S^+ \gamma_S^-)^{\frac{1}{2}} = \gamma_S^d + \gamma_S^{AB} \qquad \text{(Eq. 2.24)}$$

where γ_S^{AB} is the overall acid-base contribution to the surface free energy. Liquids usually used in three liquids method are: water, diiodomethane and glycerol.

This method may be used only to imprecise estimation of the interface strength. It does not take into consideration many more complicated processes and phenomena, which may take place while the interface is formed (i.e. internal stress). Nevertheless, as it will be shown further in this thesis, it may be extremely useful to qualitative explanation of influence of a chemical environment on the fracture strength of the interfaces.
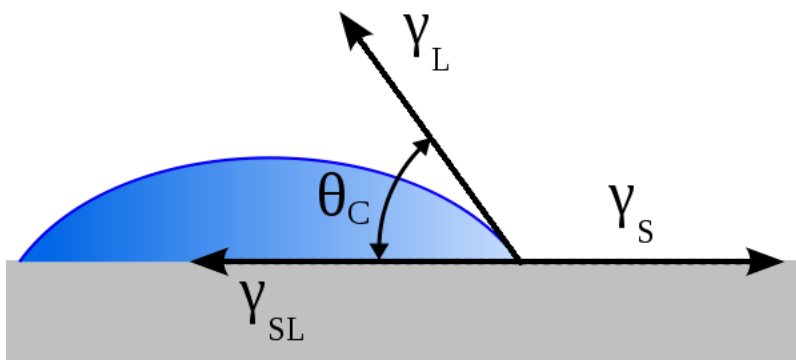

Figure 2.14 Definition of the equilibrium contact angle.

2.4.4. Fracture strength examination with nanopillars and other nanostructures

Sophisticated technological procedures and processes have recently allowed to produce structures of nanometer size. The development of modern measurement techniques and devices, such as scanning force microscope, has provided the tools to measure the properties of these structures. Therefore, it became possible to introduce measurement methods used in macroscale, to nanoworld. The fracture strength tests can also be conducted in this new area of scientific investigations.

The most popular device, which is used for mechanical testing in nanoscale is scanning force microscope (there is detailed description of this device in §4.1). Hirikata et al. [37] used SFM to study the interfacial strength between a submicron chromium dot and its silicon substrate (**Fig. 2.15**). The dot was removed by an SFM diamond tetrahedral-shaped tip, which was first engaged near the dot and then was dragged over it. The delamination area was imaged *in situ* after the test. The critical load at which delamination occurred together with the delamination area were used to estimate the interfacial strength.
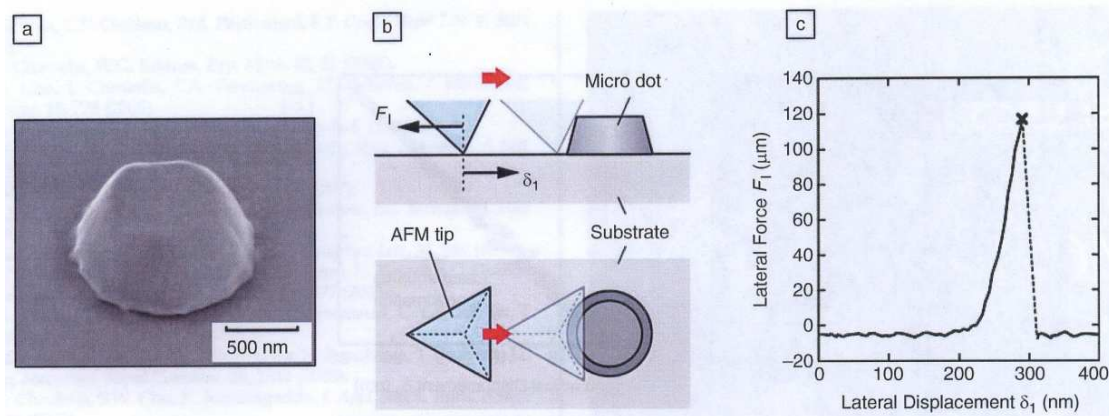
Figure 2.15 (a) Scanning electron microscopy image of a circular truncated cone-shaped chromium dot. (b) Schematic of an SFM tip dragging over the dot. The red arrow shows the direction of SFM tip motion, while the F_l is the lateral force experienced by the SFM tip. (c) The corresponding lateral force – lateral displacement curve. (Image source: [36])

Another approach to investigate fracture of materials and interfaces was applied by Baumeister et al. [38,39]. In her work, the idea to use SFM to exert forces on lithographically produced nanopillars, was described for the first time. During this

experiments, only the normal load was measured, hence, it was impossible to estimate the fracture strength of the investigated structures. The measurement took place only in water and a standard silicon tip was used. Nevertheless, it was shown that it is possible to remove selected nanopillar (**Fig. 2.16**) and it was proved that it is possible to apply well-defined forces to well-characterized nanometer-sized structures with varying geometrical and structural parameters.

Figure 2.16 Removing selected nanopillar. These experiments were first conducted by B. Baumsteier. The technique was further developed by A. Kaufmann. (Image source: [37])
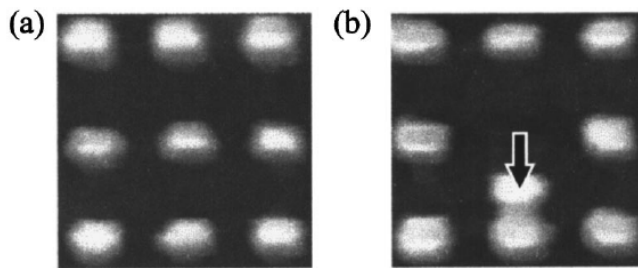
Significant improvements to this method were done by A. Kaufmann in his PhD thesis [40]. Instead of silicon tip, he used diamond covered tip, which is much more wear resistant. It allowed to conduct many experiments with the same tip and made the experiments reproducible. Furthermore, due to round cross section of pillars, it was not necessary to precisely align the samples. He conducted experiments in water as well as in ambient environment and in sodium chloride solutions, which showed many advantages in comparison to corresponding experiments in macroscale – especially much shorter time needed to investigate the influence of different chemical environment on silicon/silicon dioxide interface. Kaufmann in his thesis, also, firstly introduced experiments with pillars made of different materials than silicon and silicon dioxide. He investigated titanium(Ti)/polyamide(PI) nanopillars in order to examine whether water is responsible for the sporadic observed insufficient adhesion between Ti/PI or not. Unfortunately, however Kaufman realized that for quantitative approach to nanopillars experiments in different environments, lateral force measurements are necessary, in his work he still measured mainly the normal force. Therefore, he was not able to estimate the ultimate stress and compare the results for different size of nanopillars.

3.   Motivation and goals

The goal of this thesis is to develop and improve the measurement method of fracture investigation of nanopillars, which was firstly described by Baumeister [38,39] and then improved by Kaufmann [40]. The method should use the Scanning Force Microscope (SFM) tip to exert forces on well-defined structures with nanometer dimensions. (**Fig.3.1**). The forces and deflections of structures must be estimated with high accuracy. It should be able to investigate uniform nanopillars and also pillars which contains an interface between two different materials. Furthermore, it should be possible to investigate both brittle and ductile materials. Finally, the method ought to operate in different chemical environments, which is particularly important for corrosion studies. It would be also highly appreciated if other mechanical properties of materials (such as modulus of elasticity) can be determined from the data obtained during fracture experiments.
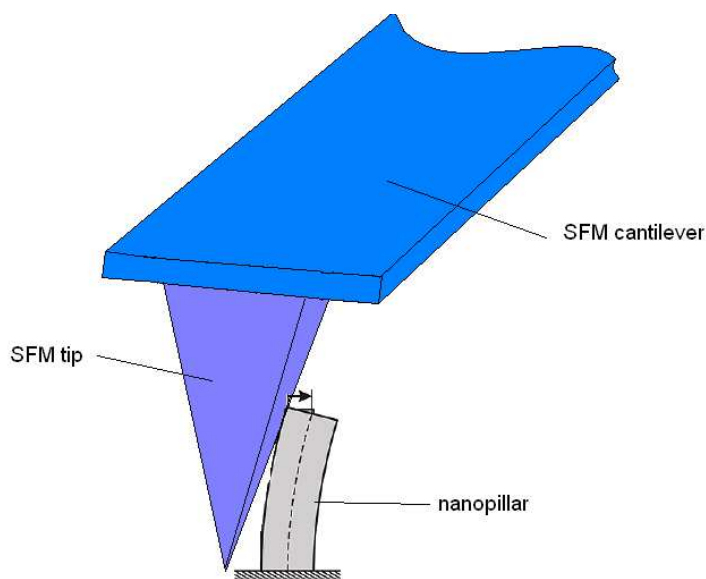
Figure 3.1 An idea of fracture strength examination with use of SFM. Schematic of fracture strength examination by bending a nanopillar with an SFM tip – not to scale. The SFM tip exerts well-defined forces on nanometer scale pillars. The pillars are bent, tilted and finally fractured.

The development of such technique will provide a unique platform for addressing a problem of fracture strength investigation of structures in range of nanometers and then investigation of some important problems in nanotechnology development, which are described below.

Based on the current state of the art in microelectronic technology and nanotechnology, three targeted scientific subtopics, which are subgoals of this Thesis can be identified:

i) Development of fracture mechanics of nanopillars,

ii) Investigations of the weakening / softening of polymers due to higher temperature

iii) Time dependent changes in mechanical properties in different chemical environments and modifications of elasticity and plasticity due to 'slow' processes like corrosion, solubilisation and the modification of the surface layer in Si/SiO_2 interface.

The development of such a portfolio of techniques in nano-fracture mechanics will provide a unique platform for addressing the challenge of fracture strength investigations for structures down to the range of some nanometers. This shall allow for the investigation of some important problems in nanotechnology and contribute to its ongoing development, as described below. This thesis is a direct continuation of the experiments with nanopillars described in §2.3.3. Nevertheless it provides significant innovations with regard to the measurement method, and the analysis of the results, also in conjunction with numerical models and simulations. It is this progress which now allows us to compare results with other methods (also with macroscopic experiments) for the first time.

3.1. Fracture mechanics of nanopillars

Materials Science has crucially contributed to the accelerated development of technological tools and devices and is mostly capable to predict materials properties, also including their failure mechanisms with good accuracy. Some challenges remain, however: (1) The mechanistic understanding of fracture on the atomic and molecular level e.g. at grain boundaries and interfaces, which is required for improving models and simulations; (2) The prediction of materials failure after long exposure to solubilizing, softening or corroding fluids i.e. gases and/or liquids.

In this context two important developments come together. Firstly, nanotechnologies have been made available to manufacture well defined model nanostructures with few to some dozens nanometers in dimension and nevertheless precisely predefined geometry. Secondly, experimental techniques have been developed to the extent that well defined experiments can be performed with forces acting on such model structures being simultaneously measured at very high (down to pN) precision.

This allows for 'Fracture Mechanics', the well-established discipline to be ported to nanostructures and enables radically new experiments: Most important is that by the scaling of fracture mechanics experiments the inherently slow mechano-chemical and mechano-physical procedures like fatigue or corrosion can be experimented with on a much accelerated time scale.

Previous experiments with nanopillars, described in §2.3.3, provided just the the very beginning of exploring a wide range of applications of nanoscale fracture experiments. There is still a necessity to develop techniques, which will give results comparable with macroscopic experiments in order to e.g. find out whether size effects occur, at which characteristic dimension(s), and how they are scaled. Furthermore, the technique must provide reproducible and accurate results which will not depend on the experimental setup. Therefore, the method of bending and fracturing nanopillars must be developed before experiments, which will provide answers to the important scientific and technological problems and can be routinely performed. The results gained by these newly developed techniques have to be compared in detail with other available experiments in order to assess the advantages and disadvantages of this approach, its imperfections and restrictions.

3.2.   Investigation of the weakening/softening of polymers

The fracture strength of nanostructures made of polymers plays an essential role in the development of modern nanofabrication processes for optical and electronic applications. It is particularly important for the development of the nanoimprint lithography process. In this process nanometer scale patterns are created by mechanical deformation of imprint resist and subsequent processes like mechanical reforming or tempering. Unfortunately, some difficulties still do not allow for this procedure to be used in mass production. For instance one of the problems is the destruction of polymer patterns during the demolding, i.e. the detachment of the mold from the molded structures. Using specific methods to investigate the fracture strength measurements and the bending of nanopillars fast measurements of different types of polymers are possible, to routinely find the best parameter set for the specific nanoimprint application or production batch. Furthermore, scanning force microscopy (SFM) is able to measure other mechanical properties of soft materials, hence, only

one experimental device can be used for many different experiments to characterize many different mechanical properties of the material. This is a particular advantage of the SFM technique and the progress reported in the rather short period elapsed during this PhD thesis project on nano-fracture mechanics experiments implies that more new modes will be developed in the future.

3.3. Time depended changes in mechanical properties (nanocorrosion and degradation processes)

Corrosion, as well as other degradation processes like the softening / hardening of polymers are very often misunderstood and mischaracterized which leads to inappropriate material choice for a particular application and consequent premature failure. Unfortunately, the damage caused by such degradation processes is extremely costly. For example, a major study, carried out in 1995 in USA, concluded that the cost impact of corrosion to this country's economy totalled nearly $300 billions annually [41]. Consequently, there is a constant need to perform experiments which will assess the corrosion and degradation of materials and structures in all fluids relevant for a specific construction or application. However, all conventional testing schemes require long testing times and are therefore expensive. This problem relates to the very long time needed to macroscopically observe the modification of materials – generally occurring at the surfaces or inside minute clefts, cracks or at grain / phase boundaries. By using scanning force microscopy for nanomechanical investigations on well defined sample structures with very small characteristic external dimensions, slow degradation processes can be quantitatively studied on a vastly accelerated time scale.

4. Description of method

This chapter provides the answers to the list of challenges to be overcome as described earlier in this Thesis. It describes the here developed method of fracture investigation by SFM in detail. In contrary to previous approaches to this problem, the described technique is able to provide results, which can be compared with macroscopic experiments. It not only provides the values of critical forces, which induce fracture, but also it evaluates the material properties such as fracture strength and the Young modulus.

4.1. Introduction to Scanning Force Microscopy

The scanning force microscope (SFM) is undoubtedly the most popular of the local probed devices. It allows quick access to a wide range of surface properties including mechanical, electrical, magnetic and other properties with high spatial resolution. Moreover, it can operate in many different environments including air, vacuum and liquids. The precursor to the SFM, the scanning tunnelling microscope (STM), was developed by Gerd Binnig and Heinrich Rohrer [42, 43] in the early 1980s at IBM Research – Zurich. STM earned its inventors the Nobel Prize for Physics in 1986. Binnig, Quate and Gerber invented the first scanning force microscope (also called atomic force microscope – AFM) in 1986 [44]. The first commercially available SFM was introduced in 1989. Since then, SFM plays an important role in development of nanotechnology.

4.1.1. Instrument

The **Fig.4.1** shows schematically how the SFM operates. The scanning probe is mounted on the free end of a silicon cantilever. The tip interacts with the surface of the measured sample. A laser beam reflects off the back of the cantilever which is deformed under the effects of interaction forces. The actual cantilever deflection and torsion are derived from the signal of a photoelectric cell divided into four sectors (**Fig.4.2**). The difference signals between coupled photodiodes are used as a control variable for adjusting cantilever height, i.e. for height signal ΔI_z:

$$\Delta I_z = \left(I_1 + I_2 \right) - \left(I_3 + I_4 \right) \text{ and}$$

$$\Delta I_L = \left(I_1 + I_4 \right) - \left(I_2 + I_3 \right)$$

for the lateral signal ΔI_L. I_1, I_2, I_3 and I_4 stand for the current from a corresponding diode. Furthermore, signals are normalized by the sum of all photodiode currents and used as the input signals in a negative feedback. Output signal of the feedback is then used to control the extension of the piezotube. On the end of the piezotube there is the cantilever's holder mounted. In the constant force scanning mode, the feedback tries to keep the deflection of the cantilever constant. In this case, differences in the extension of the piezotube are recorded as a sample's height. The SFM can record one or more characteristics of the interacting cantilever beam, e.g. deflection, torsion, amplitude of vibration etc. The system is able to work in air atmosphere, vacuum, liquids and it can be used for measurements at difference temperatures.
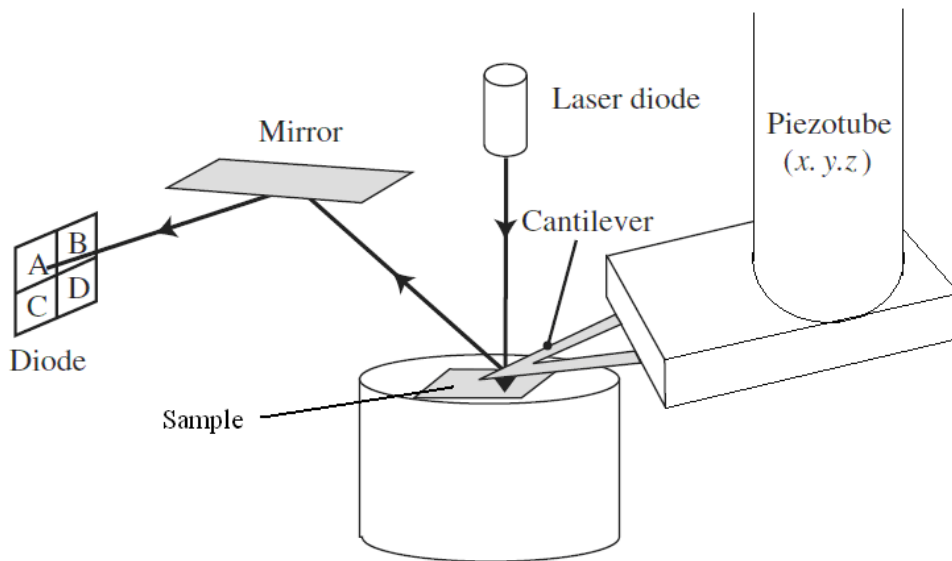

Figure 4.1 *Schematic diagram of a scanning force microscope. A piezotube displaces cantilever's holder. Deformations of the cantilever beam are determined by measuring the displacement of the light spot from the reflected laser beam by means of the system of photoelectric diodes*
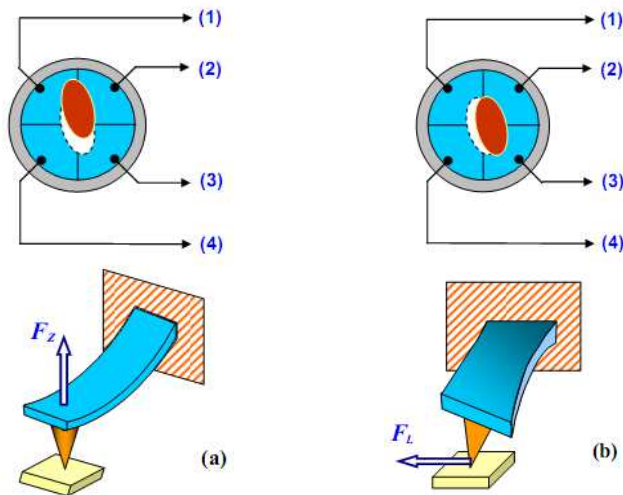
Figure 4.2 *Way of extraction of the actual cantilever deflection and torsion from the signal of a photoelectric cell divided into four sectors (1,2,3,4). F_z stands for a normal load and F_L for lateral load. (Image source: [45])*

The most important part of the SFM is obviously the cantilever with the tip. Several images of these components obtained by scanning electron microscope (SEM) are shown in **Fig. 4.3**. The spatial resolution of measurements is related to the radius curvature of the tip apex. Therefore, it is immensely important to miniaturize the dimensions of cantilever's beam and the tip. Cantilever is usually made of silicon or silicon nitride because in most cases processes developed for microelectronics are used to produce them. In certain cases special (reflecting, conducting) layer is deposited on cantilevers. The tip can be also covered with many different layers (polymers, diamond etc.) dependently on the application.
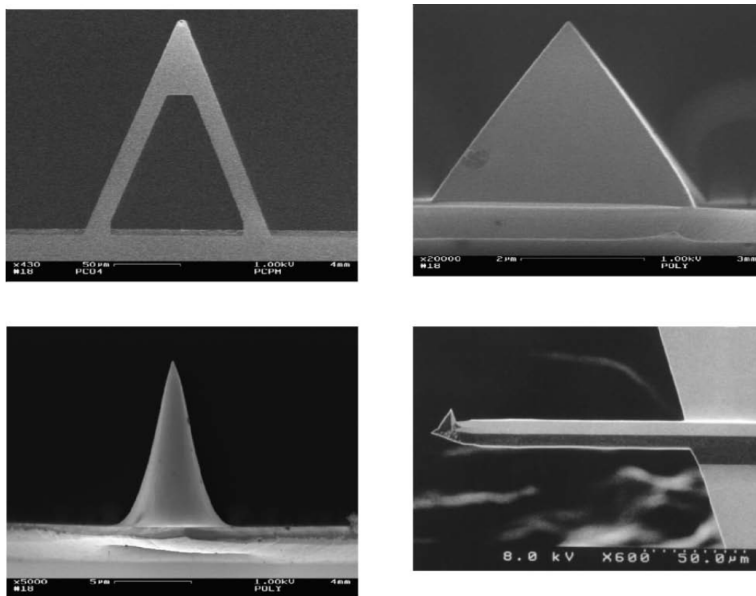

Figure 4.3 *SEM images of different SFM cantilevers (Image source: [46])*

4.1.2. Imaging modes

The interaction between SFM tip and the surface may be described by the Lennard-Jones (LJ) potential (**Fig. 4.4**):

$$U_{LJ}(r) = U_0 \left[\left(\frac{r_0}{r} \right)^{12} - 2 \left(\frac{r_0}{r} \right)^6 \right] \qquad \textbf{(Eq. 4.3)}$$

where U_0 is the depth of the potential well, r is the actual atom distance and r_0 is the distance at which the potential reaches its minimum. In this potential the r^{-12} term describes the repulsive forces whereas the r^{-6} term represents the attractive forces. Interaction is attractive at large distances due to van der Waals forces, and repulsive at very short range because of the impenetrability of the electron clouds associated with the two surfaces.

Contact mode

It is historically the first form of operation of an SFM. In this mode an SFM operates close to the repulsive edge of the potential – tip actually is constantly in contact with the surface. It is very fast and easy mode, however, due to wear and fracture it may change the scanned surface.

Friction mode

It is usually called friction force microscopy (FFM) or lateral force microscopy (LFM). Measurements are conduct in contact mode but the cantilever moves perpendicularly to its axis. In this case, friction forces cause torsion of the cantilever beam.

Tapping mode

This mode is also called quasicontact mode. The cantilever is made to oscillate at its resonant frequency with large amplitude; the mean position is close to the surface. In this case, forces applied to the surface can be immensely small and contact times so short that almost no friction occurs. Consequently, deformation of the sample can be avoided. Also phase difference between the excitation and the oscillation of the cantilever may be acquired. It corresponds to the energy dissipation of the system, which then can be used to characterize viscoelastic or plastic properties of the surface.

Force – distance curve

In this mode adhesion measurements or nanoindentation tests may be conducted. Cantilever approaches to the surface and its deflection is constantly measured. When the photodiode signal is saturated then the cantilever starts retracting. As a result force-distance curve is obtained. **Fig. 4.5** shows an example of such curve identified on hard, non-deformable material.
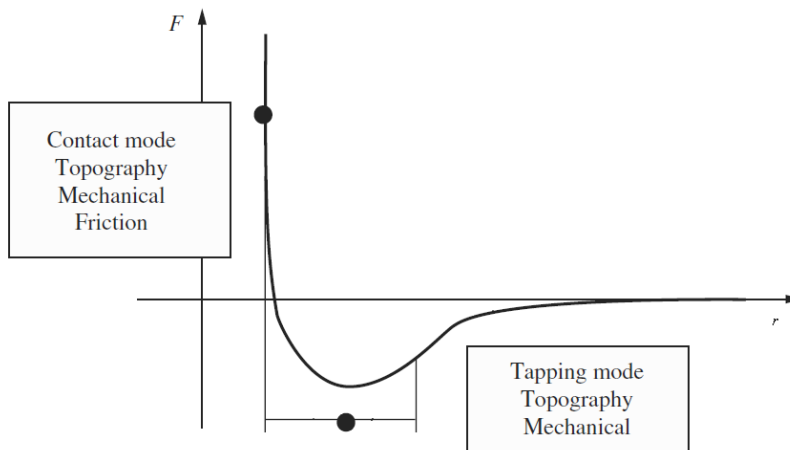

Figure 4.4 *Lennard-Jones potential. Black dots are two different SFM modes: contact mode, which is quasi-static and tapping mode, in which cantilever oscillates close to its resonant frequency. F – force, r – distance.*
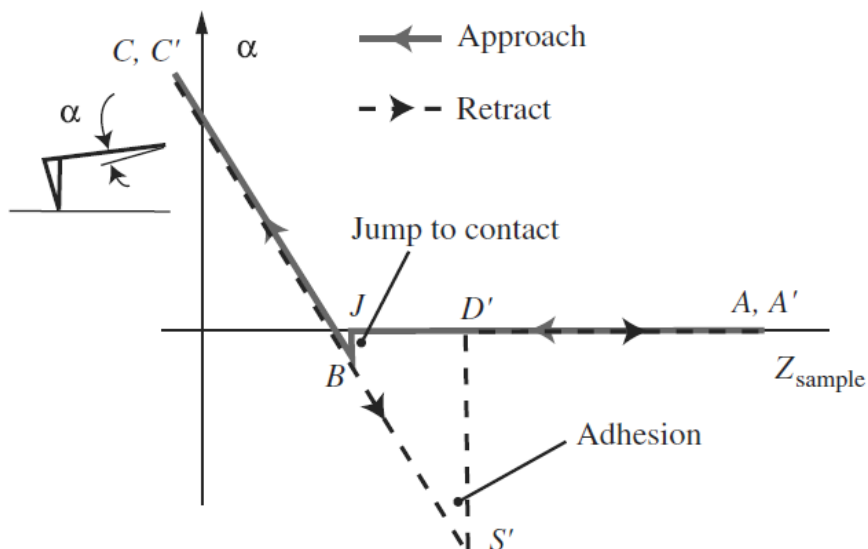

Figure 4.5 *An example of force-distance curve identified on hard, non-deformable material. (Image source: [46])*

4.1.3. Force measurement and calibration in contact mode

The measurable SFM signals come from the photo sensitive detector (PSD) and are current signals which are then converted into voltage. To convert these signals into a quantitative force values a precise calibration must be done. This has to be done independently for normal as well as lateral force.

In a normal direction the cantilever behaves analogously to a conventional spring and consequently, can be described by traditional Hook's law:

$$F_N = k_N \cdot \Delta z$$
(Eq. 4.4)

where F_N denotes the force, k_N is the spring constant and Δz means the displacement of the free end of the cantilever from its equilibrium position. Displacement Δz is determined by multiplying the deflection sensitivity (in nm/V) by the PSD signal difference between the state when cantilever is far away from the sample and when it is in contact with the surface (so called setpoint). If scanning is done in constant force mode, feedback assures that the setpoint is constant. The deflection sensitivity is derived from the force-distance curve measured on non-deformable material. In order to get the deflection sensitivity in nm/V, the piezotube must be calibrated.

The spring constant may be denoted by the cantilever manufacturer. Unfortunately, the nominal value may by much different from the real value. A more accurate method is given by [47] where the resonant frequency is used:

$$k_N \cong \frac{2\pi^3 w (f_0 L\sqrt{\rho})^3}{\sqrt{E}}$$
(Eq. 4.5)

where w stands for the width of the cantilever, f_0 for the resonance frequency, L is the length of the cantilever, ρ is the density ($\rho(Si) = 2336$ kg/m^3) and E the elastic modulus of silicon.

To determine lateral force so called friction loop is used (**Fig.4.6**). The cantilever moves over the sample with a 90° angle with regard to the scan direction forward and then backward. Its torsion is recorded and after one cycle friction loop is obtained. To derive exact value of lateral force friction loop must be centred and a calibration must

be done. In **Fig.4.6** *W* corresponds to the value of lateral force in arbitrary units. Lateral force in N may be calculated from the following equation:

$$F_L = \alpha \cdot W$$

(Eq. 4.6)

where α stands for a calibration constant. The determination of α uses the wedge calibration method from Varenberg et al [48], which is based on the method of Ogletree et al [49]. The so obtained calibration constant is only valid for the currently used setup i.e. the used cantilever and the position of the laser spot on it.
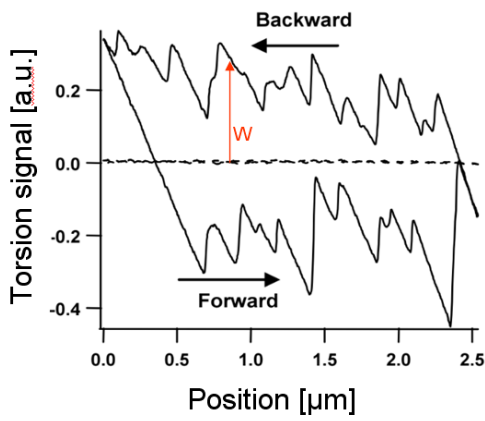

Figure 4.6 An example of a friction loop. The cantilever moves over the sample with a 90° angle with regard to the scan direction forward and then backward. Its torsion is recorded and after one cycle friction loop is obtained.

During the wedge calibration method two chemically identical surfaces which are arranged by a given angle θ (in radians) to each other are scanned (**Fig. 4.7**). For each surface the friction loop is obtained. In this case, friction loops are not centred so for both of them offsets can be evaluated. According to the **Fig.4.7** following expression can be found:

$$\sin\theta(L\cos\theta+A)\mu_s^2 - \frac{\Delta_s - \Delta_f}{W_s}(L+\cos\theta)\mu_s + L\sin\theta\cos\theta = 0$$

(Eq. 4.7)

The quadratic equation has two solutions but only the one which satisfies the $\mu < tan\theta$ condition is usable. With the derived friction coefficient for the sloped surface, the universal force factor α can then be calculated according to:
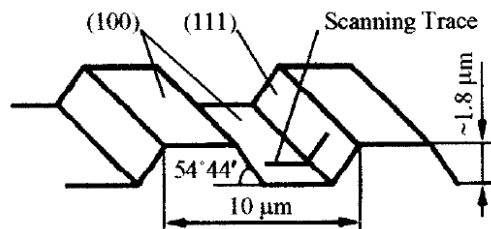
$$\alpha = \frac{\mu_s(L + A\cos\theta)}{W_s(\cos^2\theta - \mu_s^2\sin^2\theta)}$$

(Eq. 4.8)

With α every single scan point signal can be converted into a friction force F_L as long as the setup was not changed. Otherwise the system must be calibrated again. Through the relationship:

$$\mu = \frac{F_L}{F_N}$$

(Eq. 4.9)

(second law by Amonton) the friction coefficient can also be determined.
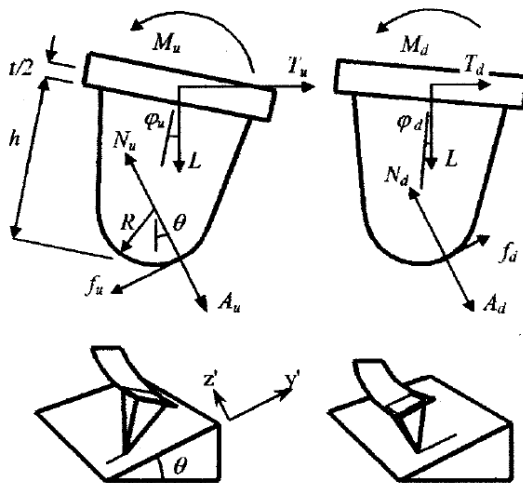
a)

Figure 4.7 Lateral force calibration method. (a) TGZ11 calibration structure, which provides two chemically identical surfaces, one flat and one angled. (b) Forces and moments, which act on SFM tip while scanning the angled surface. (c) Schematic of friction loops gained from the calibration experiment. (Image source: [48])

b)

c)

Topography

lateral signal

forward

backward

Cantilever position

W_s

Δ_s

W_f

Δ_f

θ
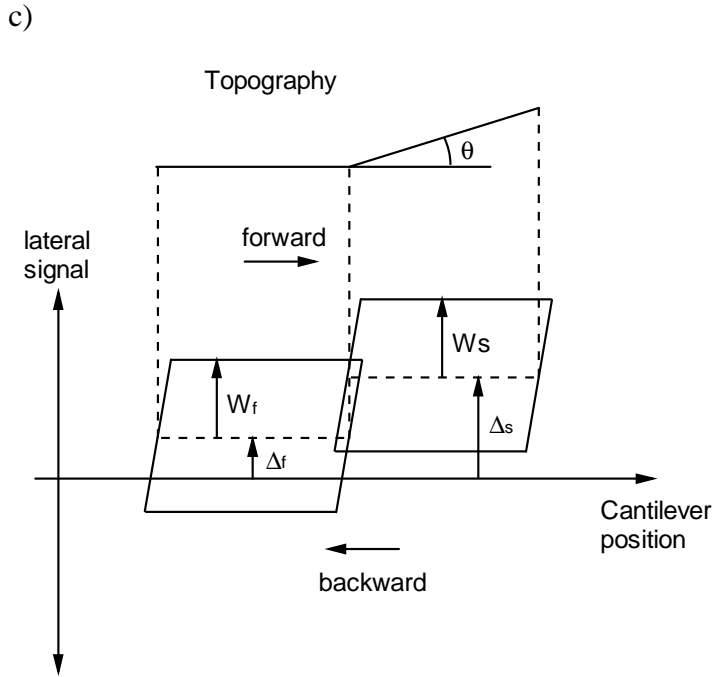
4.1.4. Determination of mechanical deflection

Particularly important for the experiments described in this thesis, where nanopillars will be bent and fractured by a tip of an SFM cantilever while scanning the nanopillars samples, is determining the deflection of nanostructures due to the applied, lateral force. Firstly, the deflection of the cantilever while scanning the edge of very stiff structure must be elaborated. In order to do that the commercial available calibration gratings TGZ3 (from NT-MDT) were used. An SEM image of such structure is shown in **Fig. 4.8**. With the assumption that the structures are perfectly stiff and does not deflect, it is possible to measure the deflection of the cantilever as a function of its position while scanning the step.

Figure 4.8 An SEM picture of the TGZ3 calibration grating (available from NT-MDT company) used for calibration of cantilever deflection.

While scanning nanopillars, not only cantilever bends but also the nanopillar. Therefore, it is possible to calculate the deflection of the nanopillar by simple subtraction as it is shown in **Fig. 4.9**.

Figure 4.9 Method of determining pillar's deflection. With the assumption that the calibration structures are perfectly stiff and does not deflect, it is possible to measure the deflection of the canti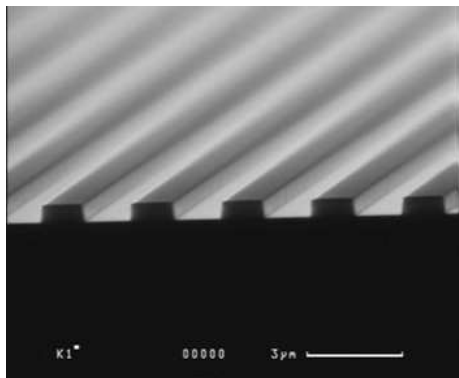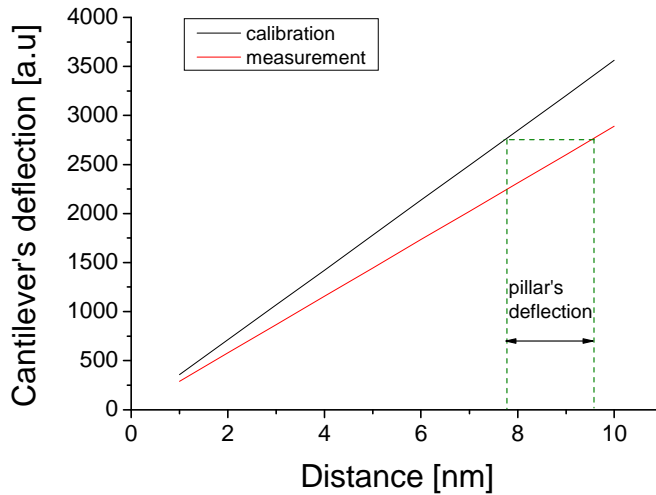lever as a function of its position while scanning the step. While scanning nanopillars, not only cantilever bends but also the nanopillar.

4.1.5. General principles of SFM tapping mode

The cantilever – the beam clamped at one end, may be a good mechanical oscillator with a low level of dissipation. Its resonant frequency is modified by interaction between a tip and a surface which was used in the SFM tapping mode. There are two techniques:

- AM-SFM – (amplitude modulated SFM) - cantilever is driven close to its resonant frequency and the variations of amplitude and phase are followed. Usually, feedback assures that the amplitude is constant and surface structure is measured. It is a very popular method, used also in this Thesis.

- FM-AFM – (frequency modulated SFM) – in this case a phase-locked loop holds the vibration amplitude and phase difference at pre-assigned values. It is mainly used in ultrahigh vacuum environment.

A very complete review of oscillating modes of SFM is described in [50].

Generally, the cantilever can be described as a beam that is clamped at one end while the other end is subjected to the force. In this case the analysis may be restricted to a

single mode for which the equation of motion can be very well approximated by the equation of a harmonic oscillator subjected to the force field:

$$\ddot{x} + 2\beta\dot{x} + \omega_0^2 x = F_0 \cos\omega t + \frac{f(d,t)}{m}$$

(Eq. 4.10)

where x stands for the displacement of the tip from its equilibrium position, ω_0 for the resonant frequency of the oscillator, F_0 for the amplitude of the excitation at frequency ω, β for a dissipation constant, m for the effective mass of the oscillator and the function $f(d,t)$ is the tip-sample interaction where d stands for the tip-sample distance when the cantilever is not deflected and t for time.

The **Eq.4.10** is linear and easy to solve when the interaction between the sample surface and the tip are non-dissipative and the oscillation amplitude is very low and far from the surface. Unfortunately, in quasi-contact tapping mode the tip usually vibrates close to the sample surface and the amplitude is significantly high which leads to non-linear equation.

In spite of the mathematical difficulties involved in solving analytically **Eq.4.10** several analytical approaches have been developed [51-53]. In specific cases numerical simulations must be done to determine amplitude-distance curves, average tip-surface forces, contact times and sample deformations. Additional problem is the existence of several oscillation states [54, 55].

4.1.6. Energy dissipation at the tip-surface contact in tapping mode

In [56] there is described an analytical relationship between the phase angle of the tip motion and the energy dissipated by the tip-surface forces. This model is based on the assumption that in the steady-state the average energy supplied to the cantilever per period (E_c) must be equal to the average energies dissipated by the inelastic interactions between the tip and the sample surface (E_{dis}) and by the viscous interactions with the environment (E_{visc}):

$$E_c = E_{visc} + E_{dis}$$

(Eq. 4.11)

where

$$E_c = \oint F_0 \cos \omega t \, \frac{dx}{dt} dt \qquad \text{(Eq. 4.12)}$$

$$E_{dis} = \oint f(d,t) \frac{dx}{dt} dt \qquad \text{(Eq. 4.13)}$$

$$E_{visc} = \oint - \frac{m \omega_0}{Q} \frac{dz}{dt} dt \qquad \text{(Eq. 4.14)}$$

where Q is the quality factor. Next, if we assume that the cantilever's deflection is quasisinusoidal, which, in fact is quite good approximation due to the high quality factor of the resonance, then the solution of the **Eq. 4.10** may be expressed as:

$$x = A \cos(\omega t - \varphi) \qquad \text{(Eq. 4.15)}$$

where A is the amplitude of the oscillations. In this case the energy dissipated by the interaction during one cycle can be expressed as:

$$E_{dis} = \frac{\pi k A_0 A}{Q} \left(\sin \varphi - \frac{\omega}{\omega_0} \frac{A}{A_0} \right) \qquad \text{(Eq. 4.16)}$$

where A_0 is the amplitude of free oscillations. Therefore, if the amplitude is held constant when a surface is scanned, then the phase shift between the excitation and the oscillation of the cantilever constitutes the energy dissipation due to the interaction between cantilever's tip and the sample surface.

4.2. Preparation of samples

4.2.1. Silicon and silicon/silicon dioxide nanopillars

The production of nanopillars follows a typical process scheme with lithography and pattern transfer (**Fig. 4.10**). For both kinds of samples Si (100) wafer was used as a substrate. For Si/SiO$_2$ samples the silicon surface was converted into SiO$_2$ in a low pressure vapour deposition (LPCVD) process, resulting in a homogeneous and dense

amorphous SiO$_2$ layer of defined thickness. For patterning, a polymethyl methacrylate layer was deposited on a wafer by spin-coating (used as positive resist) and arrays of nanopillars were produced by electron beam lithography (EBL) and subsequent wet development process in a polar solvent mixture (1:1 mixture of isopropyl alcohol (IPA) and methyl-isobutyl-ketone (MIBK)). For the experiments described here, orthogonal arrays with pillars of 100 to 200 nm diameter, 100 to 400 nm height and a pitch of 1 µm were used. Next, 20 nm chromium was evaporated in order to create a chemically resistant masking layer for reactive ion etching (RIE). The lift-off process was done in an acetone and dichloromethane bath. Eventually, the substrate was etched by RIE, using equal quantities of O$_2$ and CHF$_3$ at 100 mTorr in a 100 W RF plasma. By variation of the etching time different the height of the nanopillars was controlled, in case of the Si/SiO$_2$ samples this also lead to a controlled variation of the interface above the pillar base (here 30 nm). Finally, the chromium was removed entirely by a solution of perchloric acid (HClO$_4$) and ammonium cerium nitrate ((NH$_4$)$_2$[Ce$_2$(NO$_3$)$_6$]) in dionized water.
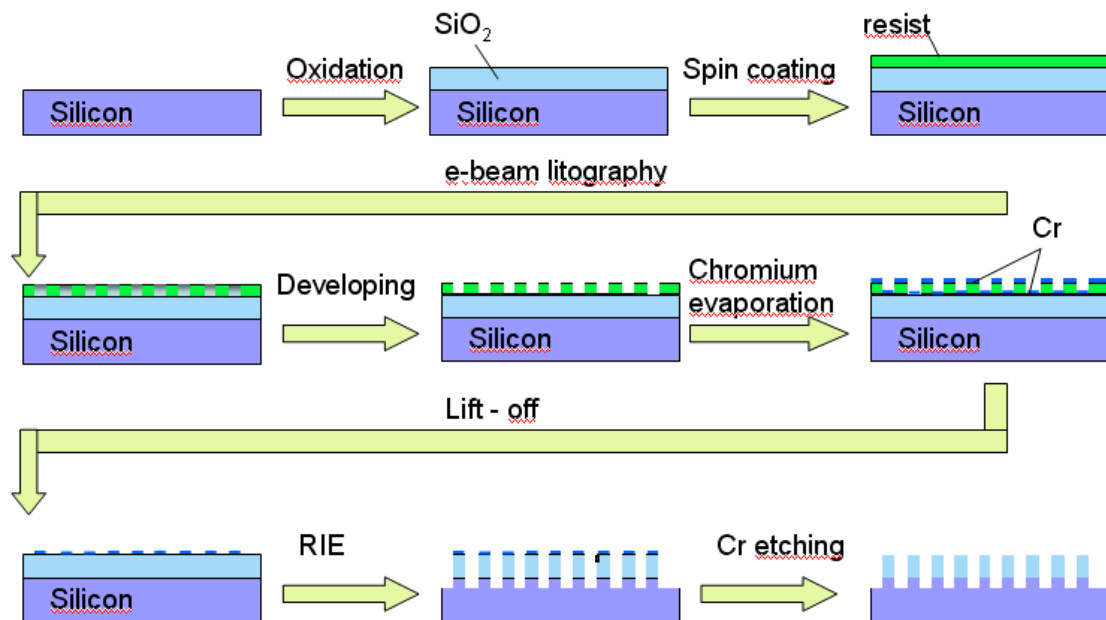

Figure 4.10 *Scheme of samples preparation procedure.*

In order to facilitate extensive studies with varied pillar dimensions and pillar height one mask had been developed with fields of pillars with different radius and

equal spacing. This mask was then used for manufacturing batches where the etch depth was carefully controlled, so a large portfolio of pillars with respect to diameter, height, material (Si, or SiO$_2$) and interface position within the pillar was available. The location of the pillar fields on the silicon wafer is shown in **Fig. 4.11**

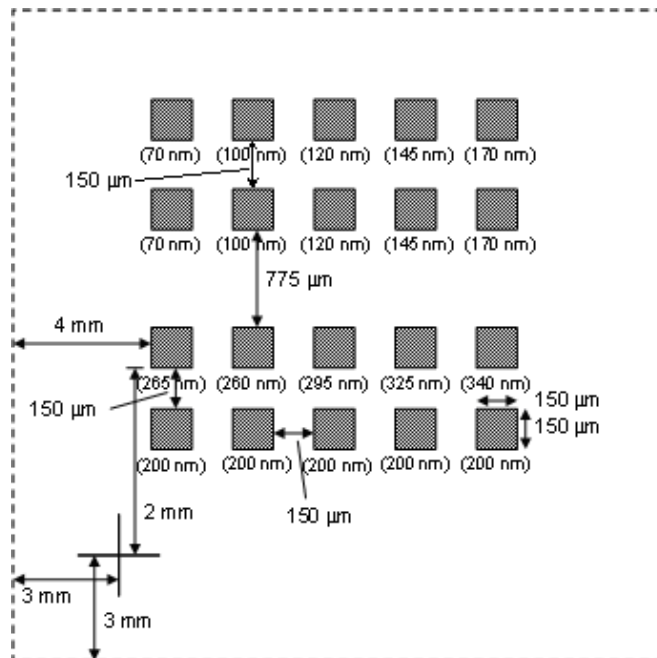*Figure 4.11 Position of fields of identical pillars with different diameters (in brackets) on a sample. Each field contained the same number of pillars at the same inter-pillar spacing.*

The SEM images of the nanopillars fields after SFM fracture experiments are shown in **Fig. 4.12**. The untouched nanopillars are shown in **Fig. 4.13**.
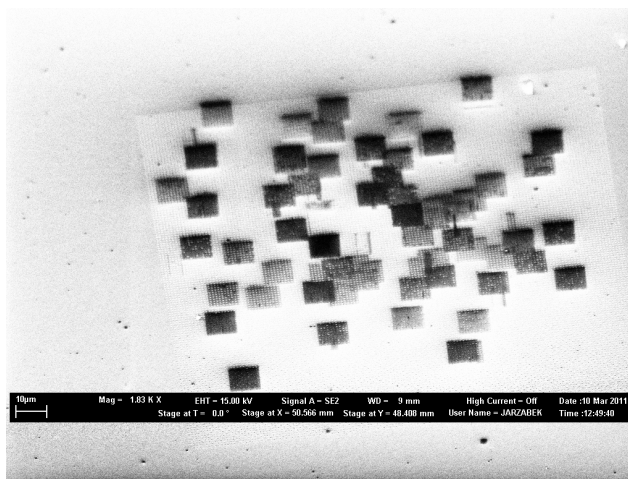

Figure 4.12 An SEM picture of one nanopillars field after many fracture experiments.
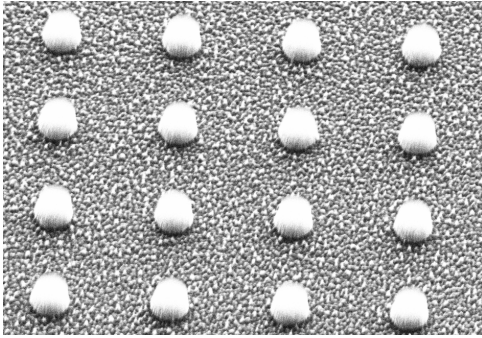
Figure 4.13 *An SEM picture of untouched Si/SiO₂ nanopillars.*

4.2.2. PMMA nanopillars

The polymer pillars were fabricated in 400 nm thick spincoated PMMA - Poly(methyl 2-methylpropenoate) - layer with a molecular weight of 25 kg/mol, by thermal imprint of a 20x20 mm^2 silicon mold with an array of 200 nm deep holes with different diameters ranging from 90 to 250 nm, during 10 min at an imprint temperature 180°C and a pressure of 25 MPa. In our experiments, silicon dioxide and silicon were used as mold materials. PMMA was chosen to fabricate the nanopillars due to its excellent properties for imprint lithography. PMMA has a small thermal expansion coefficient and a small pressure shrinkage coefficient.

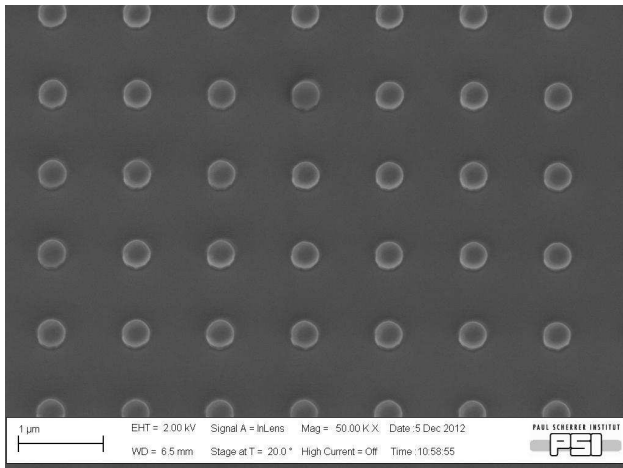The untouched PMMA nanopillars are presented in **Fig. 4.14**.

Figure 4.14 *An SEM image of as produced PMMA nanopillars with 150 nm in diameter and height of 220 nm.*

4.3. Fracture strength examination – brittle materials

4.3.1. Experimental setup

The Scanning Force Microscope (SFM) is used to perform experiments with forces in a wide range from low contact or intermittent contact forces for imaging to high contact forces inducing mechanical deformations of the nanostructures. Forces are exerted by the cantilever tip to sample pillars with dimensions of a few tens of nanometers while the cantilever deformations are monitored quantitatively by the same instrument.

Fracture experiments of nanopillars (**Fig.4.15a**) are carried out in the contact mode of SFM. Cantilevers coated with polycrystalline diamond (**Fig. 4.15b**) have been chosen for these experiments to assure high wear resistance. These coated cantilevers allowed for reproducible experimental results even in extended experimental sequences. The height of a tip is usually about 8 µm and it is much higher than the nanopillars (**Fig. 4.15a** and **4.16**). The cantilever moves across the sample surface with a 90° angle with regard to its long axis. This cantilever axis is bent by the feedback controlled force exerted onto the pillars in perpendicular direction of the surface, while frictional forces in lateral direction induce torsion of the cantilever beam which is the predominant cause of nanopillar fracture. Therefore, the calibration of the perpendicular and lateral forces exerted and measured in the SFM is essential for reproducible experiments (see §4.1.3.). The normal force has been directly adjusted via the setpoint of the feedback system. To appropriately set the lateral force the normal force as well as the scan velocity and feedback parameters has to be adjusted. Desired values of these parameters are obtained empirically. An example of these parameters, which was used to fracture Si/SiO_2 nanopillars are shown in Table 4.1
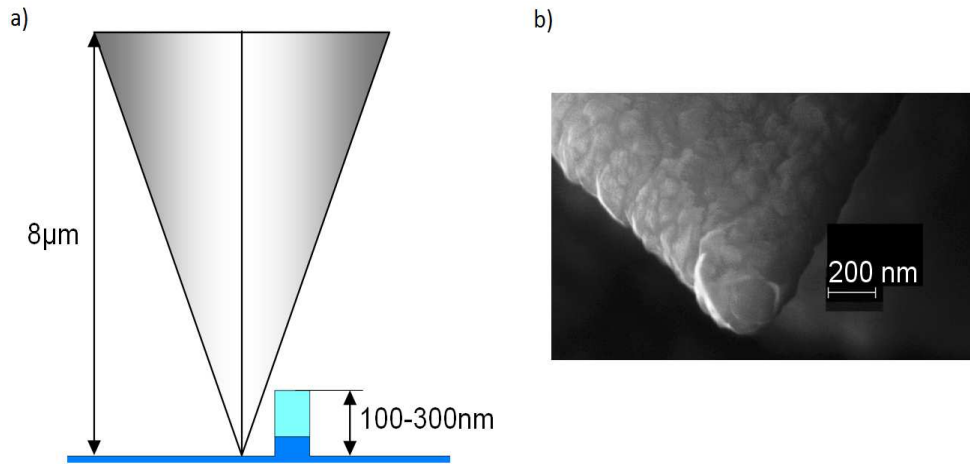
Figure 4.15 *Scheme of a tip and a nanopillar (a) and SEM picture of a tip (b). Nanopillars are much smaller than the SFM tip so it can be assumed that the same cantilever deflection induces the same lateral force which acts on nanopillars no matter how high they are. The tip diameter at the very end is usually about 100 nm as it can be seen in the SEM image(b).*
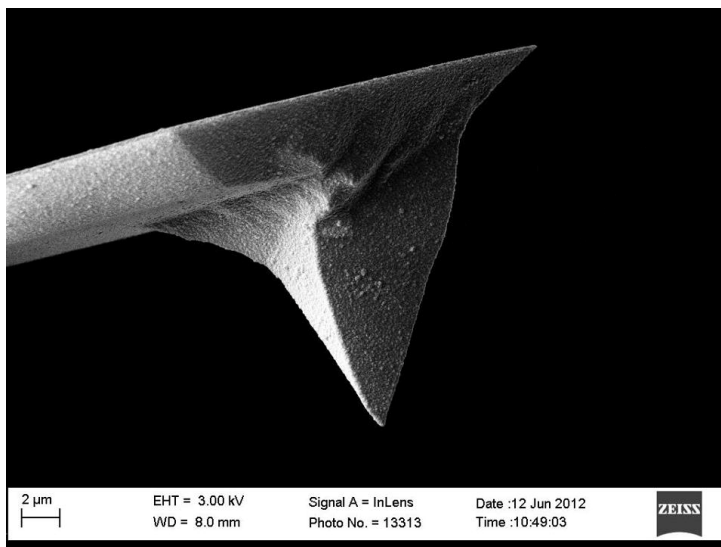
Figure 4.16 *SEM image of the tip used to fracture nanopillars. A nanopillar with typical dimensions is too small to be visible at this scale.*

Scan size (in µm):	10	Scanning field aspect ratio :	1:1
Scan angle:	90°	Scan rate (in Hz):	1.0
Tip velocity (in µm/s)	20.0	Data points/line:	512
Lines:	512	SPM feedback:	Deflection
P-Gain:	2.0	I-Gain:	3.0

Table 4.1 *Scanning parameters for fracturing of nanopillars made of brittle materials.*

The effect of scanning speed on the percentage of the fractured nanopillars is shown in **Fig. 4.17**.
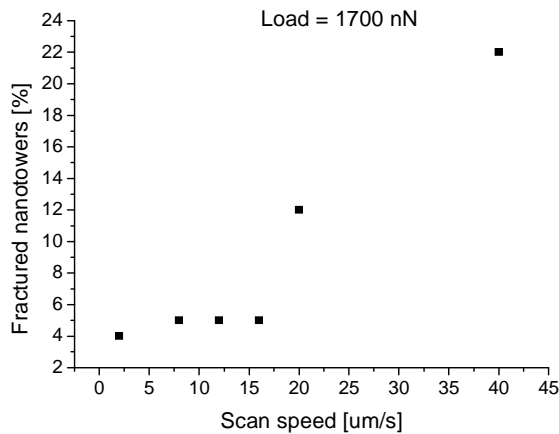
Figure 4.17 Influence of scan speed on the amount of fractured nanopillars. Due to higher velocity and the unmodified feedback parameters the lateral force, which acts on the nanopillars were higher and induced more fracture events.

Experiments have been performed with the two different types of nanopillars, manufactured as described in §5.1.1: silicon nanopillars and Si/SiO$_2$ nanopillars containing an interface between the SiO$_2$ cap on top of a Si bottom. SEM and SFM micrographs of 'as produced' nanopillars and their residues and stumps left after fracture are provided in **Fig. 4.18**

Figure 4.18 SEM picture of field of fractured nanopillars combined with a SFM micrograph of a part of this field. At the boarder of scanned field nanopillars debris may be observed.

4.3.2. Determination of Young's modulus

The main goal of this thesis is to establish a method for the measurement of the fracture strength of structures at the nanometer scale. However, before the SFM tip fractures a nanopillar, it bend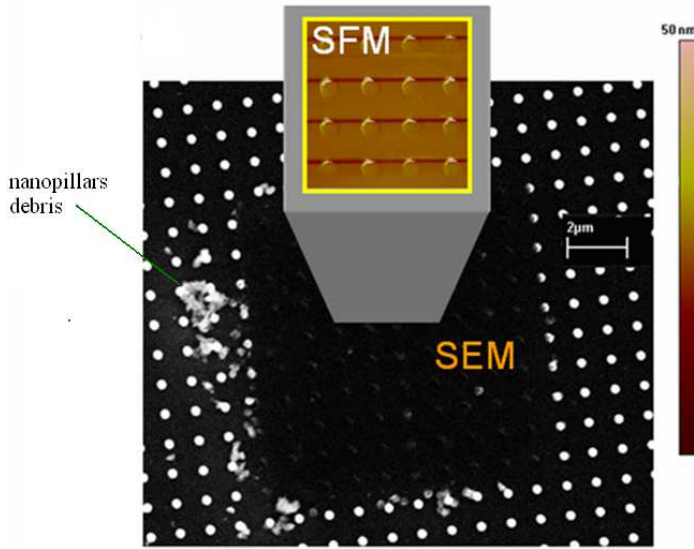s it. Therefore, it is possible to determine the Young modulus from the spring constant of bending. This is a straight forward analysis for pillars with an aspect ratio higher than 10 which are made of brittle materials. The deflection δ of bottom-fixed pillars in response to a lateral force F at the pillar top can be described, according to [57], by the following equation:

$$F = k_{bend}\delta = \frac{3\pi E D^4}{64H^3}\delta$$

(Eq. 4.17)

where k_{bend} stands for the spring constant of bending, E for Young modulus of the pillar's material, D and H for its diameter and height, respectively. Hence, the Young modulus:

$$E = \frac{64k_{bend}H^3}{3\pi D^4}$$

(Eq. 4.18)

Unfortunately, nanopillars investigated in this thesis usually have an aspect ratio lower than 10. In this case not only bending but also shear-induced deformation of

pillars occurs, therefore instead of classical Euler-Bernoulli beam theory, the Timoshenko beam theory [58] must be applied. The detailed derivation of the analytical formula for the bending of pillar with circular cross-section can be found in [59]. The shear-induced deformation is represented by an additional term in the deflection equation:

$$\delta = \frac{64FL^3}{3E\pi D^4} + \frac{\alpha FL}{GA}$$

(Eq. 4.19)

where α is the geometric coefficient, G is the shear modulus and A is the cross sectional area. According to [60], the α coefficient can be represented as a function of Poisson's ratio v:

$$\alpha = \frac{7 + 6v}{6(1+v)}$$

(Eq. 4.20)

and the shear modulus G for isotropic materials is defined as:

$$G = \frac{E}{2(1+v)}$$

(Eq. 4.21)

therefore, for an isotropic material deflection equation **4.19** is as follows:

$$\delta = \frac{64FL^3}{3E\pi D^4} + \frac{4(7+6v)FL}{E3\pi D^2}$$

(Eq. 4.22)

For an anisotropic crystals Young modulus may be approximated, according to [61], from the following equation:

$$\frac{1}{E_{\alpha\beta\gamma}} = S_{11} - 2\left[(S_{11} - S_{12}) - \frac{1}{2}S_{44}\right](l^2m^2 + m^2n^2 + l^2n^2)$$

(Eq. 4.23)

where:

$$l = \cos\alpha \quad m = \cos\beta \quad n = \cos\gamma$$

(Eq. 4.24)

56

are 'direction cosines' – cosines of the angles between the direction of interest and x,y,z axes (<100> direction).

To determine the force applied to a nanopillar and its deflection, methods described in §4.1.3 and §4.1.4 were used in this Thesis. To accurately determine the material's Young modulus more precise measurements are needed than during fracture, therefore the scan field was minimized to study only a few nanopillars with higher accuracy for such experiments. In the general case of the fracture investigation experiments presented in this thesis one hundred nanopillars are treated in one scan.

4.3.3. Bending and fracturing of a single nanopillar

The fracture of single nanopillars is induced and analyzed while simultaneously the perpendicular force and the lateral force (**Fig. 4.19**) are measured. In the experiments, it was observed that the lateral force just before fracture, is typically close to five times higher than the normal force. Note that the normal force acts towards the sample surface so it is not the predominant first reason to induce nanopillar fracture. It is predominantly the lateral force which is responsible for bending and twisting of the nanopillars.
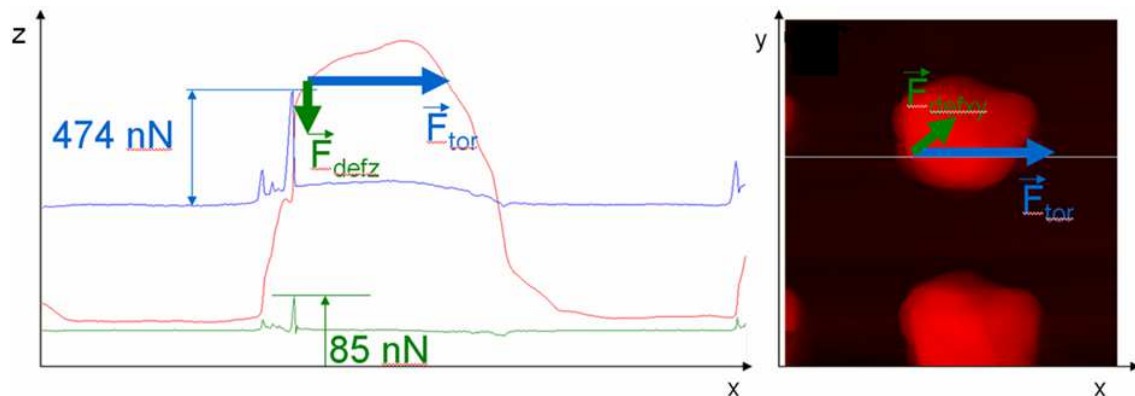
Figure 4.19 *Deflection and torsion of a cantilever can be studied in one scan, which are caused by normal and lateral force respectively. In the graph (right part magnified single pillar) the red line describes topography, the blue line represents the torsional signal and the green line represents the deflection signal. The lateral force is almost 5 times higher than normal force. The view of the nanopillar showed in the SFM micrograph here is not cylindrical because of the high scan velocity and low feedback parameters which are essential to exert forces strong enough to fracture pillars. Detailed studies of nanopillars by SEM showed that nanopillars are almost perfectly cylindrical.*

The measured fracture thresholds together with the well-known geometry and architecture of the nanopillar allow us to calculate stress distribution profiles with the finite element method (FEM). Thereby the location and the threshold values for the critical situation initiating the fracture process can be determined for differently structured and differently processed nanopillars. The results of the FEM analysis of the stress distribution for a single nanopillar are shown in **Fig. 4.20**. In this simulation perfectly cylindrical, homogeneous nanopillars are assumed. Furthermore, the experimentally determined threshold forces to induce are used as external constraints for the FEM calculations. Threshold forces are identified as maxima in the scan lines of the lateral force by identification of the contact point of the cantilever as determined from the time of fracture and the position of the cantilever in the scanned frame. The distribution of maximum principal stress within the nanopillar has been calculated and the maximum value reached within the geometrical structure has been associated with the initiation of the fracture incident. Except for the contact point where erosion takes place, the highest stress appears invariably at the base of the nanopillar. In good agreement with this FEM analysis, all the bulk Si nanopillars without interface have been observed to be fractured at the base and pillars containing interface were fractured just at this interface.
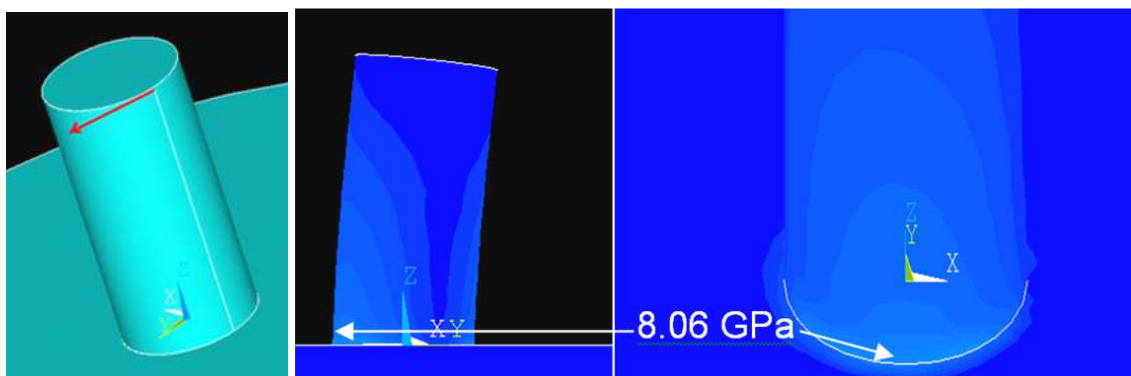

Figure 4.20 *Finite element method simulation results of bending a silicon nanopillar. The distribution of maximum principal stress within the nanopillar has been calculated and the maximum value reached within the geometrical structure has been associated with the initiation of the fracture incident. The exact parameters of the simulation are shown in Appendix 1.*

4.3.4. Statistical approach to analyze the fracture of nanopillars

To precisely evaluate the fracture strength of the measured nanopillars with low measurement errors, it is favourable to analyze many fracture incidents under identical conditions. For this purpose a 10x10 μm field with one hundred nanopillars was scanned (**Fig. 4.18**). The data acquired during such scan frames allows for the analysis of the variation of maximum lateral forces as they act on the nanopillars when they are exposed to cantilever tips exerting perpendicular forces set and held constant by the controller. Also the same data is used for the evaluation of the lateral force peaks associated with the individual fracture incidents. Variations of the fracture threshold are caused by small differences in the shape and the surface roughness of the nanopillars and consequent changes of the contact region with the tip. As result of the fracture debris is produced (**Fig. 4.21**) as it can be observed by SEM.
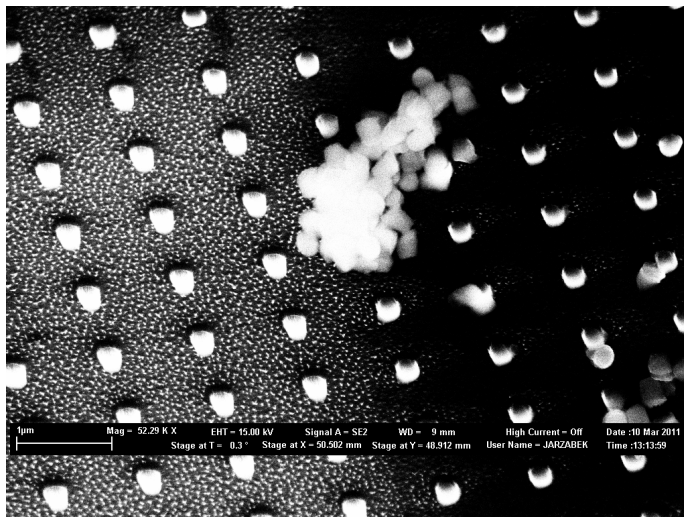
Figure 4.21 Debris of fractured nanopillars piled up at the border of a scanned area. Note that also fractured left and intact nanopillars can be discriminated in the SEM data.

Generally in fracture mechanics, specifically here in nanoscale fracture mechanics it is very important to establish the best possible force measurement and force calibration methods. In order to measure lateral forces with the use of SFM, friction loops described in detail in §4.1.3, were performed during each experiment. In **Fig 4.22** a typical 'friction loop' is shown (see blue (trace) and green (retrace) line profiles). The peaks and the valleys of these lateral force signals correspond to the rising and falling edges of the nanopillars with respect to the scan direction. During one scan of a selected frame there are 512 lines and 512 friction loops. The average maximum

lateral force is the average of 100 local maxima in the lateral force landscape acquired during the experiment. This is because there are 100 nanopillars in one scanning field.
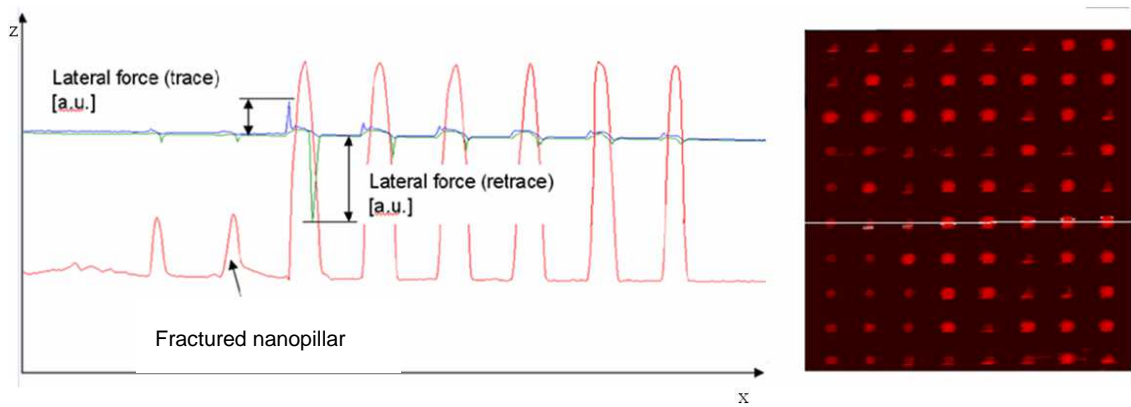

Figure 4.22 *Typical friction loop with peaks corresponding to the lateral force, which acts on a pillar. From the red line (topography) it can be seen that two first pillars were fractured at the interface.*

Firstly, a low 'imaging' normal force scan is performed. Furthermore, the normal force is increased and the fracture occurs. The number of fractured nanopillars is determined by counting incidents in a second observation scan with the imaging force set to a low 'imaging' normal force level. In a series of experiments the normal force is increased after each scan of a certain sample of nanopillars . Thereby it is possible to measure the fracture threshold distribution for example due to manufacturing irreproducibilities. The data gained from many of these experiments taken at different normal forces is plotted in a graph showing the percentage of fractured nanopillars on the ordinate and the average maximum lateral force on the abscissa (x-axis) (**Fig. 4.23**). This graph is fitted by a Boltzman sigmoidal function:

$$y = \frac{A_1 - A_2}{1 + e^{(x-x_0)/dx}} + A_2$$

(Eq. 4.25)

where $A_1 = 0$, and $A_2 = 100$ are fixed parameters; x_0 and dx are fitted parameters. The parameter x_0 is the inflection point of the sigmoid and its value is the statistically relevant value of the force to be taken to the FEM analysis to evaluate the fracture strength of the measured nanopillars. The parameter dx informs about the difference between the force which fractures all nanopillars and the force which is too small to fracture any of the nanopillars (this variability in the measurement results from (1)

60

defects in the nanopillar internal structure – (2) small differences with nanopillars shape - and (3) random measurement errors). Note that the systematic measurement errors, after careful calibration as described in the experimental part, are typically an insignificant factor compared to *dx*.
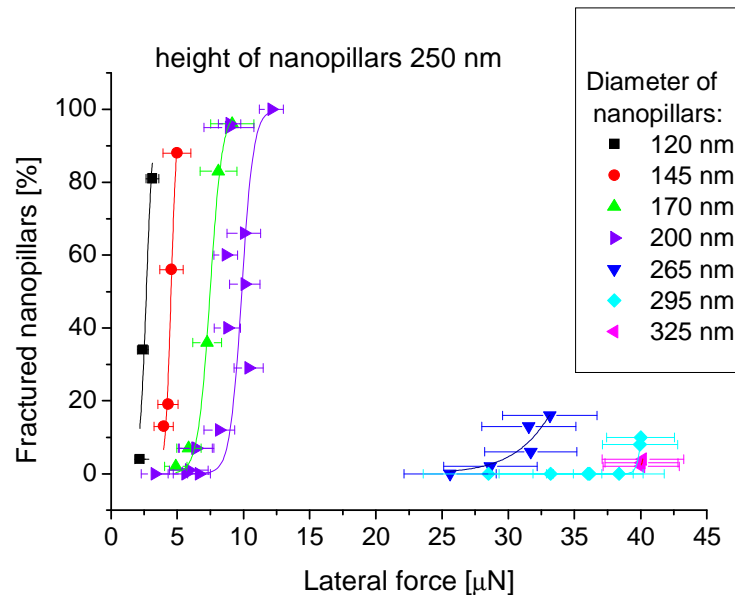
Figure 4.23 *The data gained from many of fracture experiments taken at different normal forces is plotted in a graph showing the percentage of fractured nanopillars on the ordinate (y-axis) and the average maximum lateral force on the abscissa (x-axis) for different diameters of the pillars. These graphs are fitted by a Boltzman sigmoidal function.*

4.4. Fracture strength examination and mechanical properties of ductile materials

4.4.1. Materials

Due to the high importance of polymers in many technology areas a polymer material was sought for to perform nano-fracture mechanics experiments. Due to its widespread application in semiconductor manufacturing and the thereby well established lithographic procedures, PMMA - Poly(methyl 2-methylpropenoate) (**Fig. 4.24**) – nanopillars were chosen and fabricated in order to investigate ductile fracture.

The description of the stress-strain behaviour of polymers is similar to that of metals, but a very important consideration for them is that the m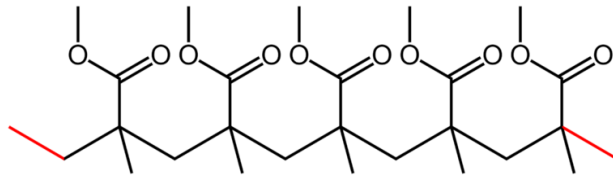echanical properties depend on strain rate, temperature, and environmental conditions. The stress-strain can be brittle, plastic and highly-elastic (elastomeric or rubber-like). In general, decreasing the strain rate has the same influence on the stress-strain characteristics as increasing the temperature: the material becomes softer and more ductile. Therefore, before fracture experiments, modelling of stress distribution in polymer nanopillars and computing fracture strength, the mechanical and rheological properties (Young modulus and viscosity) of the investigated material in current state must be elaborated. Fortunately, these properties can be investigated easily by SFM.

4.4.2. Mechanical model for the deformation of PMMA nanopillars

The testing of polymers requires unique understanding of the viscoelastic nature of these materials. Therefore, a precise model should be evaluated before the experiments. The simplest, however, still very accurate mechanical models for viscoelastic behaviour of materials during the tests described in this thesis, consist of two elements: a spring for elastic behaviour and a damper for viscous behaviour. In this work, simple 2- parameters Maxwell fluid model ([12]) (**Fig. 4.25**) was used.

Figure 4.25 Maxwell model of viscoelasticity. (source: [12])

The constitutive equation in this case is:

(Eq. 4.26)

$$\sigma + \frac{\eta}{E}\dot{\sigma} = \eta\dot{\varepsilon}$$

where σ is stress, ε is strain, E is the Young modulus and η is the viscosity of the material. According to this model, bending of a polymer nanopillar cannot be described simply by **Eq. 4.19**. In this case, instead of Young modulus, the relaxation modulus should be used. It can be obtained from **Eq.4.26** if the applied strain is written as follows:

$$\varepsilon(t) = \varepsilon_0 H(t) \tag{Eq. 4.27}$$

where H(t) is the Heavyside function and is defined as:

$$H(t) = 1 \quad \text{for } t > 0 \tag{Eq. 4.28}$$

$$H(t) = 0 \quad \text{for } t < 0$$

The solution of (4.18) for such strain is

$$\sigma(t) = \varepsilon_0 E e^{-t/\tau} \tag{Eq. 4.29}$$

where

$$E(t) = E e^{-t/\tau} \tag{Eq. 4.30}$$

is called the relaxation modulus and

$$\tau = \frac{\eta}{E} \tag{Eq. 4.31}$$

Finally, the bending of polymer nanopillar can be described as follows:

$$\delta = \frac{64 F L^3}{3 E e^{-t/\tau} \pi D^4} + \frac{2\alpha F L (1+v)}{E e^{-t/\tau} A} \tag{Eq. 4.32}$$

where α is the coefficient, which can be determined from (**Eq. 4.20**).

In the case of bending of nanopillars with SFM and yield strength determination the time dependence of Young modulus may be omitted but to properly describe and model behaviour of polymers in other processes the viscosity must be known. There are several methods to determine the viscosity and the Young modulus of thin polymers

films including recent one proposed by the author [9-12]; however, nanopillars induce a new approach to this problem. In macroscale viscoelastic properties are often determined with stead state oscillation or vibration tests[1] using small tensile (comprehensive) bars, thin cylinders or flat strip in torsion, beams in bending etc. Therefore, due to nanopillars and tapping mode of the SFM it is possible to transfer this method to the nanoscale. If we assume that a small uniaxial sample is loaded with a strain input, then:

$$\varepsilon(t) = \varepsilon_0 e^{i\omega t} \qquad \textbf{(Eq. 4.33)}$$

where ω is the angular frequency. It should be noted that the transient terms associated with starting up an oscillatory loading have decayed and are neglected as they are inertial terms. In this case the stress $\sigma(t)$ is also of exponential form:

$$\sigma(t) = \sigma^* e^{i\omega t} \qquad \textbf{(Eq. 4.34)}$$

where σ^* stands for a complex quantity. It can be further defined

$$\sigma^* = \varepsilon_0 E^*(i\omega) \qquad \textbf{(Eq. 4.35)}$$

such that the stress can be rewritten as

$$\sigma(t) = \varepsilon_0 E^*(i\omega) e^{i\omega t} = E^*(i\omega)\varepsilon(t) \qquad \textbf{(Eq. 4.36)}$$

where $E^*(i\omega)$ stands for the complex modulus and can be decomposed into real and imaginary part as

$$E^*(i\omega) = E'(\omega) + iE''(\omega) \qquad \textbf{(Eq. 4.37)}$$

The real part is defined as the storage modulus $E'(\omega)$ and the imaginary part is defined as the loss modulus, $E''(\omega)$. In the case of the Maxwell model of viscoelasticity the storage and loss moduli are:

---

[1] This approach is usually referred to as dynamic mechanical analysis (DMA) testing.

(Eq. 4.38)

$$E'(\omega) = \frac{\dfrac{\eta^2}{E}\omega^2}{1 + \dfrac{\eta^2}{E^2}\omega^2} \qquad E''(\omega) = \frac{\eta\omega}{1 + \dfrac{\eta^2}{E^2}\omega^2}$$

There is the phase lag between strain vs time and stress vs time plots due to the complex modulus resulting from **Eq.4.36**. Therefore, by plotting stress and strain on mutually perpendicular axis and combining respective points in time as shown in **Fig.4.26** the hysteresis loop can be observed. The area inside the hysteresis loop represents of the energy dissipated during the cyclic deformation.
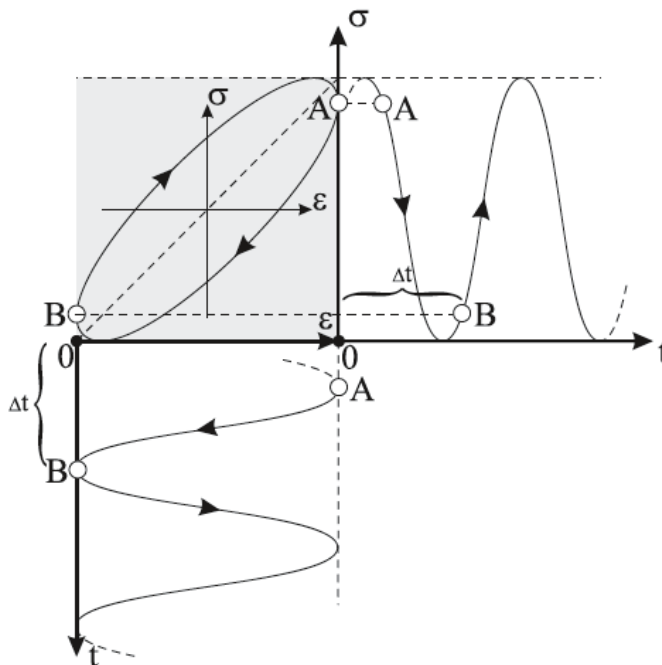
Figure 4.26 *Formation of the hysteresis loop for a polymer as visualized by graphical combination of the stress and strain values parametrically. The dashed line inside the hysteresis loop represents the pure elastic response. (source: [12])*

The dissipation can be shown to be proportional to the loss modulus using the basic relationship between the work and energy. Recall that the work per unit volume of a stressed material is given by:

$$W = \int \sigma d\varepsilon = \int_0^t \sigma \dot{\varepsilon} dt$$

(Eq. 4.39)

If the material behaves in a perfectly elastic manner, the deformation energy supplied to the material during the loading is stored in stretching of the molecular configuration changes. Hence, it recovers completely upon unloading – there is no energy dissipated. Therefore for a single complete cycle of oscillatory loading of any material (elastic or

not), the net energy stored is zero, as the material is loaded and unloaded symmetrically. The amount of the energy per unit volume dissipated in a single oscillatory loading E_{dis} can thus be calculated by integrating the **Eq. 4.39** over a complete cycle:

$$E_{dis} = \oint \sigma d\varepsilon = \int_0^{2\pi/\omega} \sigma \dot{\varepsilon} dt \qquad \text{(Eq. 4.40)}$$

For a viscoelastic material from the **Eq.4.36** results:

$$\sigma(t) = E'(\omega)\varepsilon(t) + \frac{E''(\omega)}{\omega} i\omega\varepsilon(t) = E'(\omega)\varepsilon(t) + \frac{E''(\omega)}{\omega} \dot{\varepsilon}(t) \qquad \text{(Eq. 4.41)}$$

To calculate the energy per unit volume dissipated over a cycle, **Eq. 4.41** can be substituted in **Eq. 4.40**. Using a sinusoidal strain ($\varepsilon(t)=\varepsilon_0 sin\omega t$), it can be shown that:

$$E_{dis} = \int_0^{2\pi/\omega} \left(E'(\omega)\varepsilon(t) + \frac{E''(\omega)}{\omega} \dot{\varepsilon}(t) \right) \dot{\varepsilon} dt = \varepsilon_0^2 \pi E'' \qquad \text{(Eq. 4.42)}$$

4.4.3. Experimental setup

In the case of bending and fracture of polymer nanopillars also Contact Mode Scanning Force Microscope was used. The only difference was in the scanning parameters. Due to much lower forces needed to bend the pillars and their yielding it was necessary to reduce the velocity of the cantilever's tip and increase the feedback parameters. Therefore, the scanning size was also smaller to reduce a time of a single experiment (**Tab. 4.2**).

Scan size (in µm):	5	Aspect ratio:	1:1
Scan angle:	90°	Scan rate (in Hz):	1.0
Tip velocity (in µm/s)	5.0	Data points/line:	512
Lines:	512	SPM feedback:	Deflection
P-Gain:	3.0	I-Gain:	3.3

Table 4.2 *Scanning parameters for viscoelastic materials*

The second part of the experiments with the nanopillars made of polymers are the measurement of viscosity in the SFM tapping mode. Unfortunately, oscillations of the cantilever depends on interaction with the measured structures. Therefore, to determine the desired properties of the nanopillars, a model of these interactions must be developed. In this work the model described in §4.1.6 is used. According to **Eq.4.34** the energy dissipated in a nanopillar in a single oscillatory loading is equal to:

$$E_{dis} = \varepsilon_0^2 \pi E'' V = \frac{A^2 \pi^2 D^2}{4L} E''$$

(Eq. 4.43)

where V is the volume of single nanopillar, D is its diameter and L its length. The strain may be determined easily from the amplitude of the oscillations A:

$$\varepsilon_0 = \frac{A}{L}$$

(Eq. 4.44)

According to **Eq.4.16** and **Eq.4.43** the loss modulus can be determined from:

$$E'' = \frac{4kA_0 L}{\pi QAD^2} \left(\sin\varphi - \frac{A}{A_0} \right)$$

(Eq. 4.45)

The viscosity can be determined from the quadratic **Eq. 4.38**:

$$\eta = \frac{E^2 \left(1 \pm \sqrt{1 - \frac{4(E'')^2}{E^2}} \right)}{2E''\omega}$$

(Eq. 4.46)

4.5. Restrictions and the measurement error

4.5.1. Reference measurements using silicon nanopillars

Silicon is an element which plays an extremely important role in the modern electronics so its properties have been investigated thoroughly with high accuracy by many scientists and different methods. Moreover, its processing is a standard procedure in every nanotechnology laboratory. Therefore, the first samples, which were

investigated by the above described method, were nanopillars made of silicon. The results obtained from the experiments can be then compared with the theoretical predictions, finite element simulations and the well-known values of silicon Young modulus and fracture strength. The comparison can be useful to determine the accuracy of the method and its restrictions.

Silicon has a regular crystal structure (**Fig. 4.27**), which is one of the reasons it is such an excellent engineering material. It is an anisotropic crystal, so its properties are different in different directions in the material relative to the crystal orientation, however, it has cubic symmetry so its stiffness tensor has only 3 independent values (**Tab. 4.3**).
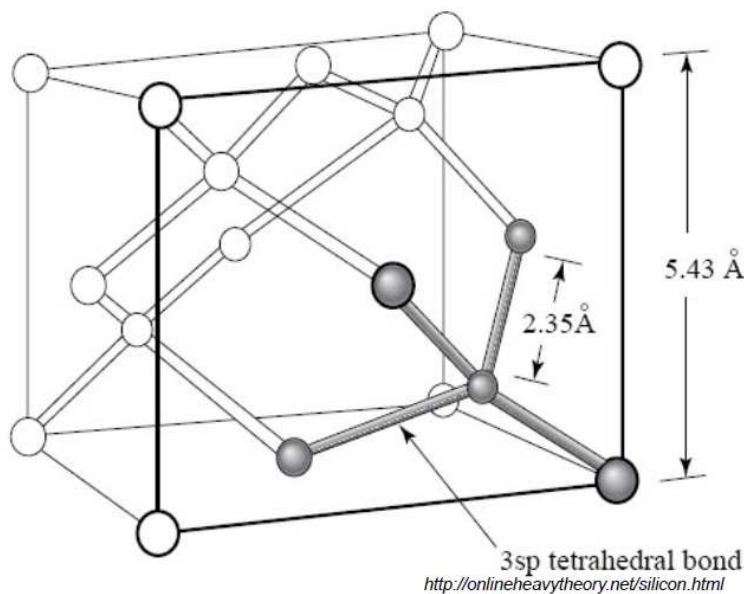
Figure 4.27 Silicon crystal structure (source: [62])

	C_{11}	C_{12}	C_{44}
C [GPa]	165.7	63.9	79.9

Table 4.3 The 3 independent values of stiffness tensor of silicon (C_{11},C_{12},C_{44}) according to: [63]

The nanopillars were fabricated on the silicon (100) surface. They were bent and fracture according to the procedure described above. The results achieved for bending of a typical nanopillar (height: 250 nm, diameter: 90 nm) are plotted in **Fig. 4.28**. Due to

the high resolution of Scanning Force Microscope, the deflection measurement error is about 3 nm. The deflection determined from the experiment is compared to the deflection evaluated from the **Eq.4.19** and from the finite element method (detailed parameters of the FEM simulation are described in Appendix 2). The Young modulus used in **Eq.4.19**, according to the **Eq. 4.23** equals 130 GPa. In this case, there is a perfect agreement with the experiment, Timoshenko theory and FEM simulation. Unfortunately, it was possible to collect only 3 different measurement points because for higher forces the pillars were fractured.

The different situation is shown in **Fig. 4.29**. In this case the nanopillar with 150 nm in diameter and height of 250 nm were investigated. The measurement results agree with the FEM simulation but the Timoshenko beam theory predicts almost two times lower deflection. The main reason for this difference is the fact that pillars with aspect ratio lower than 2 cannot be modelled as beams. Finite element method analysis is capable of dealing with different 3D structures and gives much better results. Pillars also were stronger so many measurement points were collected.

The used SFM was not able to proper measure the deflections lower than 3 nm therefore in case of thick pillar with 250 nm in diameter (aspect ratio equal to 1) measurement data are much different either from the Timoshenko beam theory and FEM simulations (**Fig. 4.30**).
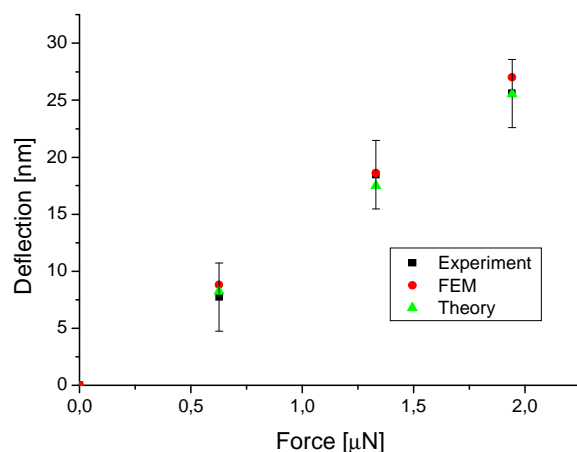

Figure 4.28 Results of bending of a typical silicon nanopillar. The results of the experiment are compared to the FEM simulation and the Timoshenko beam theory. There is a very good agreement between the experiment, theory and simulations.
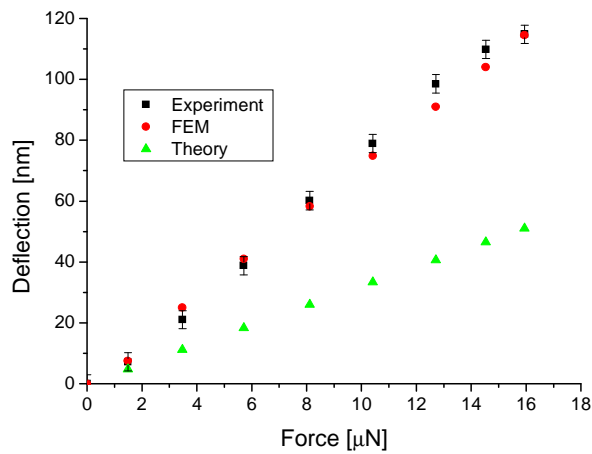
Figure 4.29 *Deflection of thicker pillars (aspect ratio between 1 and 2) cannot be described by the Timoshenko beam theory.*
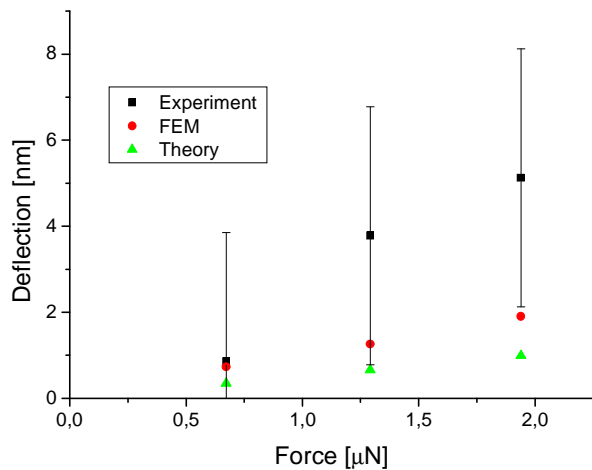

Figure 4.30 *In case of nanopillars with aspect ratio below 1 the deflection is too low to measure it properly with used SFM. Probably also other phenomena (i.e. indentation) occur here.*

Another problem with estimating the bending of a nanopillar by the Timoshenko's theory is the indentation of the nanopillar by the SFM tip due to high stress, which occurs at the contact point. The indentation depth is usually in the range of a few nanometers in case of silicon nanopillars, hence, it has a minimal influence on thin pillars, which deflection is significantly larger. Unfortunately, for thick pillars, the indentation depth may be larger than the deflection. In this case it is possible to elaborate more sophisticated FEM analysis but in this thesis only the case of the point load instead of the SFM tip and constantly elastic material were taken into consideration. The results of one of these simulations are shown in **Fig. 4.31**. The blue colour corresponds to the maximal displacement. The simulation allows also to evaluate the influence of Young modulus of the measured pillar on the indentation depth. For pillars with aspect ratio larger than 2 and two different Young moduli (200 GPa

and 10 GPa) the indentation depth is always smaller than 10% of the deflection. The situation drastically changes for pillars, which diameter and height are equal. In this case, the tip's indentation is about 10 times larger than the deflection of the pillar for 10 GPa Young modulus of the material. Despite many simplifications used in the simulation it shows certainly that the nanopillars with aspect ratio lower than 2 made of soft materials cannot be investigated with the above described procedure. On the other hand, in case of the nanopillars made of stiff materials, the main reason of the measurement error is the lateral resolution of the SFM, which should be high enough to accurately investigate immensely small pillars deflections.
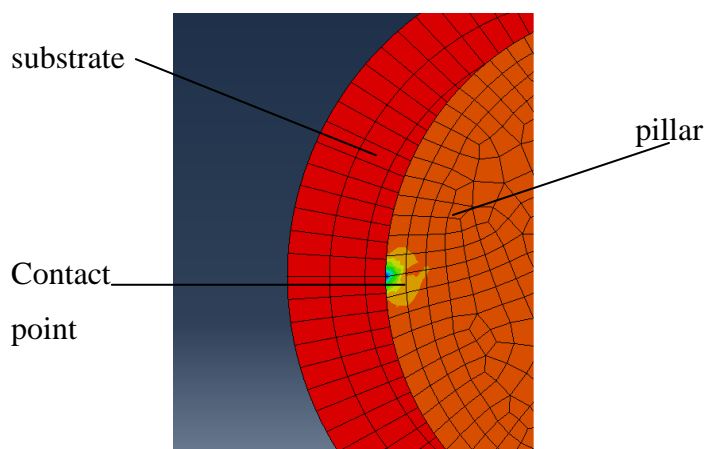

Figure 4.31 The results of FEM simulation of tip indentation into a single nanopillar. The mesh is thicker in the contact point between a tip and a pillar. Different colors correspond to different nodes displacement. The biggest displacement is exactly at the contact point.

Furthermore, the method of fracture strength investigation, described in details in §4.2, was used to measure the fracture strength of silicon nanopillars. Nanopillars with different diameters (from 200 nm to more than 300 nm) and height equal to 400 nm were used in order to find out if there is any influence of the size on measured properties. From the statistical analysis of fracture events performed with Si nanopillars, a fracture strength consistent with table values for silicon was determined. When measuring fracture thresholds of smaller diameter nanopillars one could expect that surface energies modify the energetic of the fracture process in some analogy to the discussion about the hardness increase at low loads. The data show that for silicon structures with diameters larger than 100 nm such a trend was not observed.

In **Fig.4.32b** the experimentally observed fracture strength is plotted for nanopillars in dependence of their diameter. The red line corresponds to the tabulated fracture strength of silicon. The experimentally determined threshold stress to induce fracture is about 8 GPa, similar to the fracture strength of silicon of about 7 GPa as it has been determined from macroscopic experiments [5.1]. The experimentally observed

fracture strength for Si nanopillars is without exception lying above this line. It probably the result of deviation to inaccuracies related to the nanopillar shape and possible systematic errors consequent to inaccurate calibration and the imperfection of FEM model (§4.5.3) as well as the random error. Moreover, the processing of the nanopillars may also influence the fracture strength of silicon. Nevertheless, the structures measured in this work are extremely small compared to the structures measured in classical fracture tests. This thesis presents a reliable method to probe sample volumes of down to cubic nanometers and interfacial crossections down to 50 by 50 nm which is a fraction of 0.01 compared to commonly used fracture mechanics tests and can not be expected to provide results of accuracies comparable to macroscopic methods. However, measurement error in this experiments is never higher than 30%. The results accuracy can be further improved by developing more precise lateral force calibration methods (i.e. force calibration with use of springs with well-known spring constant).
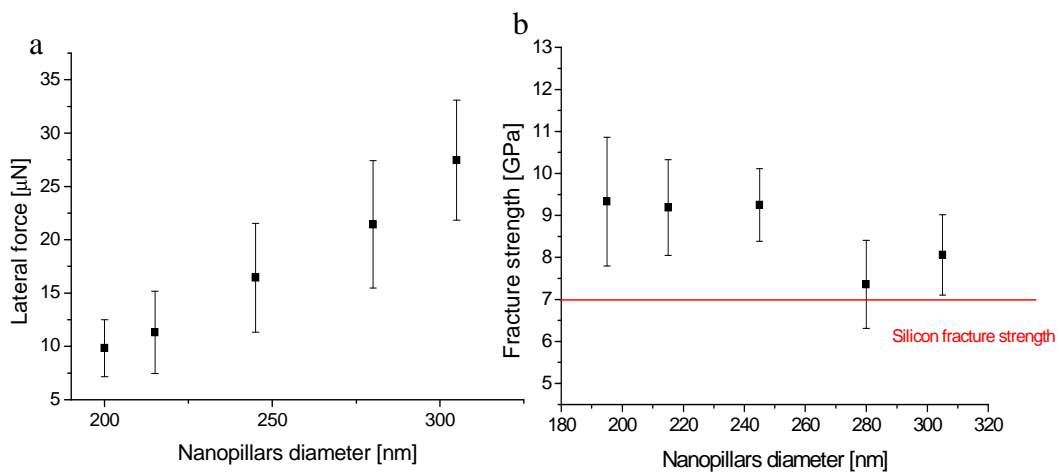
Figure 4.32 *Fracture force and corresponding maximal principle stress determined from nanopillars fracture experiments. The red line in plot (b) corresponds to the macroscale silicon fracture strength.*

4.5.2. Inaccuracies in nanopillar shape

According to the SEM images and SFM micrographs, nanopillars are usually perfectly cylindrical. However, in order to find out if small, not observable differences in geometry due to i.e. etching anisotropy may influence the results of fracture strength determination, the measurements with different angular position of the sample were

conducted. In this case Si/SiO$_2$ nanopillars were used. Two micrographs with different angles are shown in **Fig.4.33**. Fortunately, the differences between the forces, which induce fracturing, are smaller than the measurement error. Nevertheless, the experiment revealed another interesting effect. The larger distances between nanopillars can influence the behaviour of the feedback, which results in different lateral forces for the same normal load. It was not an accident that in **Fig. 4.33b** there is more fractured nanopillars than in **Fig. 4.33a**. The integral component of the feedback control is responsible for the slower reaction and, bigger lateral forces as a result, in case of larger distances between nanopillars. It is another reason, next to the changes of the friction coefficient in different environments, for direct measuring of lateral force instead of normal load.
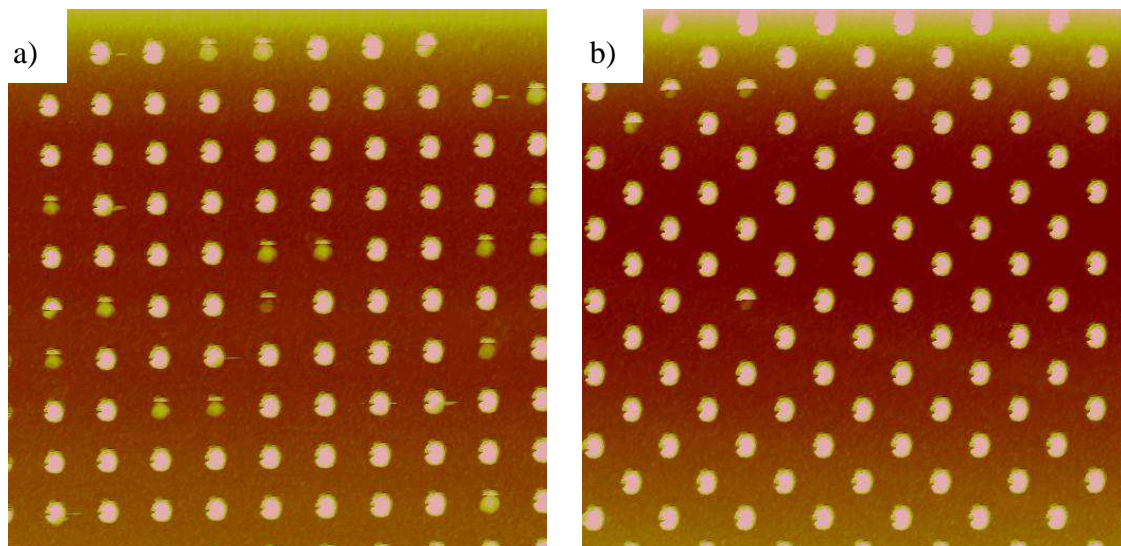

Figure 4.33 *Two SFM micrographs shown scanning with two different angles – (a) with 0° and (b) with 45° - and the same normal load.*

4.5.3. Inaccuracies in FEM simulations

The assumed geometry is very important for precise evaluation of fracture strength of measured pillars from FEM analysis. The most crucial parameter is the radius of curvature of the corner between a pillar and the substrate, which may strongly influence the estimated values of fracture strength. In first simulations it varied between 3 and 10 nm, which is a reasonable value for RIE process by which nanopillars were fabricated. Fortunately, the results gained with the smallest and the biggest radius differ from each other by 7% in case of stress at the base of pillars and less than 1% in case of

pillars with the interface (which position was assumed to be 50 nm above the ground). These results were not mesh sensitive for a reasonable number of elements.

4.5.4. Tip-pillar interactions in tapping mode

There are several models of the interactions between SFM tip and the sample surface in tapping mode [65-66]. Therefore, the question arises, what influence on the measured values has the chosen model. The model used in this thesis is based on the energy conservation principle and it also distinguishes the energy which is lost due to the ambient environment (dumping in air) and the energy dissipated by the tip-surface interactions. Hence, the assumption, which may introduce the biggest error is the assumption that all this energy is dissipated due to the viscous properties of polymer nanopillar. Certainly, there are some other dissipation mechanisms such as friction, which influence on dissipated energy is difficult to estimate due to difficulties in exact friction coefficient determination or in estimating the friction path. However, by adjusting the amplitude and the setpoint of the oscillations it is possible to minimize the energy dissipated by phenomena not described by the model.

On the other hand, the method of viscosity measurement described in §4.3.3 is based on an analogy to the macroscopic DMA (dynamic mechanical analysis) experiments. Hence, the sinusoidal stress should be constantly applied to a nanopillar, which means that the SFM tip is constantly in the contact with the pillar. The adhesive force between the top of the nanopillar and the tip plays in the case of the unloading phase an important role. This force must be stronger than the force which appears while stretching the nanopillar. To make it possible the oscillation amplitude should be small and the setpoint big, which, however, increases the friction influence. Thus, a precise adjustment of the scan parameters must be conducted before every experiment, in order to get proper results. Another option is to develop a more sophisticated model which will include at least friction.

74

5.   Results and discussion

This chapter proves that the method described above is able to investigate not only brittle materials such as silicon, but also ductile and viscoelastic materials (i.e. PMMA) and interfaces. Some interesting phenomena, which were observed while testing this method, are also described and explained here in details.

5.1.   Fracture strength of silicon and size effect

As it is shown in **Fig.4.32** the size effect for the fracture strength of silicon nanopillars was not observed. The brittle fracture of silicon is affected by defect (crack) population and residual stresses. In this case there should not be any residual stresses so the size effect can occur only due to different defect population. Nanopillars were made of silicon p-doped single crystal, in which defects dimensions are of nanometer size. Hence, their distribution in single nanopillar should be consistent with defect distribution in bulk material.

It should be noted that there are many experiments in which silicon fracture strength was measured for structures of a micrometer size [67]. Unfortunately, the measured values range from even less than 1 GPa to 10 GPa. It is due to the fact that fracture strength of silicon depends strongly on defect size, loading mode, specimen size, orientation and the test method. The microfabrication methods can also strongly affect the structure of a silicon sample. Fortunately, in our case the process of manufacturing the silicon nanopillars should not influence significantly the silicon crystal structure so it is reasonable to compare our results with the bulk silicon fracture strength.

5.2.   Si/SiO$_2$ nanopillars

5.2.1. Experiments performed at ambient conditions

The results of the fracture strength measurements for the second experimentally probed system, the Si/SiO$_2$ nanopillars which contain an interface are plotted in **Fig.5.1**. Notably the fracture initiation always occurs at threshold stresses of about 3 GPa, which is significantly lower than observed for similar diameter bulk silicon nanopillars.

Furthermore the breakage always occurred at the interface and not, as observed with crystalline Si pillars, at the pillar base (**Fig.5.2**). The quantitatively determined values are consistent with the results obtained from macroscopic investigations of that interface gained by Ando et al.[68] and have been indicated in **Fig. 5.1d** by the orange line. These results provide evidence that reliable quantitative assessments can be obtained by the here introduced method for material amounts far smaller than those probed in conventional measurement methods. Also our method is fast and allows investigation of hundreds of nanopillars within minutes to reveal the quantitative force thresholds to induce fracture and the ultimate stresses.
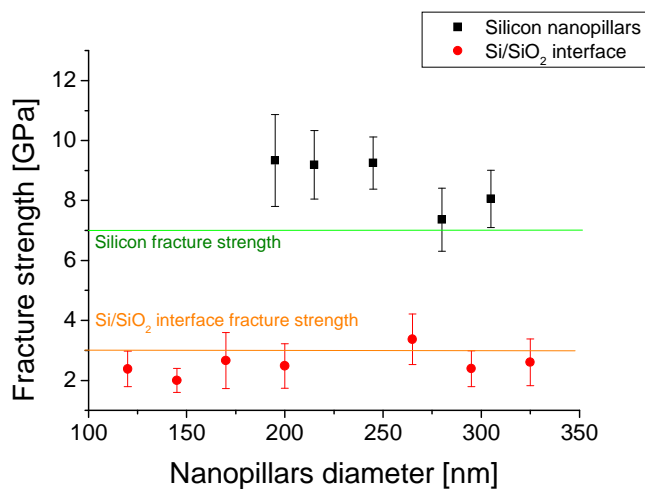

Figure 5.1 Results of measurement on nanopillars with different diameters are shown here for both silicon and Si/SiO$_2$ nanopillars. As expected fracture strength is constant and smaller for Si/SiO$_2$ pillars, which breaks exclusively at the interface.
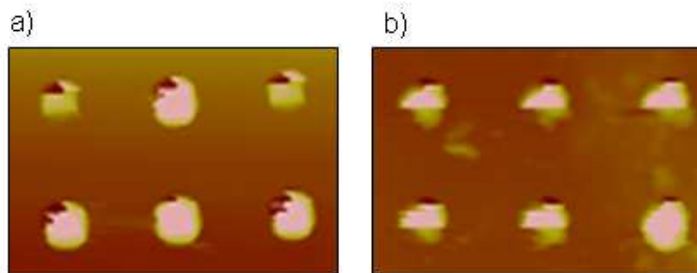

Figure 5.2 Si/SiO$_2$ nanopillars broken at the interface.

a) pillars broken instantly

b) pillars broken after a few scans.

5.2.2. Experiments performed in water

Probing materials properties with small dimensions of samples in the range of few nanometers also provides important opportunities in a different context of materials science. Many processes affecting material strength occur very slowly, e.g. via diffusion processes. This motivates studies of fracture thresholds in a modified liquid environment and as a first choice we have selected water instead of air. It was not a random choice. It is well-known that water is able to reduce the fracture strength of silicon oxide-based glasses and also may influence the structure of the Si/SiO_2 interface [69-71].

As it was expected, a significant time dependence of the fracture thresholds has been observed for nanopillars of different sizes (between 100 and 200 nm in diameter). The **Fig.5.3** plots the time dependence of the fracture thresholds, measured for 170 nm diameter nanopillars, in hours after exposure in high purity (deionized) water. From our SFM imaging experiments it is clear that these pillars also break at the Si/SiO_2 interface irrespective of the duration of water exposure. With prolonged water exposure the interface becomes distinctly weaker and the modified fracture threshold levels off after about five hours. In this state, where no further modification of the fracture strength is apparent, pillars are about 20% weaker.
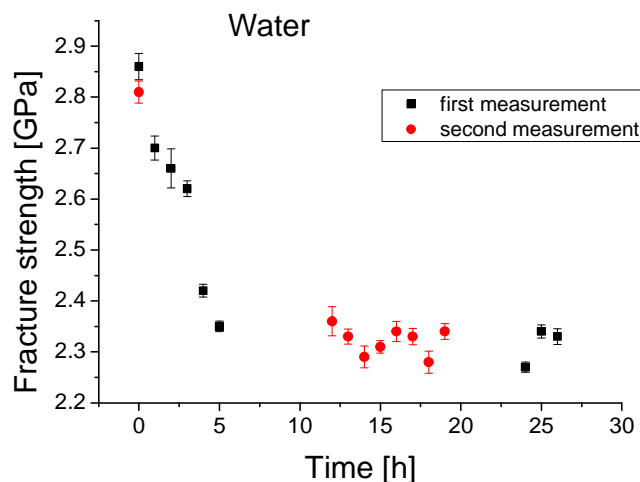

Figure 5.3 *Influence of water on Si/SiO_2 interface. After about 5 hours an equilibrium state is achieved and nanopillars are about 20% weaker than at the beginning. Two different measurements (first and second) were done to confirm the behaviour of the interface in water.*

5.2.3. Experiments performed in salt solutions

The experiments in salt solutions were the next step in the investigation of the corrosion of the Si/SiO_2 interface. There are two motivations for taking this direction. Firstly, the measurements can be useful in developing the Li-ion batteries. Conventional Si anodes in such batteries, typically suffer from rapid capacity decay due to mechanical fracture caused by large volume expansion during the Li-Si reaction [72]. Secondly, the influence of salt solutions (corrosive environment for metals) on the strength of the Si/SiO_2 interface, due to some unexplained phenomena, which occur here, was interesting from the pure scientific point of view.

During the experiments three different salt solutions in water were used: sodium chloride, lithium chloride and caesium chloride. The concentration of the solutions ranged from 0.1 to 1000 µmol/l and the measurements were conducted at room temperature. The cantilever was firstly immersed in the solution for more than 10 hours in order to equilibrate its surface and the solution. This step in experimental procedure was necessary because it was observed that water or solutions can strongly influence the surface energy of cantilever's tip and, as a result, the friction coefficient. Such an evolution of friction coefficient in time does not influence the results (the lateral force is measured) nevertheless the changes are so significant that after few hours it is impossible to fracture thicker nanopillars even when the highest possible normal force is applied - friction coefficient strongly decreases and lateral force (which depends linearly on the friction coefficient) is too weak to fracture nanopillars.

After the cantilever had been equilibrated, the samples were also immersed in liquid and the measurements of the fracture strength of the nanopillars started. In this case the procedure was the same as for the measurements in air. To estimate the averaged fracture force (§ 4.2.3) four different measurements with four different normal forces were conducted hourly. It took usually about 25 minutes for the 10x10µm scan field so to investigate rapid processes (higher concentration) scan field was smaller (5x5µm). The measurements were conducted usually for the first 8 hours of immersion and then in the equilibrium state (after 24 hours) usually for 4 hours. As it will be shown further in this paragraph, the influence of ions is reversible. Due to this effect one sample could have been used to perform more than one experiment. Some measurements were repeated to fill in the gap between the first and the second part of

the experiment and also to check if the results are repetitive. The measurements were done at room temperature.

The results of the measurements of fracture strength of Si/SiO$_2$ nanopillars in salt solutions are shown in **Fig. 5.4**. It can be clearly seen in every case that the fracture strength of the interface is much higher after a few hours of the immersion. Without an exception, after 5 hours it was higher than fracture strength estimated in air. The strengthening was faster and more significant for solutions with higher concentration. In **Fig. 5.5** it is also shown that the caesium chloride solution has the strongest influence on the fracture strength of the interface, whereas the lithium chloride has the weakest one. It can therefore be assumed that the ions, contained in the solutions, can diffuse into the Si/SiO$_2$ interface and make it stronger.
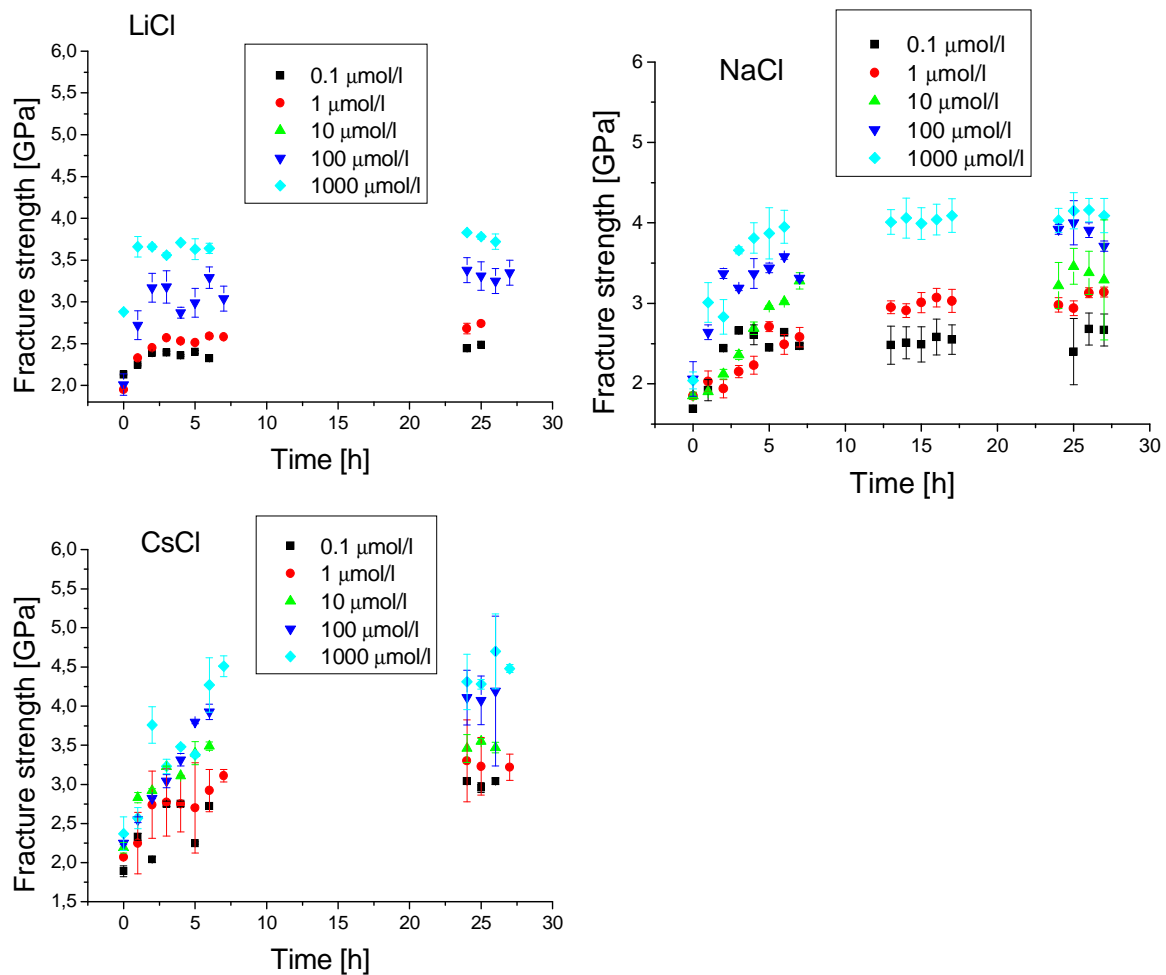

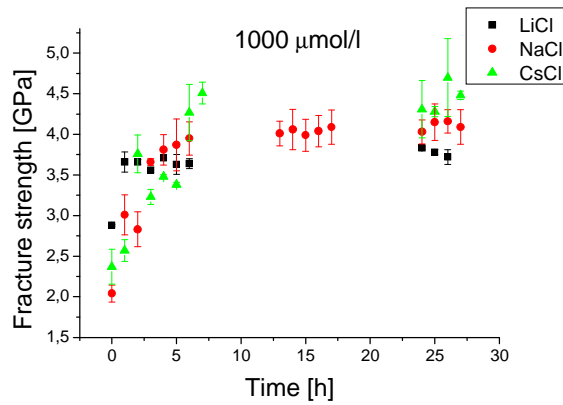***Figure* 5.4** *Influence of salt (LiCl, NaCl, CsCl) solutions on Si/SiO$_2$ interface at various concentrations.*

Figure 5.5 *Comparison of influence of salt solutions (LiCl, NaCl, CsCl) at 1000 µmol/l concentration.*

Another interesting effect was observed when the samples, firstly influenced by the solutions, were dried in air. After 24 hours the fracture strength was determined again and it was practically unchanged (**Fig.5.6**). This indicates, that the ions, which diffused into the interface, can permanently rise its fracture strength. Nevertheless, it was observed that fracture strength of pillars, which were again put into water after 72 hours drastically decreases to the level before the immersion in the salt solutions. It is evident that water can swill out the ions from the interface but it cannot influence on the interface permanently. The samples dried in air regained, surprisingly, its fracture strength from the beginning of the experiment. It is apparent, therefore, that the influence of different liquids on the measured interface can be reversed.
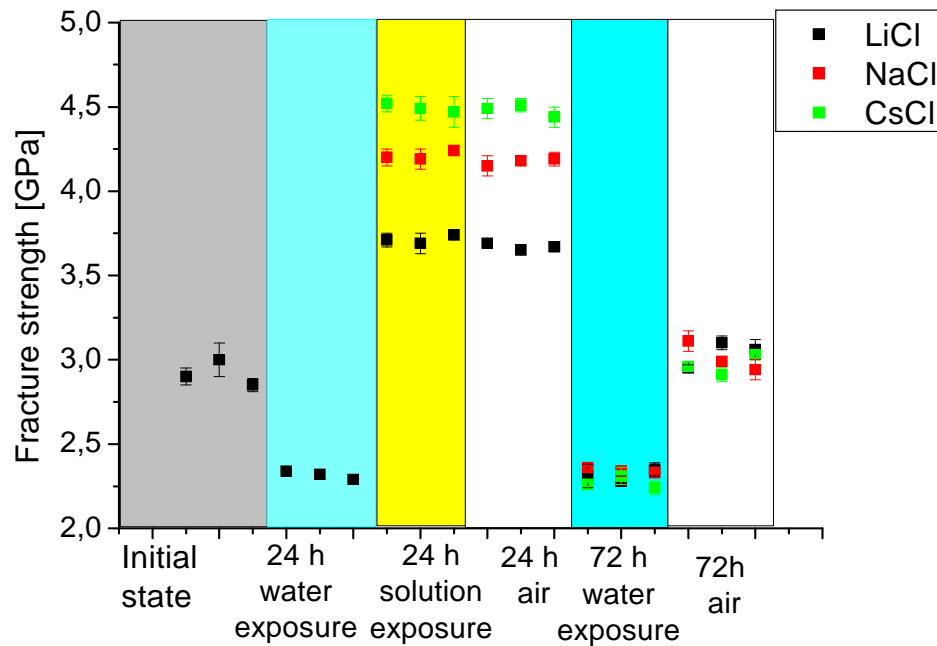
Figure5.6 *Reversibility of strengthening/ weakening processes. After 24 hours after the solution exposure the fracture strength was practically unchanged. This indicates, that the ions, which diffused into the interface, can permanently rise its fracture strength. Nevertheless, it was observed that fracture strength of pillars, which were again put into water after 72 hours drastically decreases to the level before the immersion in the salt solutions.*

To determine whether cations or anions, or maybe both are responsible for the observed strengthening effect, one more experiment was done. Two samples were firstly put into water for 24 hours and then for next 24 hours into the 1mmol/l HCl and NaOH solutions. After that procedure, the fracture strength of the nanopillars was studied. As it is shown in **Fig.5.7** fracture strength of nanopillars exposed to hydrochloric acid is slightly larger whereas nanopillars exposed to sodium hydroxide are much stronger (almost as strong as these exposed to 1 mmol/l sodium chloride solution).

Figure 5.7 *Comparison between different salt solutions. Fracture strength of nanopillars exposed to hydrochloric acid is slightly larger whereas nanopillars exposed to sodium hydroxide are much stronger (almost as strong as these exposed to 1 mmol/l sodium chloride solution).*
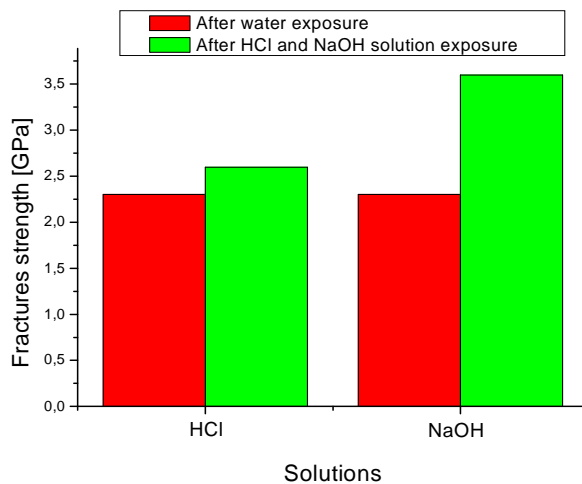
In parallel to the fracture strength measurement also friction coefficient between the diamond SFM tip and silicon surface, on which nanopillars had been made, were examined. The results (**Fig. 5.8**) indicates that the used salt solutions strongly decrease the estimated friction coefficient. In contrary to the results of fracture strength examination, the concentration of the solution has no influence on the value of the friction coefficient in the equilibrated state. However, as anticipated, the rapidity of the process depends on the concentration of the ions. Without exception for 1000 µmol/l the equilibrium state is approached within one hour whereas for lower concentrations it takes much longer.

In order to evaluate the changes in the acid and base compounds of the free surface energy of the silicon and silicon dioxide used to prepare the nanopillars, the contact angle measurements were conducted. Three different liquids were used: water, diiodomethane and glycerol. The results are shown in **Tab. 5.1**.
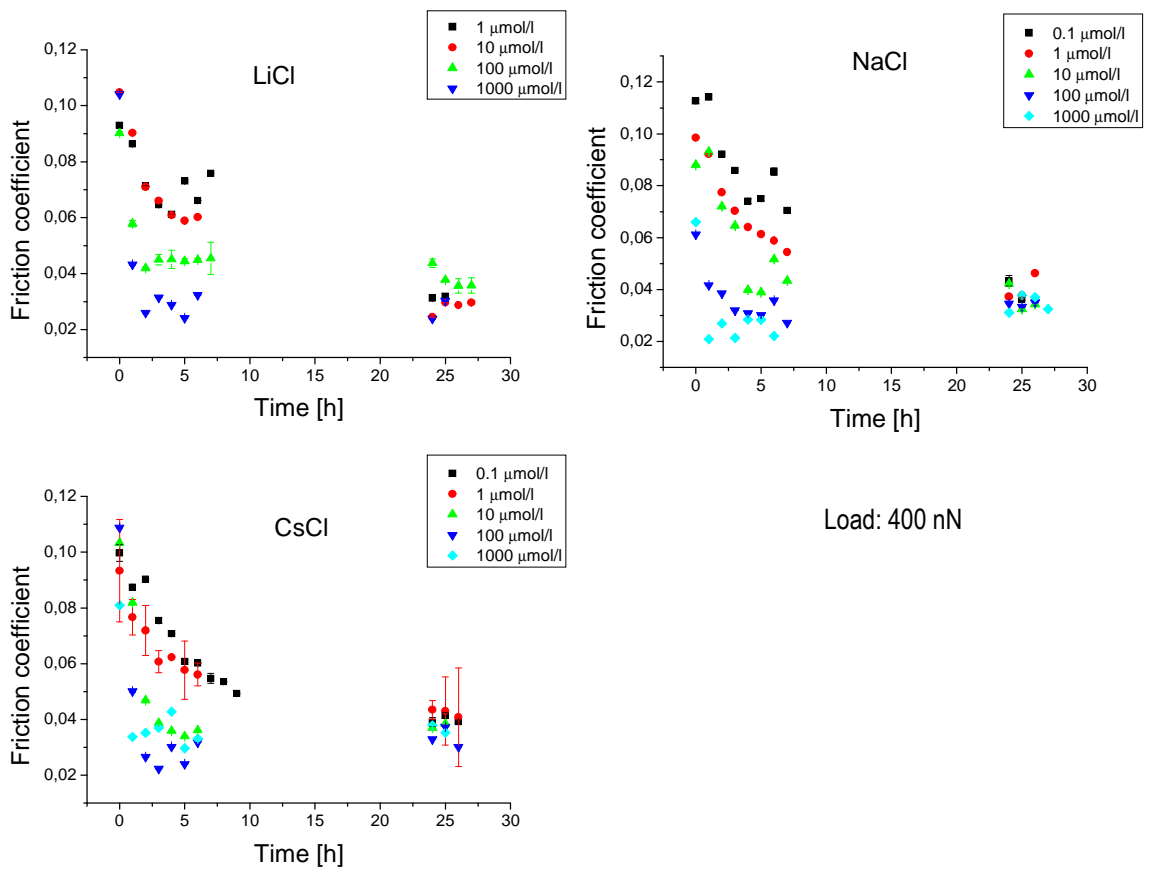
Figure 5.8 *Friction coefficient evolution in different salt solutions.*

Studied surface	γ_s^d	γ_s^+	γ_s^-	γ_s^{AB}	γ_s	$\sigma_{\gamma s}$
Silicon	40.1	3.0	32.1	19.6	59.7	0.8
Silicon after water exposure	41.2	3.1	30.2	19.4	60.6	0.9
Silicon after LiCl solution exposure	40.2	4.5	45.1	28.4	68.6	0.7
Silicon after NaCl solution exposure	40.4	4.6	49.3	30.0	70.4	0.6
Silicon after CsCl solution exposure	41.1	4.7	53.8	31.8	72.9	0.8
SiO_2	31.7	0.8	53.6	12.9	44.6	0.7
SiO_2 after water exposure	31.3	0.7	48.7	11.8	43.1	0.9
SiO_2 after LiCl solution exposure	31.5	0.8	59.1	13.7	45.2	0.8
SiO_2 after NaCl solution exposure	31.8	1.5	62.8	19.5	51.3	0.6
SiO_2 after CsCl solution exposure	31.7	1.9	69.1	22.9	54.6	0.8

Table 5.1 *Components of the surface energy [mJ/m^2] of silicon and silicon dioxide after interaction with different chemical environments. $\sigma_{\gamma s}$ stands for the standard deviation of γ_s.*

5.3. Influence of water and ions on fracture the fracture strength of Si/SiO$_2$ interface

5.3.1. Weakening in water

On the basis of fundamental physico-chemical considerations the interaction of a nanopillar surface with polar fluids like water occurs through the interaction of the topmost layer with water molecules which modifies the surface energy and possibly initiates degradation by swelling. Chemically silicon oxide is partially converted into anhydride which is persistent on the surface, while depending on environmental conditions the depth of the anhydride layer varies. There is considerable evidence from our experiments, that swelling/degradation is not the predominant effect leading to the significant decrease in the fracture strength upon the water exposure. This occurs firstly

from the levelling off of the measured values decrease after ~5h and secondly from the recovery of the initial 'dry' strength of the water-exposed nanopillars within some days after water removal and, finally from the very low solubility of silicon dioxide (0.12 g/L). Notably Si as a covalent crystal is insoluble in water, as well as the diamond coated tip.

Therefore, it can be assumed ,that the main reason for weakening of the Si/SiO$_2$ interface in water is the diffusion of water molecules along the interface into the pillar structure. As described in §5.1.1 the silicon dioxide layer was produced in a LPCVD process. The stress in the deposited layer should not be higher than 300 MPa and the interface should be uniform, without many defects and due to the process no moisture (H2O) contamination is expected. Hence, the fracture strength of this interface can be strongly affected by the diffusion of water molecules.

Under the assumption that the fracture strength reduction of the interface varies linearly with the amount of trapped water, which has diffused into it and that the equilibrium of the system means that no more water can diffuse into the interface, it is possible to evaluate the diffusion coefficient from fitting **Eq.(A2.7)** (in Appendix 3) to the experimental data. The detailed description of the diffusion theory can be found in Appendix 3. **Fig. 5.9** plots the reduction of the fracture strength of the investigated interface vs. the exposure time to water and a fitting curve.
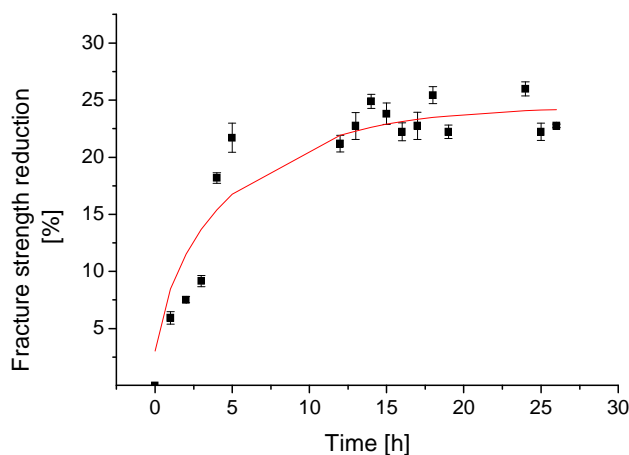

Figure 5.9 *Plot showing reduction of the fracture strength of the investigated Si/SiO$_2$ interface vs the exposure time to water and a curve fit taking into account the expected diffusion along a 2D interface.*

The correlation coefficient determined in the fitting is R^2 = 0.89. Hence, the assumption that the adhesion degradation process follows the Fick's law is correct. The water diffusion coefficient determined from the curve fit equals $(2.2\pm0.5)\cdot10^{-15}$ cm^2/s.

For comparison, this value is almost two orders of magnitude larger than for diffusion along silica glass ($7 \cdot 10^{-17} cm^2/s$) and five orders of magnitude larger than along quartz ($4.5 \cdot 10^{-20} cm^2/s$) [73]. From the magnitude of this experimentally determined diffusion coefficient it is evident then, that the diffusion responsible for the decrease of the fractures strength occurs mainly along the Si/SiO_2 interface.

The degradation of adhesion between other materials, as an effect of water diffusion, has also been reported for pairs of other materials i.e. TiN and SiO_2 [74], silicon – organosilicate glass (OSG) [75] and some others [76, 77]. The weakening of the interfaces is due to the ability of water to decrease the work needed for the opening the crack. If SiO_2 is locally converted to SiOH (the anhydride) only little interfacial cohesion remains. Especially interesting, for our case, are results described by Vlassak et al. for OSG film stack [74] due to similarities in the atomic structure between amorphous silicon dioxide and the ogranosilicate glasses[2] [77-79]. In their work, they proved that the water diffusion along the OSG/Si interface can strongly decrease adhesion between this two materials. The diffusion coefficient, which they measured, is $2.4 \cdot 10^{-15} cm^2/s$, which is consisted with the value for Si/SiO_2 interface measured in this Thesis. Furthermore, Vlassak et al. provided another evidence that in case of their samples, the water certainly diffuses along the interface. In order to determine the path of water diffusion they carried out the experiments with deuterium as an isotopic tracer. They exposed the silicon substrates with OSG films to heavy water (D_2O) at room temperature and they ensured that the diffusion can take place only at the edges of the samples. Using secondary ion mass spectroscopy (SIMS) they measured the concentration of heavy water along the interface.

The exact mechanism of the weakening of the Si/SiO_2 interface due to water diffusion has not yet been fully understood. On the other hand, the diffusion of water through the amorphous silicon dioxide is well-known and explained. In this case water diffuses in molecular form and reacts with the silicon-oxygen network to form SiOH groups [79]:

---

[2] Organosilicate glass (OSG) is a hybrid organic-inorganic material that consists of a siloxane network similar to that of amorphous silicon dioxide where some of the bridging oxygen atoms have been replaced by hydrogen (-H) or hydroxyl groups (-OH) and by organic groups such as methyl (-CH_3) or methylene (-CH_2-)

$$\text{Si-O-Si} + \text{H}_2\text{O} \leftrightarrows \text{2SiOH} \qquad \textbf{(Eq. 5.1)}$$

At low temperature the reaction is slow and the water molecules are not necessarily in equilibrium with the hydroxyl groups. Although, the process of diffusion of water into silicon dioxide does not explain the phenomenon of adhesion degradation in the experiments described in this thesis, it is highly possible that there are some similarities between this type of diffusion and observed here, diffusion into interface. Water, while diffusing into the Si/SiO_2 interface, may react with silicon dioxide according to **Eq.5.1** and as a result it breaks the bonds between Si and SiO_2. Furthermore, the amorphous silicon dioxide is grown on a pure silicon crystal and the lattice mismatch between those two materials is rather large, but the highly flexible angle of the Si-O-Si bond can compensate for a major part of this mismatch. The remaining silicon atoms with incomplete coordination form the prevalent imperfection of the interface – the silicon dangling bonds, which may strengthen and accelerate the hydration of the silicon dioxide in the analyzed interface. Nevertheless, this reaction is reversible, therefore it is possible that after some time (for the nanopillars with the diameter of 170 nm after 5 hours according to our results) some kind of equilibrium is reached.
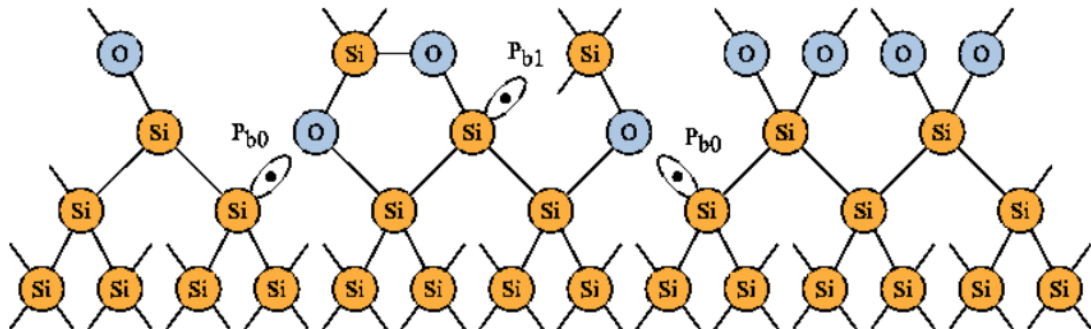

Figure 5.10 *Structure of silicon (100) and silicon dioxide interface. P_{b0} and P_{b1} are two different types of dangling bonds, which may occur in this configuration. The P_{b0} center is back-bonded to three silicon atoms and the P_{b1} is back-bonded to two silicon atoms and one oxygen atom. Both of this defects are chemically active and may strengthen the process of the hydration of the silicon dioxide.*

5.3.2. Strengthening in salt solutions

The strengthening of the Si/SiO$_2$ interface in salt solutions (**Fig.5.4**) can also be explained by the diffusion of certain ions into this interface. In our experiments three different salts were used: lithium chloride, sodium chloride and caesium chloride. Therefore, there were chloride anions in each solution and different cations. As shown in **Fig. 5.5** the strengthening depends on the type of the used salt. Furthermore, according to the results of the experiment with hydrochloric acid and sodium hydroxide (**Fig.5.7**) HCl has much weaker effect on the fracture strength of the measured interface than NaOH. In NaOH solution there are no chloride ions but the interface was almost as strong as after exposure to sodium chloride solution of the same concentration. Hence, the most probable explanation for the increase of fracture strength of Si/SiO$_2$ interface is diffusion of cations. As the strengthening is also observed for HCl we may conclude that also hydronium cations diffuse into the interface and modify the Si dangling bonds.. Hydroxyl ions present in NaOH solution may be responsible for a small difference in fracture strength of nanopillars immersed in sodium hydroxide and sodium chloride solutions.

The evaluated diffusion coefficients of used cations in the Si/SiO$_2$ interface for different concentrations are shown in **Tab. 5.2**. They are not concentration dependent, at least in the range of used concentrations. For lithium ions we measure the highest diffusion rate, in consistency with published diffusion rates whereas caesium ions are least diffusive due their large ionic radius. Lithium is the smallest ion – its radius is 90 pm, sodium – 116 pm and the biggest caesium ion – 181 pm.

Cation	Concentration [µmol/l]	Diffusion coefficient [cm^2/s]
Li+	0.1	1.4±0.5
Li+	1	1.4±0.6
Li+	10	1.4±0.3
Li+	100	1.5±0.6
Li+	1000	1.6±0.9
Na+	0.1	1.0±0.4
Na+	1	1.0±0.4
Na+	10	0.9±0.2
Na+	100	1.2±0.2
Na+	1000	1.3±0.4
Cs+	0.1	0.6±0.5
Cs+	1	0.6±0.3
Cs+	10	0.6±0.3
Cs+	100	0.7±0.3
Cs+	1000	0.7±0.3

Table 5.2 Evaluated diffusion coefficients of different ions. It is evident that the coefficient depends on the type of ions and slightly on concentration (at least in the investigated concentration range). The fastest diffusion occurs for the lithium ions due to their small dimensions.

The mechanism of strengthening of the Si/SiO$_2$ interface in the different salt solutions can be explained by two different effects. Firstly, ions may take the place of water in the interface, therefore, reduce the internal stress, which is caused by it. It is well-known that especially silicon dangling bonds react easily with hydrogen ions. Even stronger effect occurs for ions present in salt solutions used here. Secondly, the acid-base adhesion theory described in §2.1.4 can explain the strengthening of the interface above its initial fracture strength. The results of the free surface energy components, showed in **Tab.5.1**, can confirm this assumption. Water has not changed significantly the value of the free surface energy. The dispersive part of it has been also barely changed by salt solutions. However, the acid-base part (nondispersive) has been changed significantly. Especially, the acidic component of silicon dioxide surface energy is changed by the salt solutions. These changes influence strongly the adhesion between the silicon and silicon dioxide and therefore increase the fracture strength of this interface. The largest increase of acidic part of both silicon and silicon dioxide free surface energy has been observed after exposure to caesium chloride solution. It is

consistent with the fracture strength measurements, in which this solution has given the largest increase of fracture strength. It is quite surprising result because cesium ions are not as strong Lewis acids as i.e. hydrogen ions. This effect can be explained, however, when the ions radiuses are compared. The caesium ions are the larges ions used in this experiments. Hence, their diffusion inside the silicon dioxide is considerably retarded and they stay on the SiO_2 surface or in SiO_2/Si interface, whereas smaller ions (hydrogen or lithium) can easily diffuse deeper into SiO_2, which may reduce their influence on the surface or interface properties. The acidic part of the silicon surface energy were also alerted by the salt solutions but in this case, the changes were much smaller and in the same range for each salt. It means that ions does not react as easily with silicon surface and diffusivities of ions in silicon crystal are similar.

Another effect, which was observed while fracture strength measurements, was the strong reduction of the friction coefficient between diamond SFM tip and the silicon surface. Further investigations revealed that the same effect is observed for silicon dioxide surface (**Fig. 5.11**). Therefore, an extremely important advantage of direct lateral force measurement is revealed. If constant friction coefficient is assumed and only normal load is taken into consideration then it is impossible to distinguish the weakening/strengthening of pillars and observe the friction coefficient changes.
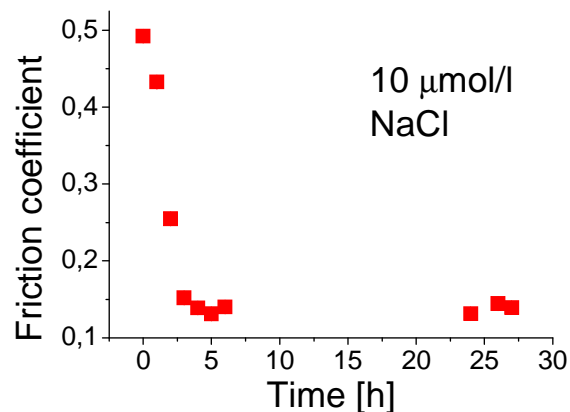

Figure 5.11 *Evolution of friction coefficient in time for diamond SFM tip and a silicon dioxide surface immersed in 10 µmol/l sodium chloride solution.*

The friction coefficient measurements also provide one more proof that the diffusion of ions is responsible for the observed changes in the fracture strength. In **Fig. 5.12** there are two different plots shown – evolution in time of fracture strength of Si/SiO_2 interface in 1000 µmol/l caesium chloride solution and evolution in time of friction coefficient between the SFM diamond tip and silicon surface in the same

solution. To the friction coefficient points simple exponential decrease function is fitted and the time constant is evaluated (time after the friction coefficient is smaller *e* times, *e* – Euler constant). To the fracture strength points the **Eq.A2.7** is fitted and also time constant is determined. Both time constants are different: for strengthening of the interface it is 2.5±0.4 h whereas for the friction coefficient decrease it is much shorter: 0.5±0.3 h. Hence, these two effects are different in nature. The friction coefficient is changed due to ions reacting with the surface and the fracture strength increased as a result of ions diffusing into the interface and complex processes occurring there.
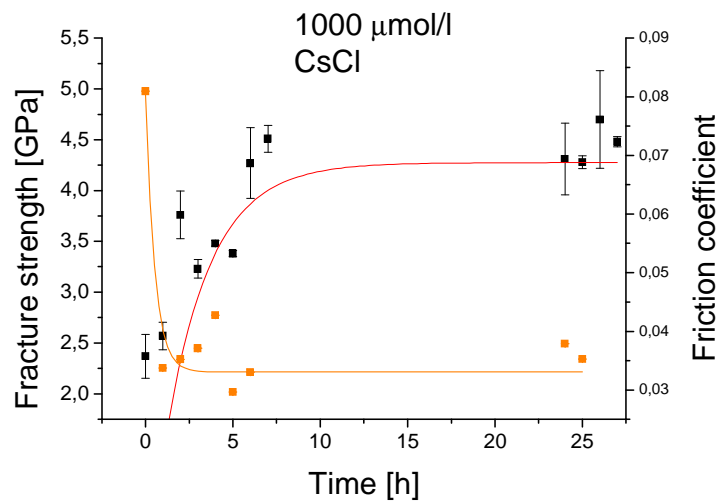
Figure 5.12 *Fracture strength and friction coefficient for Si/SiO$_2$ interface vs immersion in the 1000 µmol/l CsCl solution time. Time constants were estimated as follows:*
Strengthening: 2.5±0.4 h
Friction coefficient reduction: 0.5±0.3 h

The problem of the ionic interaction with Si/SiO$_2$ interfaces and silicon or silicon dioxide or similar surfaces was not studied in details in the literature. Nevertheless, some interesting reports can be found. In [81] it is shown that the ionic strength has a strong influence on the corrosion of glass fibers. On the other hand in [82] it is described the process of reduction alkali metals chemically by the Si/SiO$_2$ interface, whereby positive charges are transmitted to the interface region. Results consistent with our observation are shown in [83] where accumulation of alkali metal ions at the interface is proofed. This effect is explainable by the low interface packing density. As a result, the diffusion rate at the interface is increased which may explain the ion accumulation at that position. A very interesting effect is studied in [84]. Photoemission

and thermionic emission are used to determine the dipole polarization layer produced by sodium ions at a Si/SiO$_2$ interface. The electronic energy barrier at the interface is reduced by the sodium ion dipole from 4.25 eV for a clean Si/SiO$_2$ interface to a saturation limit of 2.6 eV for a sodium coverage of 1.3×10^{15} Na∕cm^2. Such an effect, in consistence with the acid-base theory and our results, certainly leads to strengthening of the interface.

The results and theories described in this thesis may be useful to explain some problems and difficulties which have arised in Kaufmann's Thesis [40] (he also worked with nanopillars as it was described in §2.3.4). Firstly, as it is shown in **Fig. 5.13**, he identified two different processes, which take place when pillars are immersed in sodium chloride solution in water: weakening of the pillars at the beginning of the experiment and strengthening of the pillars after about 5 hours. These effects can be easily explained; Kaufmann measured only normal force and he did not equilibrate the tip surface. Hence, the friction coefficient changes are responsible for the apparent "weakening" of nanopillars. In **Fig.5.14** the evolution of the friction coefficient is shown without previous equilibration of the tip. At the beginning the friction coefficient significantly increases for each concentration of sodium chloride solution. Therefore, while the normal load was kept constant, the lateral force was increasing. After a few hours, the friction coefficient decreases and reaches its equilibrium which is consistent with the previous experiments. The strengthening of nanopillars observed by Kaufmann, according to findings of this thesis, is not only strengthening of nanopillars but also reduction of friction coefficient.

Furthermore, Kaufmann hypothesis about the strengthening of nanopillars in sodium chloride solution due to the diffusion of ions into the interface has been confirmed in this Thesis which provides more conclusive data and thereby allowed for deeper insight into the competing mechanisms affecting the experimental outcome.
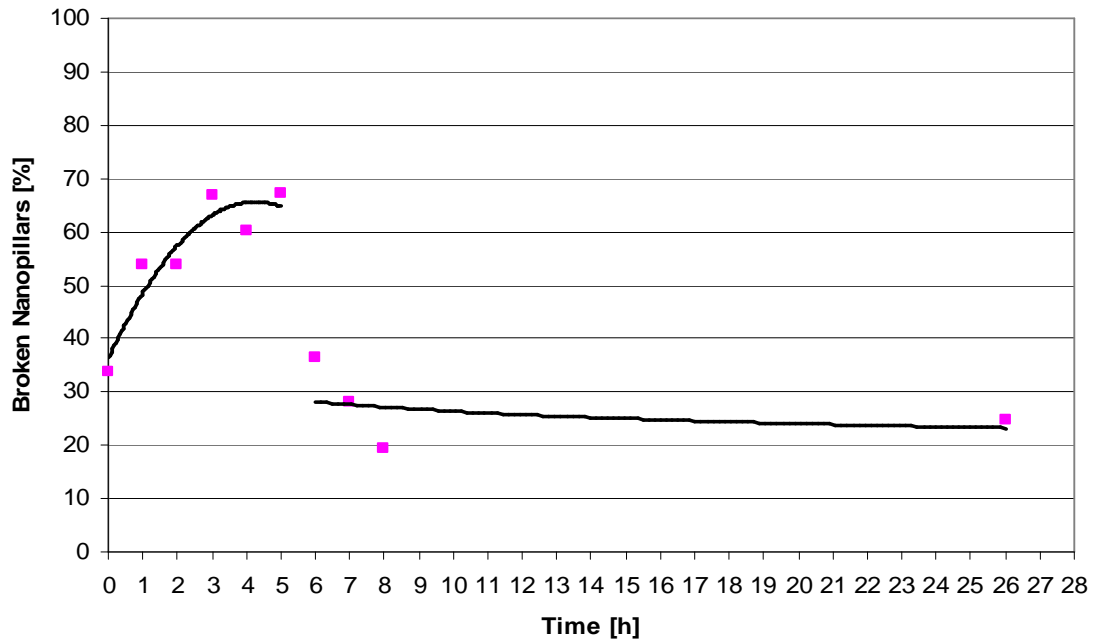
Figure 5.13 *Results of fracture experiment with Si/SiO$_2$ nanopillars in sodium chloride solution gained by A. Kaufman. (source: [40])*
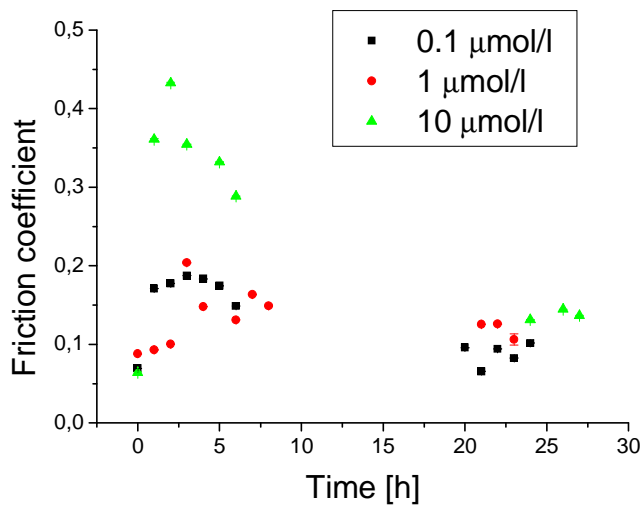

Figure 5.14 *Evolution of friction coefficient in time for diamond SFM tip and a silicon dioxide surface immersed in three different solutions of sodium chloride. The cantilever tip was not equilibrated in the solution before the measurements as it was done in previous experiments described in this thesis.*

5.4. Mechanical properties of PMMA as a function of temperature

5.4.1. Elastic modulus and flexural strength

To determine the Young modulus of PMMA, two different approaches were used. The first method was by measurement of the bending of the nanopillars as described earlier in this thesis. The second approach is commonly used method – the indentation of the SFM tip into the PMMA surface (detailed description is presented in Appendix 3) and it was used as a reference method.

In **Fig.5.15** there is plotted a typical relationship between the applied force and the deflection of PMMA nanopillars. To determine the Young modulus the linear fit was evaluated for the linear part of the curve and then the modulus was calculated according to the **Eq. 4.19**. It should be noted that the Young modulus in this case is assumed to be constant in time. It is a reasonable assumption while the time here is short and the viscosity of PMMA below the glass transaction temperature is very high. From the curve showed in **Fig. 5.15** it is also possible to determine the flexural strength of the PMMA. In order to do that, the value of force above which the nonlinearity in relation between force and pillar's deflection appears must be evaluated. The next step is to determine the stress field in nanopillars, which is loaded with this force and determine the highest von Mises stress (polymers are ductile materials so von Mises yield criterion is the most suitable in their case). Analogically to the silicon nanopillars fracture strength determination, to evaluate the flexural strength, FEM simulations are used.

The results of Young modulus measurement with two different methods (by bending and by indentation) are shown in **Fig.5.16**. Both methods give consistent results so it confirms that, the bending test method, which has been established in this thesis, is able to appropriately measure the Young modulus of soft and ductile materials. The data reveals that the Young modulus decreases with increasing temperature which is typical for the PMMA. Much stronger reduction may be observed below the glass transaction temperature. Unfortunately it was not possible to achieve temperatures higher than 100°C with the experimental setup used in this experiment, so no further experiments about glass transition temperatures have been performed yet.
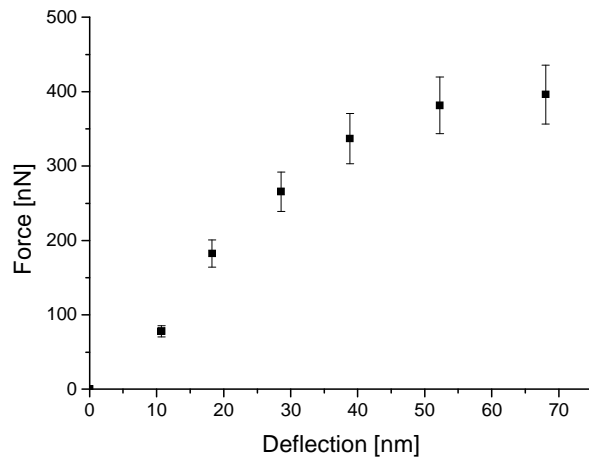
Figure 5.15 Typical relationship between applied force and the deflection of a PMMA nanopillar.
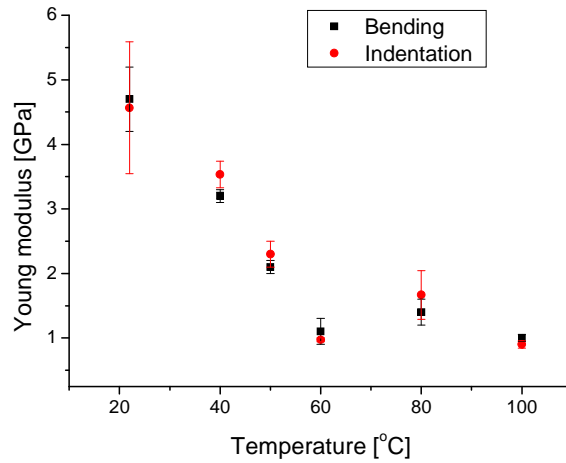

Figure 5.16 Results of investigation of Young modulus with use of two different techniques: nanopillars bending and PMMA surface indentation.

A significant advantage of the bending test method is the ability to determine the flexural strength of the investigated material. The results of flexural strength measurement are shown in **Fig.5.17**. The plot reveals that the dependence of flexural strength of PMMA on temperature is much weaker than the corresponding dependence of the Young modulus. The values of the flexural strength measured here can be used in modelling of PMMA nanostructures as a maximal admissible stress. Above this value, plastic deformation and polymer failure occur.

Figure 5.17 *Results of flexural strength measurements of PMMA nanopillars.*
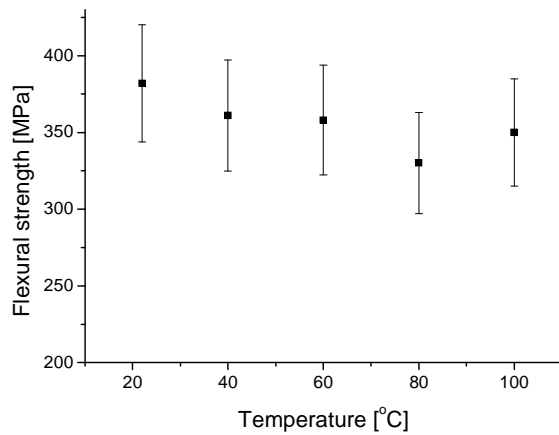
5.4.2. Viscosity

The knowledge of the Young modulus allows to evaluate the value of viscosity by using the tapping mode measurement method described in §4.3.3. An example of the phase angle measurement in tapping mode SFM is shown in **Fig 5.18**. It can clearly be seen that the phase shift and therefore, the dissipated energy is smaller for the nanopillars than for the flat polymer surface which agrees with the expectations. The results of loss modulus and viscosity measurement in different temperatures are shown in **Fig.5.19**. It is apparent that both loss modulus and the viscosity depends on the temperature. Nevertheless, the viscosity is decreasing with increasing temperatures whereas the loss modulus increases with temperature. This behavior is typical for polymers below the glass transition temperature.
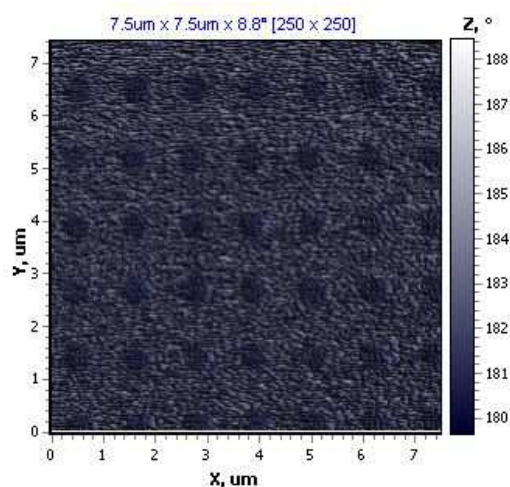

Figure 5.18 SFM tapping mode micrograph, which shows the phase shift of the cantilever's oscillation while scanning the nanopillars.
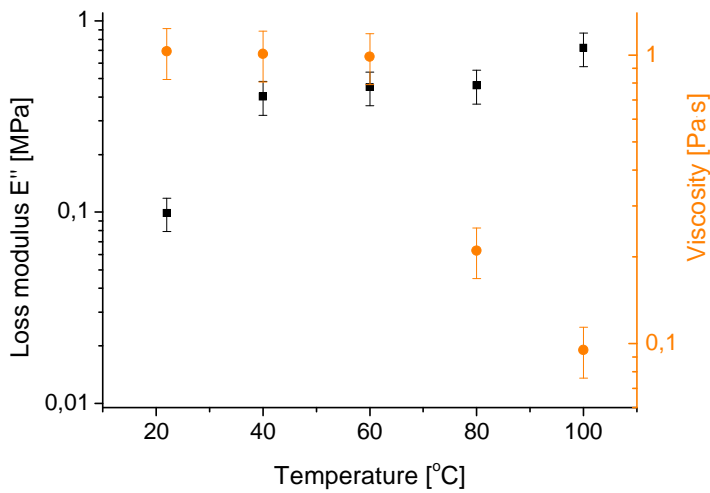
Figure 5.19 *The results of loss modulus E'' and viscosity η measurement in SFM tapping mode.*

PMMA is widely used, therefore its properties have been investigated many times in many different configurations. It should be noted that measured values of both loss modulus and viscosity of polymers strongly depend on the frequency of oscillations of the used probes or velocity of flow of the material. Molecular weight and the thickness of the polymer film are also very important in this case (more details can be found i.e. in [9]). Hence, it is quite complicated to compare the achieved results to other work. Nevertheless, the results of Young modulus and viscosity presented in this thesis agree within one order of magnitude with the results from other experiments [84-86]. To the best of the knowledge of the author, the flexural strength, has been measured for the first time on the nanoscale in this thesis. Experiments performed with bulk PMMA samples provide values for the flexural strength which are about two times smaller than measured here. There are two possible explanations. Firstly, the nanoimprint lithography process, in which the nanopillars were produced, may somehow influence their strength (temperature, high pressure). Secondly, some inaccuracies, which have not been taken into consideration and/or imperfect calibration may be the reason. However, it should be noted that the experiment gives proper values for silicon and PMMA.

6.   Summary and conclusions

6.1.   New possibilities for the investigate the mechanical properties of materials and interfaces on the nanoscale

As stated in Chapter 3, the main goal of this thesis is to develop a method to investigate the failure of materials on the nanoscale. At the end it is clear that this aim has been achieved. The Young modulus and silicon strength has been properly measured by bending and fracturing the silicon nanopillars with the SFM tip. It provides a completely new approach to the investigation of the nanomechanical properties of materials and nanostructures. A scale effect in fracture mechanics can be now studied in details using many materials. The influence of a surface energy on ultimate stresses and fracture strength can be investigated. The fast development of microfabrication techniques allows for the production of pillars even with a few nanometers in diameter, therefore, further essential knowledge towards the future design of nanomachines may be achieved.

Furthermore, due to the ability of measuring the fracture strength of interfaces, such as Si/SiO_2 interface, the technique described in this thesis may influence the progress in developing i.e. flexible electronics. In this types of devices, interfaces subjected to high stresses, play an essential role. Some successes in this field have been achieved and described in A. Kaufman thesis [40], significant progress has been achieved since and reported here, but, there remains a lot to be investigated and studied about the mechanical properties on the single nanometer scale.

6.2.   Corrosion investigation

As it mentioned in Chapter 3, the corrosion and material degradation problems consume a great amount of money. The macroscale approach to investigate these phenomena is extremely time-consuming and also can generate very high costs. One solution to this problem may be provided by experiments using much smaller amounts of material allowing for much faster experimental times to conclusion The investigations in this thesis show a new method in that a SFM is used for studying the corrosion phenomena on the nanometer scale. The fracture investigation of Si/SiO_2 nanopillars in different chemical environments proved that the here described method

provides an unique platform of such fast and relatively cheap experiments. The weakening of the measured interface in water was investigated in details. The effect was observed after a few hours. The same was achieved with strengthening of the interface in salt solutions. On the other hand, corresponding experiments on the macroscale may take weeks or even months.

The nanofracture method may find many commercial applications. For example, to measure the corrosion resistance of new alloys, nanopillars may be produced and immersed in corrosive environment. The degradation of the material and its fracture strength reduction will be then evaluated within a couple of hours. Therefore, it is expected that many commercial laboratories would like to use SFM technique instead of traditional measurement methods.

6.3.   Implication of results on nanoimprint lithography development

The mechanical and rheological properties of PMMA are immensely important for developing of nanoimprint lithography technology. As it is shown in **Fig.6.1** polymer structure may be destroyed during the demolding process due to the adhesion and friction forces.. Therefore, the results presented in this thesis may be useful in modeling the demolding process. It can be assumed that if the von Mises stress in the demolding structure goes beyond the measured flexural strength of the polymer than it will be destroyed (**Fig. 6.1a**). It is thereby possible to predict the highest manufacturable aspect ratio of structures made by PMMA in the nanoimprint lithography process.
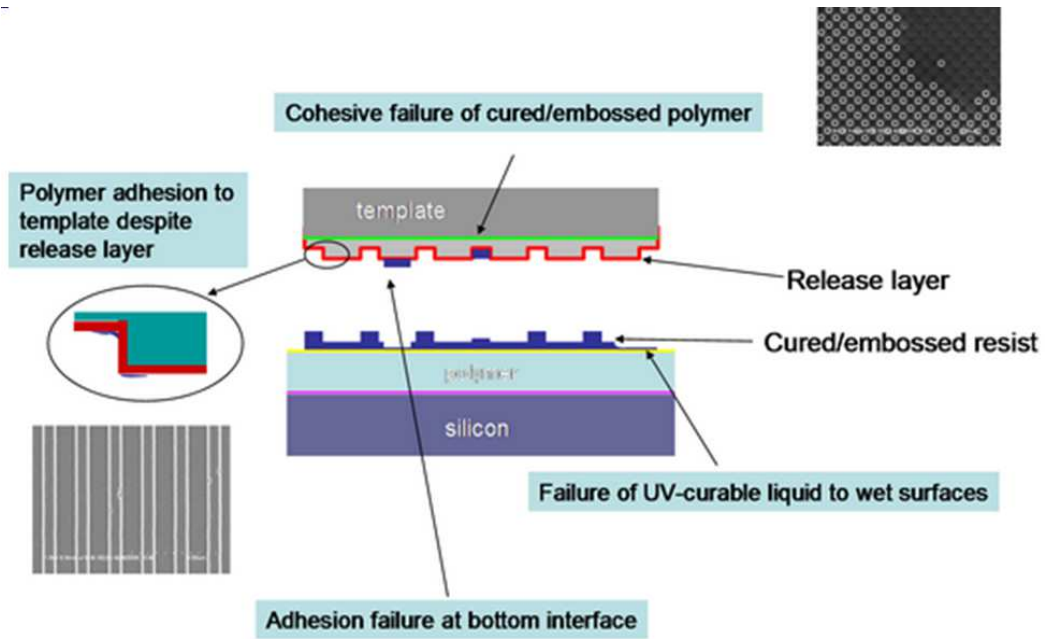
Figure 6.1 *Polymer structure may be destroyed during demolding process due to adhesion and friction forces.*

Incidentally, also during the production of PMMA nanopillars well known problems with nanoimprint lithography reoccurred and were observed: Fig.6.2 shows an SEM image of first PMMA nanopillars produced for the experiments. Actually, they are not pillars but look like beans. It was due to the fact that the polymer has not filled all the space between the template and the sample surface. The reason for this may be too high viscosity (i.e. too low temperature) and too high aspect ratio of the template nanocavities. Therefore, due to the methods of measurement described in this thesis it is possible to evaluate the relaxation modulus of the polymer at different temperatures and then model its behaviour for the nanoimprint process. It may reduce cost and time of the experiments with new-developed polymer.
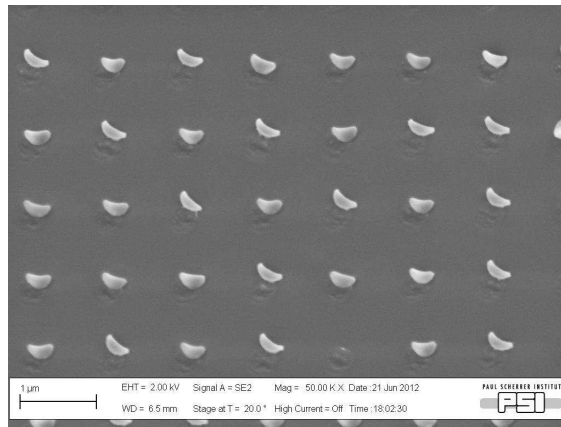
Figure 6.2 *Problems with nanoimprint lithography occurred also in PMMA nanopillars production.*

6.4. Future applications of nanofracture mechanics

The progress in nanotechnology and microfabrication is immensely fast nowadays, therefore, the need for material properties investigation in nanoscale will increase. Even now, as it was described above, there are many applications for the method evaluated in this thesis. Some more will arise soon i.e. in material science with the development of nanocomposites, in which the adhesion between ceramic nanoparticles and the matrix is of high importance.

There are still some technical problems, which should be overcome before the method will be commercialized. Many of them may be solved by developing a special software for SFM, which will ensure a higher accuracy of the measurements. Furthermore, the models developed in this thesis are usually quite simple and does not deal with all complicated processes and phenomena i.e. the indentation of the tip into a nanopillar, capillary forces etc. Also the technology of pillars production may be developed (especially if higher aspect ratios are needed) and applied to many different materials.

Nevertheless, due to the work of people who have dealt with nanopillars before, and due to this work, the investigation of material failure in nanosale, the precise method of nanofracture experiments is finally established.

A.M.D.G

Acknowledgements

Special thanks are due also to my Polish friends, without whom my stay in Switzerland would not be so good as it was: Piotr Śliwa, Iza Czekaj, Justyna Piwek and Anetta Płatek.

I would like to thank also my parents Jolanta and Leszek Jarząbek for many useful advices.

And last of all, thank you my love, Alicja Wojtowicz, for supporting me while writing, for your patience, for reading this thesis and your precious advices.

References

[1] http://researcher.watson.ibm.com

[2] T. Kobayashi, I. Yamamoto, and M. Niinomi, *Eng. Fract. Mech*. **1986**, 24(5): p. 773-782

[3] P. Moore, (ed.), in *Nondestructive Testing Handbook,* Vol. 7, American Society for Nondestructive Testing, **2007**

[4] A. N. Sinclair and T. Chan, in *Advances in Fracture Research* Vol. 5, Pergamon Press, Oxford, **1989**, p. 3145.

[5] H. D. Espinosa, R. A. Bernal, M. Minary-Jolandan, *Adv. Mater*., **2012,** 24(34): p. 4656-75

[6] G.Hodes, *Adv. Mater*. **2007**, 19(5): p. 639-655

[7] Z.P. Bazant, *Arch. Appl. Mech.* **1999**, 69(9-10): p. 703-725

[8] Y. Weia, X. Wanga, M. Zhao, *J. Mater. Res.* **2004**, 19(01): p. 1

[9] D.M. Jarzabek, Z. Rymuza, A. Horiba, Y.J. Hirai, *J. Vac. Sci. Technol. B* **2011**, 29(6)

[10] W.C. Oliver, G.M. Pharr, *J. Mater. Res*. **2004**, 19(1): p. 58-65

[11] J.B. Pethica, W.C. Oliver, in *Thin Films: Stresses and Mechanical Properties,* edited by J.C. Bravman, W.D. Nix, D.M. Barnett, and D.A. Smith, Mater. Res. Soc. Symp. Proc. 130**,** Pittsburgh, PA, **1989**, p. 13.

[12] H.F. Brinson., L.C. Brinson, *Polymer Engineering Science and Viscoelasticity*, Springer, Berlin, **2008**

[13] D. Gross, T. Seeling, *Fracture mechanics: With an Introduction to Micromechanics*, Springer, Berlin, **2011**

[14] A.A. Griffith., *The Phenomena of Rupture and Flow in Solids.* Philosophical Transactions of the Royal Society of London, London, **1920**

[15] D. Roylance, *Introduction to Fracture Mechanics*, Department of Material Science and Engineering, Massachusetts Institute of Technology, Boston, **2001**

[16] T.H. Courtney, *Mechanical Behavior of Materials*, McGraw-Hill, New York, **1990**

[17] J.E. Gordon., *The New Science of Strong Materials*, Princeton University Press, **1976**

[18] F. M. Fowkes, *Ind. Eng. Chem.* **1964** 56(12): p. 40

[19] F. M. Fowkes, M. A. Mostafa, *Ind. Eng. Chem.* 1978, 17(3)

[20] C. J. van Oss, R. J. Good, M. K. Chaudhury, *Langmuir* **1988,** 4: p.884

[21] H. Czichos, T. Saito, L.E. Smith, *Springer Handbook of Materials Measurement Methods*, Springer, Berlin, **2006**

[22] http://en.wikipedia.org/wiki/File:Tensile_specimen_nomenclature.svg

[23] http://atrona.com/charpy-testing.html

[24] ASTM E23, *Standard Test Methods for Notched Bar Impact Testing of Metallic Materials*

[25] ISO 148-1 *Metallic materials - Charpy pendulum impact test - Part 1: Test method*

[26] EN 10045-1 *Charpy impact test on metallic materials. Test method (V- and U-notches)*

[27] W.C. Oliver, G.M. Pharr GM., *J. Mater. Res.* **1992**, 7: p.1564

[28] A. Bagchi, G. Lucas, Z. Suo, A. Evans, *J. Mater. Res.* **1994**, 44: p.4051

[29] A.A. Volinsky, N.R. Moody, W.W. Gerberich, *Acta Mater* 2002, 50: p.441-466

[30] A.G. Evans, J.W. Hutchinson, *Int. J. Solids Struct.* **1984**, 20(5): p.455

[31] D.B. Marshall, A.G. Evans, *J. Appl. Phys.* **1984**, 56:2632

[32] L.G. Rosenfeld, J.E. Ritter, T.J. Lardner, M.R. Lin, *J. Appl. Phys.* **1990**, 67: p. 3291

[33] M.P. de Boer, W.W. Gerberich, *Acta Mater.* **1996**, 44: p.3169

[34] J.J. Vlassak, M.D. Drory, W.D. Nix, *J. Mater Res.* **1997**, 12: p.1900

[35] P. Benjamin, C. Weaver, *Proc. R. Soc. London* **1960**; A254: p.163

[36] P. Burnett, D. Rickersby, *Thin Solid Films* **1987,** 154: p.403

[37] H. Hirikata, T. Kitamura, Y. Yamamoto, *JSME Int. J., Ser. A* **2004**, 47(324)

[38] B. Baumeister, T.A. Jung, *Appl. Phys. Lett.* **2001**, 78(17): p. 2485-88

[39] B. Baumeister, T.A. Jung, E. Meyer, *Tribol. Lett.* **2001**, 11(2): p. 107-110

[40] A. Kaufmann, *PhD Thesis*, Basel University, Basel, **2011**

[41] A. K. Kuruvilla, *Life Prediction and Performance Assurance of Structural Materials in Corrosive Environments - A State of the Art Report* (AMPT-15), AMPTIAC, New York, **1999**

[42] G. Binnig, H. Rohrer, *Helv. Phys. Acta*, **1982**, 55(6): p. 726-735.

[43] G. Binnig, H. Rohrer, Ch. Gerber, E. Weibel, *Phys. Rev. Lett*, **1983**. 50(2): p. 120-123.

[44] Binnig, G., C.F. Quate, C. Gerber, *Phys. Rev. Lett*., **1986**. 56(9): p. 930-933.

[45] V.L. Mironov, *Fundamentals of Scanning Probe Microscopy,* The Russian Academy of Sciences, Nizhny Novgorod, **2004**

[46] C. Dupas, P. Houdy, M. Lahmani, *Nanoscience*, Springer, Berlin, **2007**

[47] M. Tortonese, M. Kirk, *Characterization of application specific probes for SPMs*, in *Micromachining and Imaging*, T.A. Michalske and M.A. Wendman, Editors, Spie - Int Soc Optical Engineering: Bellingham **1997**, p. 53-60.

[48] M. Varenberg, I. Etsion, G. Halperin,. *Rev. Sci. Inst*., **2003**. 74(7): p. 3362-3367.

[49] D.F. Ogletree, R.W. Carpick, M. Salmeron, Rev. Sci. Inst., **1996**. 67(9): p. 3298-3306.

[50] R. Garcia, and R. Perez, *Surf. Sci. Rep*. **2002,** 47, 197–301

[51] L. Wang, *Surf. Sci.* **1999** 429(178)

[52] L. Wang, *Appl. Phys. Lett.* **1998** 73(12)

[53] L. Nony, R. Boisgard, J.P. Aime, *J. Chem. Phys.* **1999,** 111(16)

[54] R. Garcia, A. San *Paulo, Phys. Rev. B* **1999,** 60(8)

[55] W. van der Water, J. Molenaar, *Nanotechnology* **2000**, 11(192)

[56] J.P. Cleveland, B. Anczykowski, A.E. Schmid, V.B. Elings, *Appl. Phys. Lett*. 1992, 72(10)

[57] J.M. Gere, S.P. Timoshenko, *Mechanics of materials*, 4th ed.; PWS Publishing Co.: Boston, **1997**.

[58] S. Timoshenko, J. M. Gere, *Mechanics of Materials*, Van Nostrand Reinhold, New York, **1972**.

[59] P. Du, I. K. Lin, H. B. Lu, and X. Zhang, J. *Micromech. Microeng.* **2010**, 20(9),

[60] G. R. Cowper, *J. Appl. Mech.***1966,** 33(2): p.335

[61] J. F. Nye, *Physical properties of crystals : their representation by tensors and matrices.* Oxford University Press, Oxford, **1985**.

[62] http://onlineheavytheory.net/silicon.html

[63] W.A. Brantley, *Jour. Appl. Phys.* **1973**, 44: p.534-535

[64] Y.S. Sohn, J.Park, G.Yoon, J.Song, S.W. Jee, J.H. Lee, S. Na, T. Kwon, K. Eom *Nanoscale Res Lett* **2010**, 5:211–216

[65] R, Hiiper, T. Gesang, W. Possart, O.-D. Hen~emann, S. Boseck, *Ultramicroscopy 1995,* 60: p.17-24

[66] S. I. Lee, S. W. Howell, A. Raman, R. Reifenberger, *Phys. Rev. B* **2002**, 66(5)

[67] H. Kahn, R. Ballarini, A.H. Heuer, *Int. J. Mat. Res*. **2010**, 101(3)

[68] T. Ando, T. Takumi, K. Sato, *Proc. IEEE. MEMS* **2009**, p.665-668

[69] M. Wiederhorn, *J. Am. Ceram. Soc*. **1967,** 50, 407

[70] B. R. Lawn, *Fracture of Brittle Solids*, Cambridge University Press, Cambridge, **1993**

[71] G. Xu, M. Y. He, D. R. Clarke, *Acta Mater.* **1999**, 47, p.4131

[72] S.W.Leea, M.T. McDowella, L.A. Berlaa, W.D. Nixa, Y. Cuia, *Proceedings of National Academy of Sciences of USA* **2012,** 109 (11)

[73] G. Xu, D.R. Clarke, *J. Appl. Phys*. **2000** 88(6)

[74] Y. Lin, T.Y. Tsui, J.J. Vlassak, *Acta Materialia* **2007***,* 55: p.2455-2464

[75] Y. Lin, JJ. Vlassak, T.Y.Tsui, A.J. McKerrow *Mater Res Soc Symp Proc* **2003**, 766:171

[76] A. Grill, D.A. Neumayer, *J Appl Phys* **2003**, 94:6697.

[77] M.W.Lane, J.M. Snodgrass, R.H. Dauskardt, **2001**, 41(9-10): p. 1615-1624.

[78] P.Y. Mabboux, K.K. Gleason, *J Electrochem Soc* **2005**;152:F7.

[79] Y. Lin , T.Y. Tsui, J.J. Vlassak, *J Electrochem Soc* **2006**:153

[80] R.H. Doremus, *J Mater Res* **1995**,10:2379.

[81] J.V. Overgaard, *Experimental results of the influence of ionic strength in liquid environment on fibre life*, in *Optical Network Engineering and Integrity*, H.H. Yuce, D.K. Paul, and R.A. Greenwell, Editors. **1996**, Spie - Int Soc Optical Engineering: Bellingham. p. 64-71.

[82] E. Kooi, M.V. Whelan*, Appl. Phys. Lett*, **1966**. 9(8): p. 314-317.

[83] A.E. Gershinskii, *Thin Solid Films*, **1980**. 70(2): p. 341-349.

[84] T.H. Distefano, J.E. Lewis, *J. Vac. Sci Tech*., **1974**. 11(6): p. 1020-1024

 [85] A.I. Fedorchenko, I. Stachiv, An-Bang Wang,   *Sens. Actuators. B*, **2009**, 142: p.111-117

[86] S. Itoh, K. Fukuzawa, Y. Hamamoto, H. Zhang, Y. Mitsuya, *Tribol Lett*. **2008**, 30: p.177-189

[87] A. A. Svintsov, O. V. Trofimov, S. I. Zaitsev, *J. Vac. Sci. Technol. B*, **2007**, 25 (6)

Appendix 1 – Details of Finite Element Simulation

Most of the FEM simulations were conducted in Abaqus 6.11-2 environment. All simulations were done in 3D mode. For every simulations 20-node hexahedral elements with reduced integration (C3D20R) were used. The mesh was design to investigate with high accuracy the current interesting problem. Therefore, for the determination of the SFM tip indentation depth into a nanopillar, denser mesh was applied around the point load (Fig. A1.1).
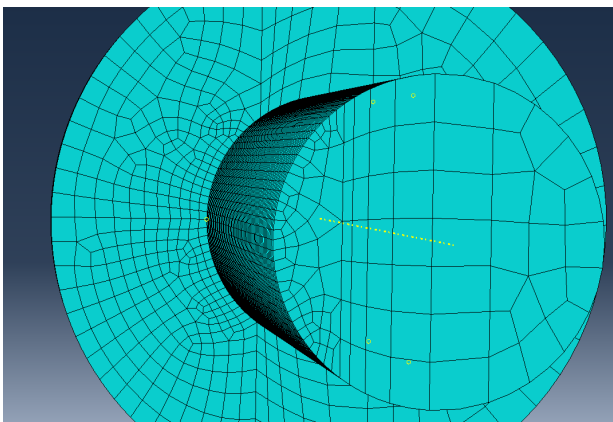

Figure A1.1 A scheme of a nanopillar used in the FEM model (view of a pillar from top). Mesh is more dense in the contact point with an SFM tip.

Material models used in the simulations:

- silicon – elastic, anisotropic (the components of the stiffness tensor are given in §4.4.1)

- silicon dioxide – elastic, isotropic (Young modulus: 72 GPa, Poisson's ratio: 0.17)

Investigated parameters: displacements and stresses.

Appendix 2 – SFM indentation test

The SFM indentation test was used in this thesis as a reference method of Young modulus determination of polymers. To get proper results, firstly, the proper contact model must be assumed. One of the simplest but still proper in this case is Hertz contact model. It works only in an elastic regime, therefore, only small forces at the beginning of the indentation should be taken into consideration. According to Hertz model, the relation between displacement δ of the indenter and the applied force F while spherical indenter is in contact with a flat surface is described by the following equation:

$$\delta = \left(\frac{9F^2}{16RE^{*2}} \right)^{1/3}$$

(Eq. A3.1)

where R is the radius of the indenter and E^* is reduced Young modulus, which is described by the relation:

$$\frac{1}{E^*} = \frac{1-v_1^2}{E_1} + \frac{1-v_2^2}{E_2}$$

(Eq. A3.2)

and E_1, E_2 are Young moduli and v_1, v_2 are Poisson's ratios associated with the indenter and the surface, respectively. The radius of the indenter was evaluated from the SEM pictures of used SFM tip. It varied from 40 to 100 nm.

During the experiment, force-distance curves from the SFM are obtained. An example of such curve is shown in Fig. A2.1. Deflection of the cantilever is measured while the sample is moved up by the piezotube. If the calibration is done properly, it is possible to determine the indentation force from the deflection of the cantilever. The indentation depth is the difference between the piezotube displacement and cantilever's deflection. After proper data evaluation, the curve, which is shown in Fig. A3.2. is obtained. The red line is a fit of eq. A2.1. From the fitting parameter, the Young modulus is then evaluated.

It is important, especially in case of soft materials, that only the beginning of force-distance curve should be investigated. Otherwise, the effects connected to plasticity may influence the value of evaluated modulus of elasticity.
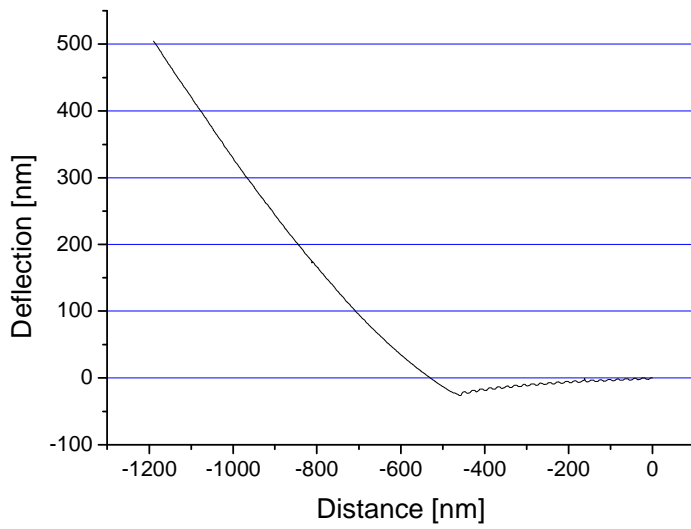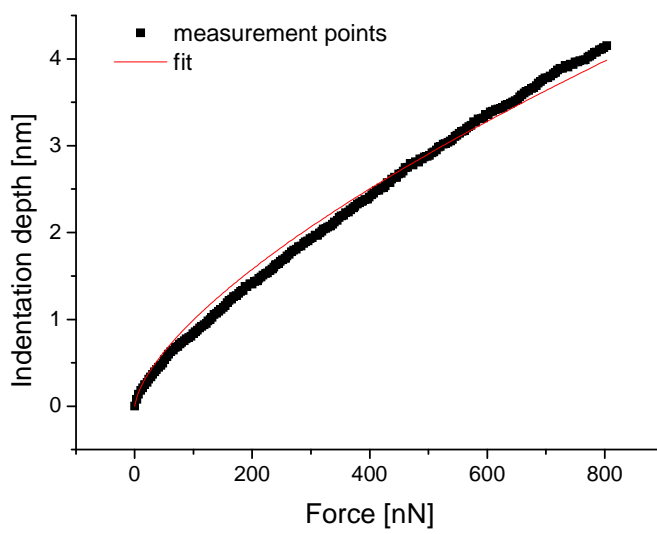
Figure A2.1 An example of SFM force-distance curve.

Figure A2.2 Young modulus determination from the fitting curve.

Appendix 3 – The theory of diffusion

Diffusion is the process by which matter is transported from one part of a system to another as a result of random molecular motion. Due to the fact that structural defect, which originate from the different characteristics of the single crystalline Si and the amorphous SiO_2, are distributed all over the Si/SiO_2 interface, different particles and ions may diffuse into it and strongly influence its properties.

The mathematical theory of diffusion in isotropic substances is based on the assumption that the rate of transfer of diffusing substance through unit area of a section is proportional to the concentration gradient measured normal to the section:

$$F = -D\frac{\partial C}{\partial x}$$

(Eq. A3.1)

where F is the rate of transfer per unit area of section, C the concentration of diffusing substance, x the space coordinate measured normal to the section, and D is called the diffusion coefficient. In the case of experiments described in this thesis, where the solutions are dilute, it is reasonable to assume that D is constant. The negative sign in eq. 6.1 arises because diffusion occurs in the direction opposite to that of increasing concentration.

The concentration C in the section changes in time. It can be calculated frome the following equation:

$$\frac{\partial C}{\partial t} = D\frac{\partial^2 C}{\partial x^2}$$

(Eq. A3.2)

where t is time. Expressions (**A3.1**) and (**A3.2**) are usually referred to as Fick's laws of diffusion, because they where firstly formulated by Fick (1855) by direct analogy with the equations of heat conduction.

Nanopillars can be modeled as small cylinders. Hence, by considering an element of volume of a cylinder of sides dr, $rd\theta$, dz, from eq. 6.1, we obtain the equation for diffusion in a cylinder,

$$\frac{\partial C}{\partial t} = \frac{1}{r}\left[\frac{\partial}{\partial r}\left(rD\frac{\partial C}{\partial r}\right) + \frac{\partial}{\partial \theta}\left(\frac{D}{r}\frac{\partial C}{\partial \theta}\right) + \frac{\partial}{\partial z}\left(rD\frac{\partial C}{\partial z}\right)\right]$$

(Eq. A3.3)

in terms of the cylindrical coordinates r, θ, z. For a circular cylinder in which diffusion is everywhere radial, equation 6.3 simplifies to:

$$\frac{\partial C}{\partial t} = \frac{1}{r}\frac{\partial}{\partial r}\left(rD\frac{\partial C}{\partial r}\right)$$

(Eq. A3.4)

According to [88], for the cylinder of radius a, on which edge the concentration is constant in time and equal to C_0 and initial concentration throughout the cylinder is 0, the solution of **Eq A3.4** is:

$$C = C_0\left(1 - \frac{2}{a}\sum_{n=1}^{\infty}\frac{\exp\left(-D\alpha_n^2 t\right)J_0(r\alpha_n)}{\alpha_n J_1(a\alpha_n)}\right)$$

(Eq. A3.5)

where $J_1(x)$ is the Bessel function of the first order and α is a root of the following equation:

$$J_0(a\alpha_n) = 0$$

(Eq. A3.6)

where $J_0(x)$ is the Bessel function of the first kind of order zero. Roots of (A3.6) are tabulated in tables of Bessel functions.

If M_t denotes the quantity of diffusing substance which has entered the cylinder in time t and M_∞ the corresponding quantity after infinite time, then from (A3.5):

$$\frac{M_t}{M_\infty} = 1 - \sum_{n=1}^{\infty}\frac{4}{a^2\alpha_n^2}\exp\left(-D\alpha_n^2 t\right)$$

(Eq. A3.7)

Author's publications

JCR journals:

1. **Jarzabek D**., Rymuza Z., Horiba A., Hirai Y., 2011, *Development of an experimental technique for testing rheological properties of ultrathin polymer films used in nanoimprint lithography*, *J. Vac. Sci. Technol. B* 29(6), IF = 1.341

2. Atasoy H., Vogler M., Haatainen T., Schleunitz A., **Jarzabek D**., Schift H., Reuther F., Gruetzner G., Rymuza Z., 2011, *Novel thermoplastic polymers with improved release properties for thermal NIL*, *Microelectronical Engineering* 88: 1902-1905, IF = 1.557

3. Kravchuk A. Rymuza Z., **Jarzabek D**., 2009, *Penetration of a pyramid indenter into a multilayer coating* , International Journal of Material Research 100: 933-935, IF = 1.667

4. **Jarzabek D**., Rymuza Z., Ohmae N., 2009, *Friction and adhesion of carbon nanotube brushes*, International Journal of Material Research 100: 973-977, IF = 1.667

5. **Jarzabek D.**, Rymuza Z., Wada T., 2008, *Mechanical and tribological behaviour of carbon nanotube brushes*, International Journal of Material Research 99: 883-887, IF = 1.667

Others:

1. Abetkovskaya S.O., Chizhik S.A., Pogoskaya I.V., Rymuza Z., **Jarząbek D**., Michałowski M., Linke J., 2012 *Determining the Young Modulus of Nanosize Thickness Coatings for MEMS from the Results of Static Force Spectroscopy*, *Bulletin of the Russian Academy of Sciences* 76(9):1009-1011

2. **Jarzabek D.**, Rymuza Z, Nowa metoda pomiaru lepkości ultracienkich warstw polimerów, Pomiary Automatyka Kontrola, 57, (2011):697-701

Books chapters:

1. Chizhik S.A., Rymuza Z., Chikunov V.V., Kuznetsova T.A., **Jarzabek D.**, *Micro- and nanoscale testing of tribomechanical properties of surfaces*, [w:] Recent Advances in Mechatronics, Jablonski R., Turkowski M., Szewczyk R.,